

University of Dayton

eCommons

Graduate Theses and Dissertations

Theses and Dissertations

2008

Restoration of defocused imagery from incoherently illuminated imaging systems with modeled point spread functions and wiener filters

Mark R. Burky
University of Dayton

Follow this and additional works at: https://ecommons.udayton.edu/graduate_theses

Recommended Citation

Burky, Mark R., "Restoration of defocused imagery from incoherently illuminated imaging systems with modeled point spread functions and wiener filters" (2008). *Graduate Theses and Dissertations*. 1846.
https://ecommons.udayton.edu/graduate_theses/1846

This Thesis is brought to you for free and open access by the Theses and Dissertations at eCommons. It has been accepted for inclusion in Graduate Theses and Dissertations by an authorized administrator of eCommons. For more information, please contact mschlangen1@udayton.edu, ecommons@udayton.edu.

**RESTORATION OF DEFOCUSED IMAGERY FROM
INCOHERENTLY ILLUMINATED IMAGING SYSTEMS WITH
MODELED POINT SPREAD FUNCTIONS AND WIENER FILTERS**

Thesis

Submitted to

The School of Engineering of the

UNIVERSITY OF DAYTON

In Partial Fulfillment of the Requirements for

The Degree

Master of Science in Electro-Optics

By

Mark R. Burky


UNIVERSITY OF DAYTON

Dayton, Ohio

August 2008

**RESTORATION OF DEFOCUSED IMAGERY FROM
INCOHERENTLY ILLUMINATED IMAGING SYSTEMS WITH
MODELED POINT SPREAD FUNCTIONS AND WIENER FILTERS**

APPROVED BY:



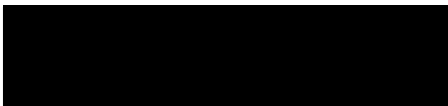
Russell Hardie, Ph. D.
Advisory Committee Chairman
Assistant Professor, Electrical Engineering
& Electro-Optics



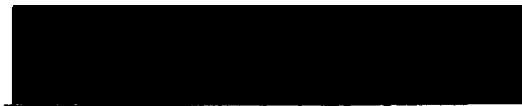
Christopher D. Brewer, Ph. D.
Committee Member
Technical Advisor
AFRL/MLPJE, WPAFB, OH



Joseph W. Haus, Ph. D.
Committee Member
Professor & Director,
Electro-Optics



Malcom W. Daniels, Ph. D.
Associate Dean
School of Engineering



Joseph E. Saliba, Ph. D., P.E.
Dean, School of Engineering

ABSTRACT

RESTORATION OF DEFOCUSED IMAGERY FROM INCOHERENTLY ILLUMINATED IMAGING SYSTEMS WITH MODELED POINT SPREAD FUNCTIONS AND WIENER FILTERS

Name: Burky, Mark R.

University of Dayton, August 2008

Advisor: Dr. Russell Hardie

The purpose of this work was to investigate defocused incoherent intensity imaging and the extent to which such defocused imagery could be restored in post-processing. A model was constructed for the defocused imaging point-spread-function given a specific imaging system that incorporates relevant information about the optical components and the sensor and uses Fresnel diffraction to propagate the modeled field. This model was applied to two imaging systems: a single-lens visible system constructed in the lab and a prefabricated multi-component MWIR imager. An analysis of each system based on how the imaging point-spread-function changes with defocus was performed and compared with actual defocused imagery. Defocused imagery for each system was restored using the modeled point-spread-functions by application of a Wiener deconvolution filter. The results were consistent with the predictions of the constructed model and suggest that under certain conditions, a reasonable facsimile of the in-focus image could be obtained upon restoring defocused imagery.

TABLE OF CONTENTS

ABSTRACT	iii
TABLE OF CONTENTS	iv
LIST OF FIGURES	vi
LIST OF TABLES	ix
CHAPTER 1 Introduction	1
CHAPTER 2 Monochromatic Defocus PSF from a Circular Lens	4
2.1 Fresnel Defocus Diffraction Integral.....	5
2.2 Computation of the Fresnel Defocus Diffraction Integral.....	6
2.3 Experimental Validation.....	17
CHAPTER 3 Imaging Defocus PSF and Image Restoration	27
3.1 Longitudinal Chromatic Aberration (LCA).....	27
3.2 Imaging Defocus Point Spread Function (PSF).....	28
3.3 Image Restoration with Wiener Deconvolution Filters.....	31
3.4 Quantitative Error Metric of Restoration.....	34
3.5 Effect of Zeros in the MTF on Image Restoration.....	35
CHAPTER 4 Application to Imaging Systems.....	38
4.1 Visible Imaging System Specification and Characterization	39
4.2 Results of Restoring Imagery from the Visible System	51
4.3 MWIR Imaging System Specification and Characterization.....	72
4.4 Results of Restoring Imagery from the MWIR System	83
CHAPTER 5 Conclusions	97
Appendix A.....	102
Appendix B.....	106
Appendix C.....	113

REFERENCES	115
------------------	-----

LIST OF FIGURES

Figure 2-1: Defocus PSF	6
Figure 2-2: Execution Speed as a Function of Defocus	13
Figure 2-3: Comparison of Execution Speeds	14
Figure 2-4: Ratio of RMS Intensities	15
Figure 2-5: 1-D Defocus PSFs – Num. Int. vs Truncated Bessel Series	16
Figure 2-6: Sample 1-D Intensity Defocus PSF (200 Samples) – Num. Int. vs. Truncated Bessel Series	17
Figure 2-7: Experimental Setup for Recording Monochromatic Intensity Defocus PSFs 18	
Figure 2-8: HeNe Defocus PSFs for $f/50$ optics – Observed vs. Predicted	19
Figure 2-9: HeNe Defocus PSFs for $f/25$ optics – Observed vs. Predicted	20
Figure 2-10: Observed vs. Predicted for $dz = -5.4$ mm, $f/50$	21
Figure 2-11: Observed vs. Predicted for $dz = 0$ mm, $f/50$	21
Figure 2-12: Observed vs. Predicted for $dz = 13.4$ mm, $f/50$	22
Figure 2-13: Observed vs. Predicted for $dz = 31$ mm, $f/50$	22
Figure 2-14: Observed vs. Predicted for $dz = -5.25$ mm, $f/25$	23
Figure 2-15: Observed vs. Predicted for $dz = -0.25$ mm, $f/25$	23
Figure 2-16: Observed vs. Predicted for $dz = 2.75$ mm, $f/25$	24
Figure 2-17: Observed vs. Predicted for $dz = 7.25$ mm, $f/25$	24
Figure 2-18: Ratio between Observed and Predicted RMS Intensities for $f/50$	26
Figure 2-19: Ratio between Observed and Predicted RMS Intensities for $f/25$	26
Figure 3-1: Sample Polychromatic Intensity PSF Computation (center wavelength of 532 nm)	29
Figure 3-2: Observation and Restoration Model in the Space Domain	31
Figure 3-3: 1-D Example of Distorted Restored Images Caused by Zeros in the Transfer Function	37
Figure 4-1: Defocused Visible Imaging System	39
Figure 4-2: Newport PAC088 Achromatic Doublet Modeled Focal Shift Curve	40

Figure 4-3: Relative Spectral Response for Sony ICX408AL CCD.....	40
Figure 4-4: Visible System Model Analysis.....	41
Figure 4-5 Horizontal Cross Sections of Modeled Imaging Defocus PSFs.....	44
Figure 4-6: Modeled Defocus MTF for Visible System with $dz = -363$ Microns.....	45
Figure 4-7: Modeled Defocus MTF for Visible System with $dz = -227$ Microns (1 st Zero in MTF).....	46
Figure 4-8: Modeled Defocus MTF for Visible System with $dz = -182$ Microns.....	47
Figure 4-9: Modeled Defocus MTF for Visible System with $dz = 0$ Microns.....	48
Figure 4-10: Modeled Defocus MTF for Visible System with $dz = 749$ Microns	49
Figure 4-11: Modeled Defocus MTF for Visible System with $dz = 2269$ Microns (1 st Zero in MTF).....	50
Figure 4-12: Bar Target, $dz = -1500$ Microns.....	53
Figure 4-13: Bar Target, $dz = -500$ Microns	54
Figure 4-14: Bar Target, $dz = -250$ Microns	55
Figure 4-15: Bar Target, Image Plane.....	56
Figure 4-16: Bar Target, $dz = 1500$ Microns.....	57
Figure 4-17: Bar Target, $dz = 2000$ Microns.....	58
Figure 4-18: Bar Target, $dz = 2500$ mm.....	59
Figure 4-19: Circuit, $dz = -1200$ Microns	61
Figure 4-20: Circuit, $dz = -450$ Microns	62
Figure 4-21: Circuit, $dz = -200$ Microns	63
Figure 4-22: Circuit, Image Plane.....	64
Figure 4-23: Circuit, $dz = 500$ Microns.....	65
Figure 4-24: Circuit, $dz = 1750$ Microns.....	66
Figure 4-25: Circuit, $dz = 2500$ Microns.....	67
Figure 4-26: Sample Full-Size Blurred Circuit Image, $dz = -450$ Microns (Zero in MTF)	68
Figure 4-27: Sample Full-Size Restored Circuit Image, $dz = -450$ Microns (Zero in MTF)	69
Figure 4-28: Sample Full-Size Defocused Circuit Image, $dz = -200$ Microns (No Zero in MTF).....	70

Figure 4-29: Sample Full-Size Restored Circuit Image, dz = -200 Microns (No Zero in MTF).....	71
Figure 4-30: MWIR Zemax Model Diagram.....	72
Figure 4-31: MWIR System Modeled Focal Shift Curve	74
Figure 4-32: Generic InSb Spectral Sensitivity	74
Figure 4-33: MWIR System Model Analysis.....	75
Figure 4-34: Horizontal Cross Sections of Modeled Imaging Defocus PSFs.....	77
Figure 4-35: Modeled Defocus MTF for MWIR System with dz = -1667 Microns (1 st Zero in MTF)	78
Figure 4-36: Modeled Defocus MTF for MWIR System with dz = -1414 Microns	79
Figure 4-37: Modeled Defocus MTF for MWIR System, Image Plane.....	80
Figure 4-38: Modeled Defocus MTF for MWIR System with dz = 859 Microns.....	81
Figure 4-39: Modeled Defocus MTF for MWIR System with dz = 1162 Microns (1 st Zero in MTF).....	82
Figure 4-40: Modeled Defocus MTF for MWIR System with dz = 1869 Microns.....	83
Figure 4-41: MWIR Imagery, dz = -2827 Microns	85
Figure 4-42: MWIR Imagery, dz = -1907 Microns	86
Figure 4-43: MWIR Imagery, dz = -1158 Microns	87
Figure 4-44: MWIR Imagery, dz = -375 Microns	88
Figure 4-45: MWIR Imagery, Image Plane.....	89
Figure 4-46: MWIR Imagery, dz = 647 Microns.....	90
Figure 4-47: MWIR Imagery, dz = 1379 Microns.....	91
Figure 4-48: MWIR Imagery, dz = 1745 Microns.....	92
Figure 4-49: Sample Full-Size Defocused MWIR Imagery, dz = -1907 Microns (Zero in MTF).....	93
Figure 4-50: Sample Full-Size Restored MWIR Imagery, dz = -1907 Microns (Zero in MTF).....	94
Figure 4-51: Sample Full-Size Defocused MWIR Imagery, dz = -375 Microns (No Zero in MTF).....	95
Figure 4-52: Sample Full-Size Restored MWIR Imagery, dz = -375 Microns (No Zero in MTF).....	96

LIST OF TABLES

Table 4-1: Important Visible System Distances	42
Table 4-2: Important MWIR System Distances	76

CHAPTER 1

Introduction

A linear, shift-invariant imaging system can be characterized by its on-axis point-spread-function or impulse response ([1] pg. 355) – the function that defines how an object point is transformed. From this perspective, defocused imaging has been well characterized in the geometric and wave (monochromatic) limits of optics ([2] and [3] for example). However, most systems image over a band of wavelengths. This complication causes the defocus PSFs associated with the geometric and wave limits of optics to be insufficient to satisfactorily restore images. For that reason, the work presented here is based upon an approximate polychromatic model for the defocused imaging PSF that builds on the defocus PSF predicted by diffraction considerations. The thesis work herein consists of the development and the application of this model to two imaging systems for the purpose of restoring actual defocused images with Wiener filters. Note that the work presented here is restricted in scope to the following limiting assumptions: that the imaging system is incoherently illuminated, that the imaging system is shift-invariant (the off-axis PSF does not deviate significantly from the axial PSF), the exit pupil is circular, and that the imaging system is monochromatically diffraction limited.

There are several possible applications of this work. The most obvious is to restore accidentally defocused imagery given that the requisite information about the imaging system is available. Another possibility is to use the computed in-focus PSF

generated from the proposed approximation to slightly enhance in-focus images taken by digital cameras in a more sophisticated way. An additional possibility is to intentionally defocus a system as an anti-aliasing measure and then restore using a Wiener filter. This last application has already been examined using an ad hoc approximation for a PSF [4]. Yet another application involves correcting chromatic aberration. Combination optical-digital imaging systems have been proposed that correct both lateral and longitudinal chromatic aberration but these require custom optical elements [5]. The methods of this thesis could be used to approximately correct longitudinal chromatic aberration in post-processing.

Chapter 2 begins by presenting the monochromatic intensity defocus PSF from a circular lens predicted by using the Fresnel diffraction integral and the assumption that a lens can be modeled as a quadratic phase transparency. As there is no closed form solution to the integral representing this PSF, a fast algorithm for computing this integral is then developed which allows tolerance enforcement. This algorithm is compared with numerical computation to justify its use. Finally, the modeled monochromatic defocus PSF was validated with experimental data. The monochromatic defocus PSF is the basis upon which the defocused imaging model is built.

In Chapter 3, the results of Chapter 2 are extended to a polychromatic approximation of a defocused imaging PSF given knowledge of a specific imaging system. The basic components of this model are the spectral sensitivity of the sensor, the pixel dimensions, the focal shift curve of the optics (variation of focus with wavelength due to longitudinal chromatic aberration), exit pupil diameter, and distance to image plane. The method by which a Wiener deconvolution filter is computed from this PSF

and used to restore blurred images is expounded upon here as well. Finally, metrics based on the computation of the defocused imaging PSF used to characterize the quality of restored defocused imagery are defined.

Chapter 4 applies the defocus model represented by Chapters 2 and 3 to two real imaging systems: a simple visible system consisting of a single lens and a board CCD constructed in the lab and a multi-component prefabricated MWIR imager with an InSb focal plane array (FPA). Modeled PSFs and MTFs for each system for incremental defocus distances of the system are presented in addition to a characterization based on the metrics defined in Chapter 3. Finally, the results of restoring defocused imagery collected from each system with a Wiener deconvolution filter is presented. Chapter 5 provides a summary of work accomplished, conclusions, and suggestions for further research.

CHAPTER 2

Monochromatic Defocus Point Spread Function from a Circular Lens

The Fresnel integral is typically a good assumption for diffraction from an aperture if the observation plane is close to the aperture. With increasing distance, z , the Fresnel integral becomes more accurate and eventually the Fresnel diffraction integral produces a Fraunhofer diffraction pattern [6] once $z \gg \frac{D^2}{\lambda}$ where D is the diameter of the aperture, λ is the wavelength of the light incident upon the aperture, and z is the distance from the aperture to the plane of observation. When a positive lens is placed at the aperture, a Fraunhofer diffraction pattern is obtained at the image plane and the Fresnel approximation is most applicable in planes near the image plane. This is precisely the area of interest in this analysis and it is therefore expected that using the Fresnel diffraction integral to compute the field displaced from the image plane by small amounts (defocus) will produce accurate results. It should be noted that although this chapter is presented assuming the optics consist of a single positive, circular lens, the results extend to a compound optical system with a positive effective focal length and a circular exit pupil by treating the system as being located at the exit pupil.

2.1 Fresnel Defocus Diffraction Integral

The Fresnel integral representing the monochromatic defocus PSF is the basic building block used to construct the defocused imaging model and is described in this section. If a lens with uniform circular aperture P of radius R is illuminated with either a plane wave or spherical wave of wave number k from an axial position, then the combined phase factor at the lens is proportional to $e^{j\frac{k}{2d_i}(x^2+y^2)}$. The Fresnel diffraction integral from such a lens for $z = d_i + \Delta z$, where z is the distance from the exit pupil to the defocus plane (z appears in Equation 2-1 only implicitly), d_i is the distance to the image plane (i.e. the focal length), and Δz is the defocus distance from the image plane (Figure 2-1), is [2]:

$$U(x,y;\Delta z) = \frac{e^{jk(d_i+\Delta z)}}{j\lambda(d_i+\Delta z)} e^{j\frac{k}{2(d_i+\Delta z)}(x^2+y^2)} \int_{-\infty}^{\infty} \int_{-\infty}^{\infty} P(u,v) e^{-\frac{jk\Delta z}{2d_i(d_i+\Delta z)}(u^2+v^2)} e^{-\frac{jk}{d_i+\Delta z}(xu+yv)} dudv \quad (2-1)$$

Letting $w = \frac{1}{8(f/\#)^2 \left(\frac{1}{\Delta z} + \frac{1}{d_i} \right)}$ and $f/\# = \frac{d_i}{2R}$, and applying the Hankel transform of

order zero ([6] pg. 11) the field is:

$$U(r,\Delta z) = 2\pi \frac{e^{jk(d_i+\Delta z)}}{j\lambda(d_i+\Delta z)} e^{j\frac{k}{2(d_i+\Delta z)}r^2} \int_0^R e^{-jkwr\frac{r'^2}{R^2}} J_0(2\pi r' \frac{r}{\lambda(d_i+\Delta z)}) r' dr' \quad (2-2)$$

In Equations 2-1 and 2-2 the variables u and v are the horizontal and vertical spatial coordinates and r' is the radial spatial coordinate in the plane of the lens. The variables x , y , and r are similarly defined in the defocus plane (See Figure 2-1). The intensity is found by taking the modulus squared of Equation 2-2 and is given by

$$I(r; \Delta z) = 4\pi^2 \frac{1}{\lambda^2 (d_i + \Delta z)^2} \left| \int_0^R e^{-jk_w \frac{r'^2}{R^2}} J_0 \left(2\pi r' \frac{r}{\lambda (d_i + \Delta z)} \right) r' dr' \right|^2 \quad (2-3)$$

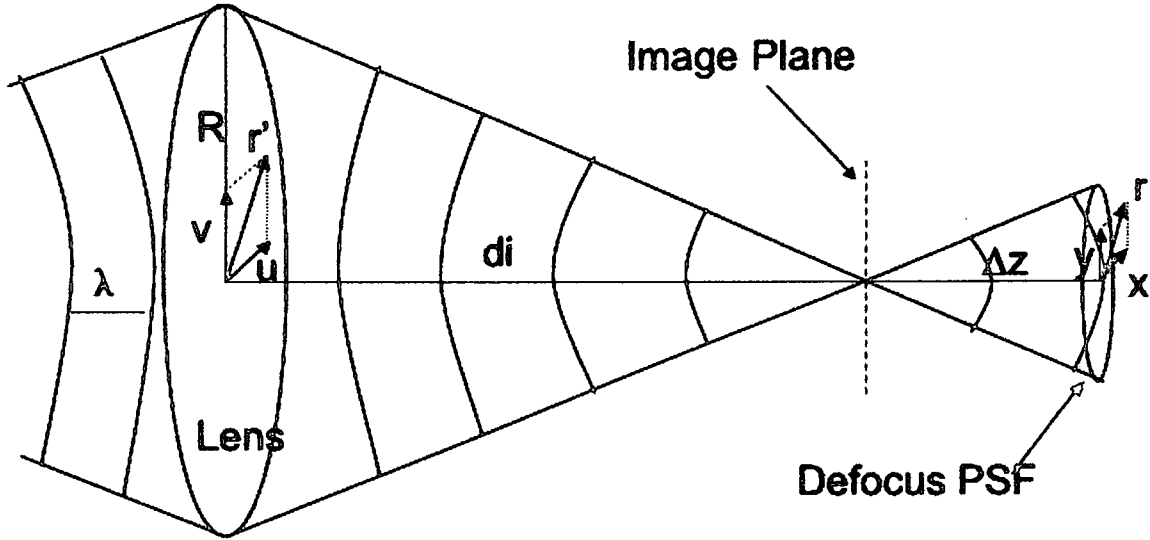


Figure 2-1: Defocus PSF

2.2 Computation of the Fresnel Defocus Diffraction Integral

It was found that the numerical computation of the integral in Equation 2-2 was both time-consuming and prone to numerical error when the number of waves of error,

$\frac{w}{\lambda}$, was large. An alternate method of computing this integral was developed and is

described here. It should be noted that the analytic evaluation of this integral in terms of series of Bessel Functions presented here is similar to the Lommel solution [7]. What is potentially new is the method by which the accuracy of the evaluation is enforced.

The integral in Equation 2-2 can be integrated by parts[8]:

$$\int_0^R e^{-jk w \frac{r'^2}{R^2}} J_0(2\pi r' \frac{r}{\lambda(d_i + \Delta z)}) r' dr' = e^{-jk w} \frac{T}{j} \sum_{n=1}^{\infty} \left(j \frac{a}{r} \right)^n J_n(br) \quad (2-4)$$

The constants T, a, and b are:

$$T = \frac{R^2}{2kw}$$

$$a = 2w \frac{d_i + \Delta z}{R}$$

$$b = \frac{kR}{d_i + \Delta z}$$

As a check, we must obtain the airy pattern if $w = 0$ (indicating $\Delta z = 0$). Since T is inversely proportional to w and a is proportional to w only the first term in the series in

Equation 2-4 has a nonzero factor. The integral is then $\frac{Rd_i}{k} \frac{J_1(\frac{kR}{d_i} r)}{r}$ and the field is given by

$$U(r, \Delta z = 0) = \frac{e^{jkd_i}}{j} e^{j \frac{k}{2d_i} r^2} \frac{J_1(\frac{kR}{d_i} r)}{r/R} \quad (2-5)$$

The squared modulus of this is the expected Airy disk - the diffraction pattern obtained in the image plane for a circular, positive lens with image plane $z = d_i$.

An alternate, equivalent series to Equation 2-4 can be found by rearranging the Bessel generating function [9]:

$$e^{\frac{x}{2}(t - \frac{1}{t})} = \sum_{n=-\infty}^{\infty} t^n J_n(x) \quad (2-6)$$

and using the property $J_{-n}(x) = (-1)^n J_n(x)$, valid for integer orders n, to obtain:

$$\sum_{n=1}^{\infty} t^n J_n(x) = e^{\frac{x}{2}(t-\frac{1}{t})} - J_0(x) - \sum_{n=1}^{\infty} (-t)^{-n} J_n(x) \quad (2-7)$$

With the substitutions $t = \frac{ja}{r}$ and $x = br$ Equation 2-7 becomes:

$$\sum_{n=1}^{\infty} \left(j \frac{a}{r}\right)^n J_n(br) = e^{j \frac{b}{2}(a + \frac{r^2}{a})} - J_0(br) - \sum_{n=1}^{\infty} \left(j \frac{r}{a}\right)^n J_n(br) \quad (2-8)$$

and so we have an alternate to Equation 2-4:

$$\int_0^R e^{-jk\omega \frac{r'^2}{R^2}} J_0(2\pi r' \frac{r}{\lambda(d_i + \Delta z)}) r' dr' = e^{-jk\omega \frac{T}{j}} \left(e^{j \frac{b}{2}(a + \frac{r^2}{a})} - J_0(br) - \sum_{n=1}^{\infty} \left(j \frac{r}{a}\right)^n J_n(br) \right) \quad (2-9)$$

Equation 2-4 is a series in increasing powers of $\frac{a}{r}$ and should converge quickly

for $r > a$, while Equation 2-9 is a series in increasing powers of $\frac{r}{a}$ and should converge

quickly for $r < a$. The strategy is to truncate, in a regulated way, each series and use each only in its domain of fast convergence.

We now derive upper bounds on the magnitude of the absolute errors obtained from truncating the two series. We define the following functions:

$$\begin{aligned} S(r, M) &= e^{j \frac{b}{2}(a + \frac{r^2}{a})} - J_0(br) - \sum_{n=1}^M \left(j \frac{r}{a}\right)^n J_n(br) \\ L(r, M) &= \sum_{n=1}^M \left(j \frac{a}{r}\right)^n J_n(br) \end{aligned} \quad (2-10)$$

The magnitude of the errors in truncating each series at $n=M$ for M an integer ≥ 1 are:

$$\begin{aligned}
E_s(r, M) &= |S(r, \infty) - S(r, M)| = \left| \sum_{n=M+1}^{\infty} \left(j \frac{r}{a} \right)^n J_n(br) \right| \\
E_l(r, M) &= |L(r, \infty) - L(r, M)| = \left| \sum_{n=M+1}^{\infty} \left(j \frac{a}{r} \right)^n J_n(br) \right|
\end{aligned} \tag{2-11}$$

The letters "S" and "L" correspond to "short" ($r < |a|$) and "long" ($r > |a|$) in relation to the domain over which we intend to use each series. The following uniform bound for the magnitude of a Bessel function [10] is used to derive the bounds:

$$|J_n(x)| < \frac{0.6748}{n^{1/3}} \tag{2-12}$$

The magnitude error E_s is then

$$\begin{aligned}
E_s(r, M) &= \left| \sum_{n=M+1}^{\infty} \left(j \frac{r}{a} \right)^n J_n(br) \right| \leq \sum_{n=M+1}^{\infty} \left| \left(j \frac{r}{a} \right)^n \right| |J_n(br)| < \sum_{n=M+1}^{\infty} \left(\frac{r}{|a|} \right)^n \frac{0.6748}{n^{1/3}} \leq \\
&\frac{0.6748}{(M+1)^{1/3}} \sum_{n=M+1}^{\infty} \left(\frac{r}{|a|} \right)^n = \frac{0.6748}{(M+1)^{1/3}} \left(\frac{r}{|a|} \right)^{M+1} \sum_{n=0}^{\infty} \left(\frac{r}{|a|} \right)^n = \frac{0.6748}{(M+1)^{1/3}} \left(\frac{r}{|a|} \right)^{M+1} \frac{1}{1 - \frac{r}{|a|}}
\end{aligned} \tag{2-13}$$

We have used the facts that $M+1 \leq n \Rightarrow \frac{1}{(n)^{1/3}} \leq \frac{1}{(M+1)^{1/3}}$ and $\sum_{n=0}^{\infty} x^n = \frac{1}{1-x}$ so long

as $|x| < 1$. The above bound on E_s is therefore valid so long as $r < |a|$. The same method produces a similar result for E_l . In summary, the bounds on the magnitude errors are

$$\begin{aligned}
E_s(r, M) &\leq \frac{0.6748}{(M+1)^{1/3}} \left(\frac{r}{|a|} \right)^{M+1} \frac{1}{1 - \frac{r}{|a|}} \quad ; r < |a| \\
E_l(r, M) &\leq \frac{0.6748}{(M+1)^{1/3}} \left(\frac{|a|}{r} \right)^{M+1} \frac{1}{1 - \frac{|a|}{r}} \quad ; r > |a|
\end{aligned} \tag{2-14}$$

Note that $r_2 > r_1 \Rightarrow E_s(r_2, M) > E_s(r_1, M)$ and $r_4 < r_3 \Rightarrow E_t(r_4, M) > E_t(r_3, M)$. Hence, if we compute, $E_s(r = (1 - \varepsilon)a, M)$ and $E_t(r = (1 + \varepsilon)a, M)$ for some positive number $\varepsilon < 1$, we are guaranteed that the absolute errors for $r < (1 - \varepsilon)|a|$ and $r > (1 + \varepsilon)|a|$ will have even smaller upper bounds. Furthermore, $E_s(r = 0, M) = 0$ and $E_t(r \rightarrow \infty, M) = 0$ meaning that the approximations are exact for those values of r . It should also be noted that E_s and E_t diverge as $r \rightarrow |a|$. This means only that the derived bounds diverge, not that the series diverge. In fact, both series in question converge absolutely for all values of r [8].

The above analysis allows for tolerance enforcement upon the truncated series in Equation 2-10 except for at $r = |a|$. Luckily, $r = |a|$ appears to be the only finite value of r (other than $r = 0$ and $r = \infty$) for which the infinite series $S(r, \infty)$ and $L(r, \infty)$ can be summed in closed form. Rearranging Equation 2-8 and setting $r = |a|$ we have:

$$\sum_1^{\infty} (\text{sign}(a)j)^n J_n(b|a|) = \frac{1}{2} [e^{jba} - J_0(b|a|)] \quad (2-15)$$

Hence, since the infinite series evaluated at $r = |a|$ is

$$A = S(r = |a|, \infty) = L(r = |a|, \infty) = \frac{1}{2} [e^{jba} - J_0(b|a|)] \quad (2-16)$$

Where we have introduced the constant A for convenience. Having the exact value of these sums at $r = |a|$ allows us to compute the error for $S(r, M)$ and $L(r, M)$ at the one value of r for which the derived bounds in Equation 2-14 are invalid.

We introduce the following algorithm, using the results derived above, to compute the Fresnel diffraction pattern from a circular lens of radius R illuminated by either a spherical wave or plane wave with axial positioning in an observation plane defocused Δz from the image plane.

Define the function $B(r, M)$ by the following approximation to the full series

$$S(r, \infty) = L(r, \infty).$$

$$B(r, M) = \begin{cases} S(r, M) & ; r < |a| \\ L(r, M) & ; r \geq |a| \end{cases} \quad (2-17)$$

The function $E(r, M)$ in Equation 2-18 is defined as an upper bound on the magnitude of the fractional error in B from the infinite series at each value of r .

$$E(r, M) = \begin{cases} \frac{E_s(r, M)}{|S(r, M)|} & ; r < |a| \\ \frac{|L(|a|, M) - A|}{|L(|a|, M)|} & ; r = |a| \\ \frac{E_l(r, M)}{|L(r, M)|} & ; r > |a| \end{cases} \quad (2-18)$$

Now, although we have bounds on the fractional errors for all values of r , the upper bounds in Equations 2-14 diverge as r approaches $|a|$. We therefore consider E only for a domain $D_\epsilon = \{r : r < (1 - \epsilon)|a|\} \cup \{|a|\} \cup \{r : r > (1 + \epsilon)|a|\}$ for some positive number $\epsilon < 1$. This leaves the possibility of errors larger than desired in the domain about $r = |a|$ excluded from D_ϵ . However, so long as $\epsilon \ll 1$ errors above that which is specified should be minimal because $|a| \in D_\epsilon$ and both the intensity distribution and Bessel functions are continuous functions of r .

The algorithm is as follows:

- 1) If $w = 0$, skip steps 2-4.
- 2) Select a tolerance, τ , a positive number, $\epsilon < 1$, and set $m = 1$.
- 3) Compute $B(r, m)$ and $E(D_\epsilon, m)$

- 4) If $\text{Max}(E(D_\epsilon, m)) > \tau$ then set $m = m + 1$ and repeat steps 3 and 4.
- 5) If $w = 0$ the field is given by Equation 2-5 and the intensity is the squared modulus given by

$$I(r, \Delta z = 0) = |U(r, d_i, \Delta z = 0)|^2 = \left(\frac{J_1\left(\frac{kR}{d_i} r\right)}{r/R} \right)^2 \quad (2-19)$$

If $w \neq 0$ set M equal to the last value of m determined in steps 2-4. Combining Equations 2-2 and 2-4 the field is approximately

$$U(r, \Delta z) \cong -e^{jk(d_i + \Delta z)} e^{j\frac{k}{2(d_i + \Delta z)} r^2} e^{-jk w} \frac{R^2}{2w(d_i + \Delta z)} B(r, M) \quad (2-20)$$

The intensity pattern is then

$$I(r, \Delta z) = |U(r, \Delta z)|^2 \cong \left(\frac{R^2}{2w(d_i + \Delta z)} \right)^2 |B(r, M)|^2 \quad (2-21)$$

The intensity pattern output by this algorithm (See Appendix A) was compared with the resultant intensity pattern found by numerically evaluating the integral in Equation 2-2 with adaptive Lobatto quadrature [11] using MATLAB. The assumed parameters are $\lambda = 1 \mu m$, $R = 25 mm$, $d_i = 250 mm$, $\tau = 0.001$, and $\epsilon = 0.01$. The one-dimensional intensities were computed for defocus distances $\Delta z = -10 \dots 10 mm$ (corresponding to the number of waves of error ranging from $w/\lambda \approx -50 \dots 50$) for 20 evenly spaced radial points (except possibly for the points adjacent to $r = |a|$) from $r = 0 \dots \max(2a, 5r_0)$ where $r_0 = 1.220\lambda f/\#$ is the first zero of the Airy disk.

Figures 2-2 and 2-3 show speed comparisons between the two methods. The gain in execution speed in Figure 2-3 is close to 1.6 orders of magnitude over a wide range of defocus errors. In later chapters, some plots were made with the computation of 10,000 defocus PSFs. The total execution time if each computation required 25 seconds (the average execution time for the numerical method between -25 and + 25 waves of error) would be about 3 days. If each required only 0.48 seconds (the average execution time for the developed algorithm between -25 and + 25 waves of error) the execution time would be 1.3 hours.

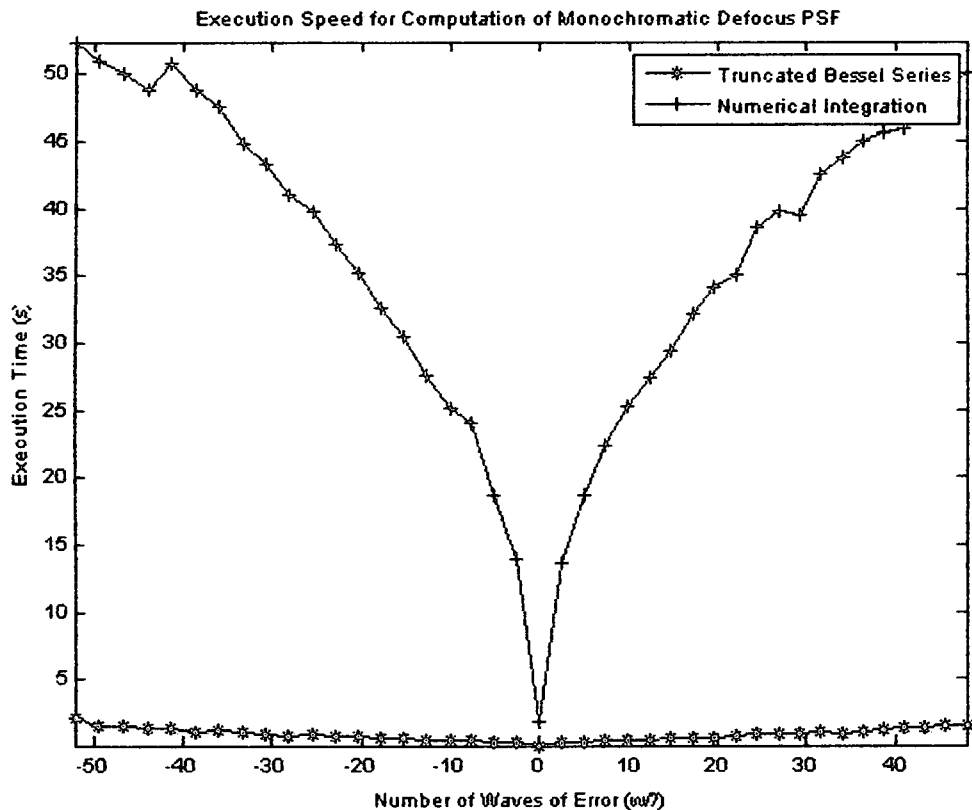


Figure 2-2: Execution Speed as a Function of Defocus

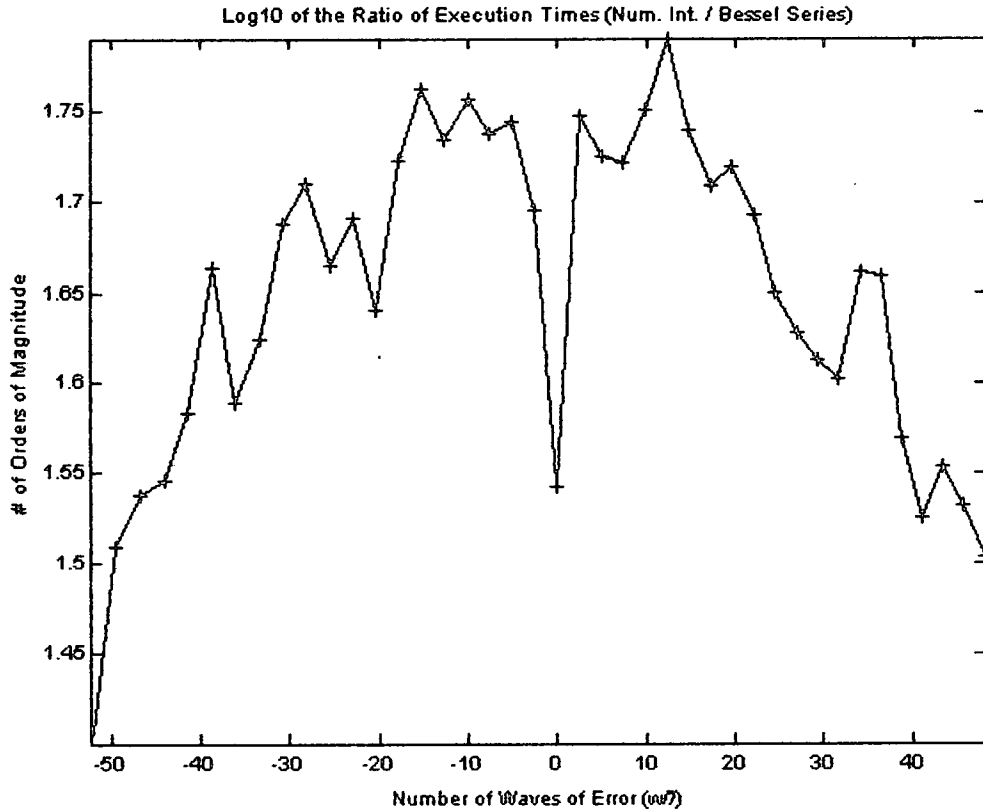


Figure 2-3: Comparison of Execution Speeds

Figure 2-4 shows the ratio of the RMS intensities at each defocus position. The average RMS value was 1.0000 and the standard deviation was $4.95\text{E-}5$ for values between -25 and + 25 waves of error. This indicates excellent agreement for smaller amounts of defocus. However, as seen in Figure 2-4, the two methods predict diverging RMS intensities as defocus increases. The reason for this increasing discrepancy is increasing errors produced by numerical integration. For large amounts of defocus error, MATLAB output warnings suggesting the numerical integration was failing.

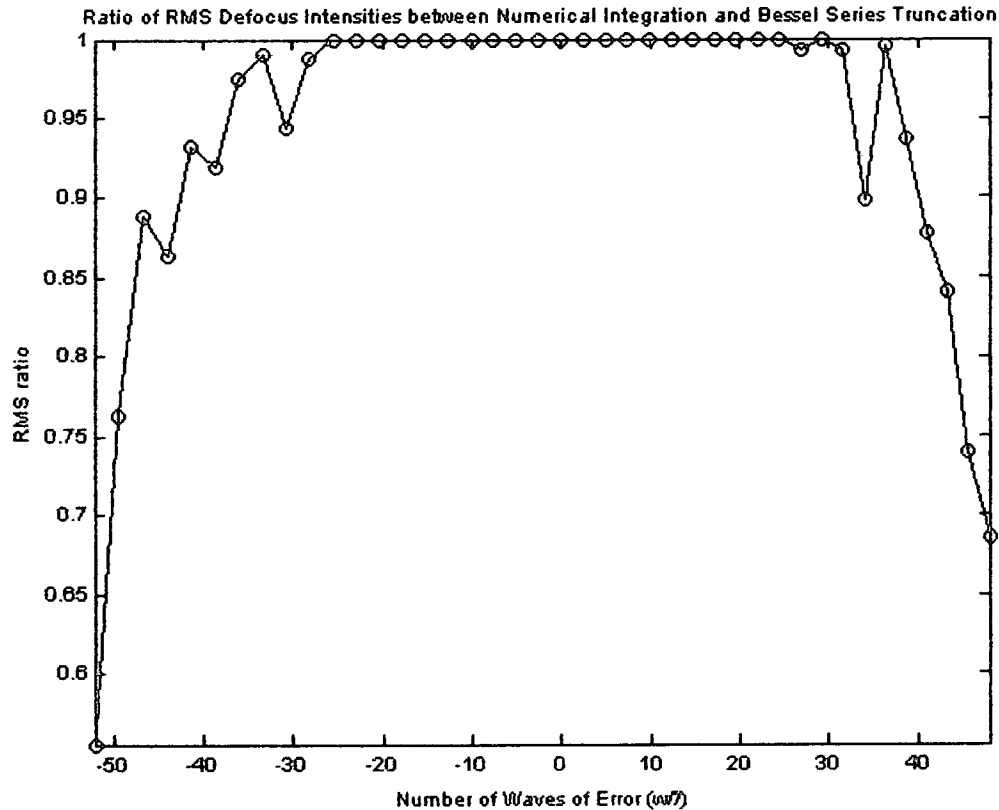


Figure 2-4: Ratio of RMS Intensities

Figure 2-5 plots the intensity patterns used in the execution speed plots above for several defocus positions for each method. For large amounts of defocus error (# of waves of defocus error larger than 25) the intensity pattern produced by numerical integration contains large errors. For example, consider the plot in Figure 2-5 with $w/\lambda \approx 52$ and $dz = -10$ mm (top left plot). For such a large defocus error, the intensity pattern should be similar to that predicted by geometric optics. Geometric optics with these parameters predicts a pillbox shaped PSF with a radius dictated by using similar triangles: $\frac{d_i}{R} = \frac{dz}{r} \Rightarrow r = \frac{Rdz}{d_i} = \frac{25 \cdot 10}{250} = 1$ mm where R is the radius of the lens, d_i is the distance to the image plane, dz is the defocus distance, and r is the radius of the geometric defocus PSF. This is consistent with the intensity pattern produced by the

derived algorithm that shows a cutoff radius of about 1000 microns and the pattern produced by numerical integration must be erroneous.

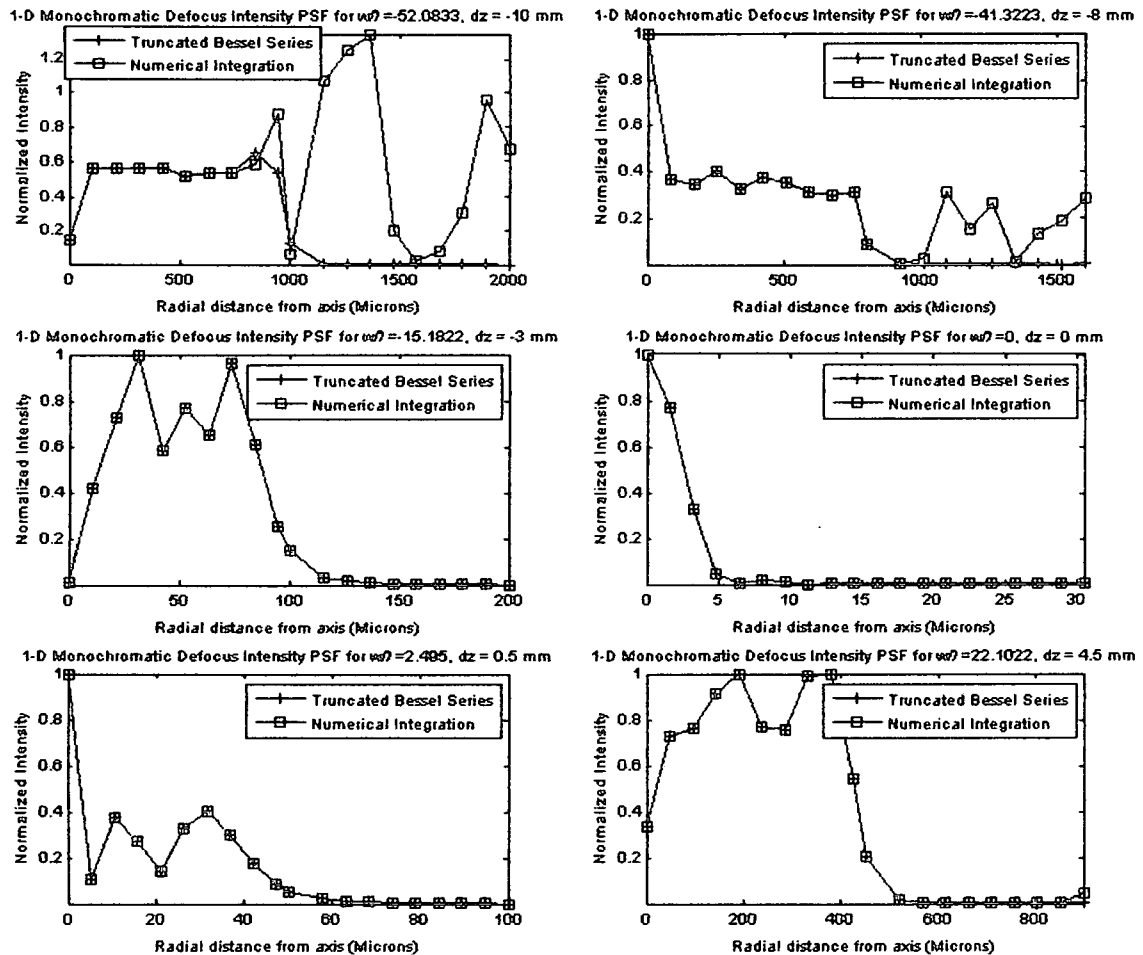


Figure 2-5: 1-D Defocus PSFs – Num. Int. vs Truncated Bessel Series

Figure 2-6 shows the intensity pattern for one selected defocus position with 200 radial points computed. The intensity distributions in Figure 6 required 252 seconds and 8.3 seconds for numerical integration and Bessel series truncation respectively.

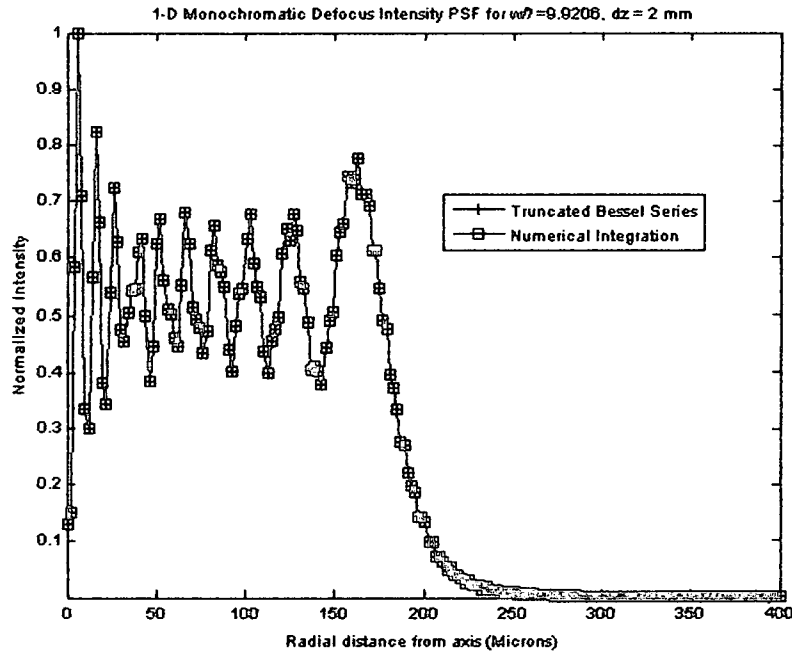


Figure 2-6: Sample 1-D Intensity Defocus PSF (200 Samples) – Num. Int. vs. Truncated Bessel Series

2.3 Experimental Validation

An experiment was designed to validate the defocus model presented in the preceding sections against defocus data. A HeNe laser was focused with a microscope objective, spatially filtered with a pinhole, and imaged with a circular, achromatic doublet onto a CCD board camera (See Figure 2-7). The position of the CCD relative to the image plane was translated with a micrometer and the intensity patterns recorded. The data collection was performed with all external lights off so that only the HeNe point source was imaged. The recorded intensity patterns were compared with the associated predicted intensity patterns from Section 2.2. In addition the intensities were rotated about their axis to provide 2D PSFs, averaged over the pixel dimensions of the CCD, and sampled at the same pixel frequency as the CCD (See Appendix B for MATLAB files).

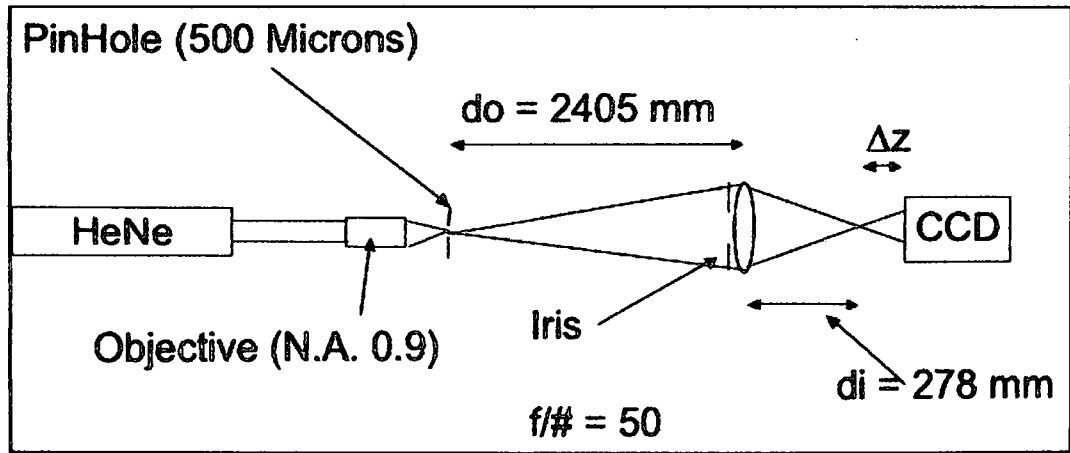


Figure 2-7: Experimental Setup for Recording Monochromatic Intensity Defocus PSFs

The CCD used, a Sony ICX408AL, had pixel dimensions of $6.4 \times 7.5 \mu\text{m}$ and a minimum sampling frequency of $f_s = \frac{1}{7.5}(\mu\text{m})^{-1}$. The smaller of the two maximum spatial frequencies detectable (Nyquist frequencies) in the horizontal and vertical directions is then [12]:

$$f_N = \frac{1}{2} f_s = \frac{1}{2 \cdot 7.5} = 0.067(\mu\text{m})^{-1} \quad (2-22)$$

By equating this with the optical cutoff frequency (incoherent) a suitable $f/\#$ ($f/\# = \frac{d_i}{D}$) where d_i is the distance to the image and D is the diameter of the exit pupil) could be selected to insure the recorded defocus patterns were not aliased (in either the vertical or horizontal directions):

$$f_c = \frac{1}{\lambda f/\#} \leq f_N \Rightarrow f/\# \geq \frac{1}{\lambda f_N} = \frac{1}{0.6328[\mu\text{m}] * 0.067[\mu\text{m}]^{-1}} \approx 23.6 \quad (2-23)$$

Data was collected for $f/\#$ s 25 and 50.

Figures 2-8 and 2-9 show the observed and predicted 2D intensity defocus PSFs for select defocus positions.

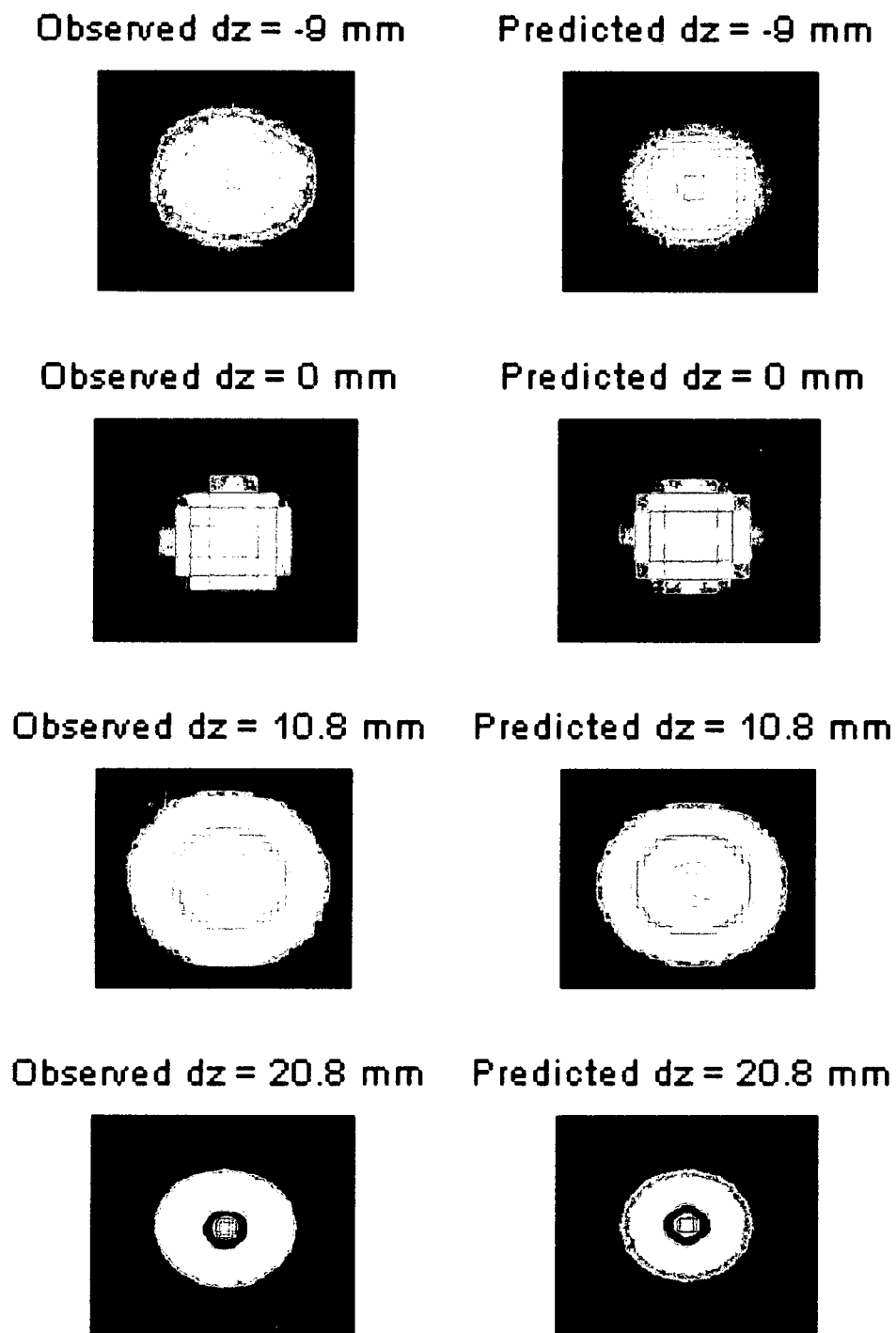
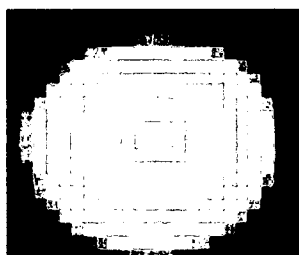
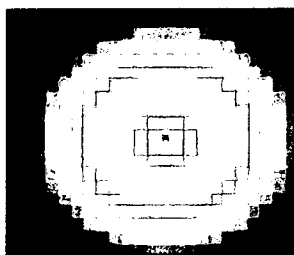


Figure 2-8: HeNe Defocus PSFs for $f/50$ optics – Observed vs. Predicted

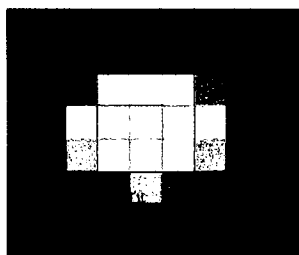
Observed $dz = -3.75$ mm



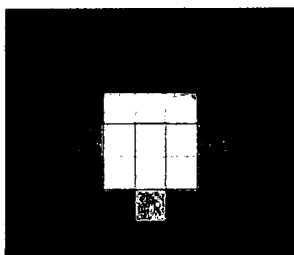
Predicted $dz = -3.75$ mm



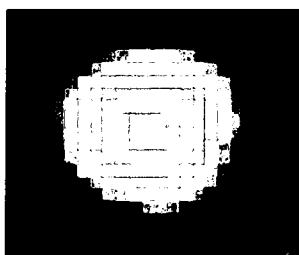
Observed $dz = -0.25$ mm



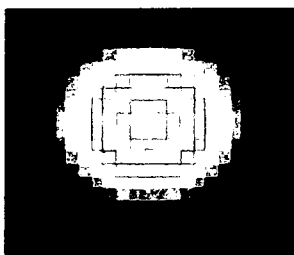
Predicted $dz = -0.25$ mm



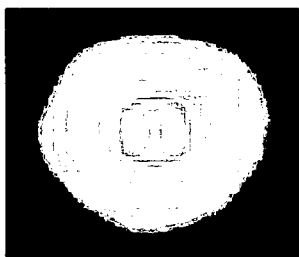
Observed $dz = 2.75$ mm



Predicted $dz = 2.75$ mm



Observed $dz = 7.75$ mm



Predicted $dz = 7.75$ mm

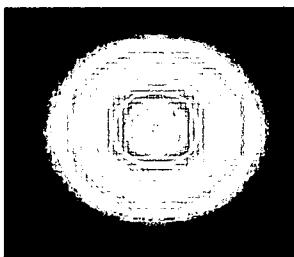


Figure 2-9: HeNe Defocus PSFs for f/25 optics – Observed vs. Predicted

Figures 2-10 through 2-17 show the observed and predicted intensities for horizontal cross sections for select defocus positions.

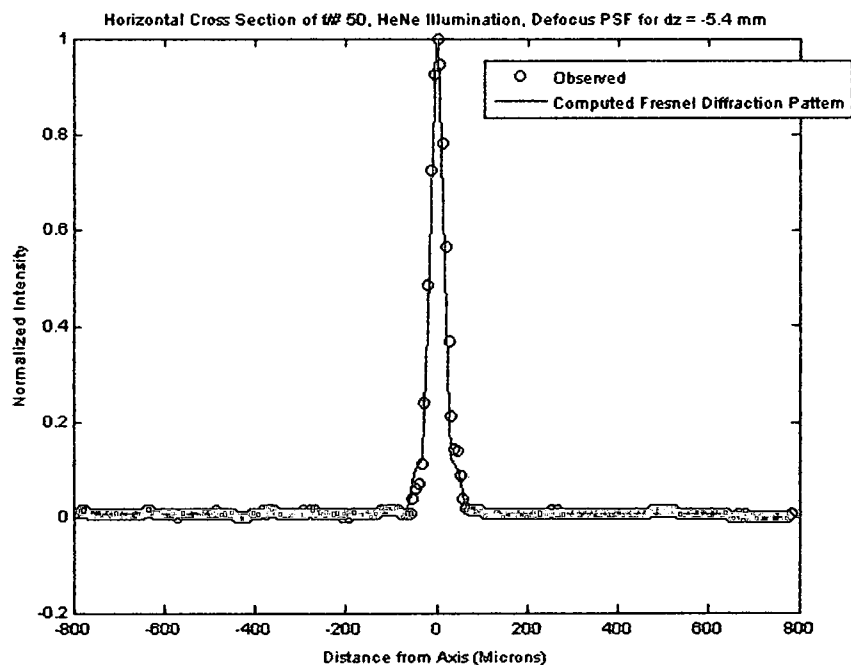


Figure 2-10: Observed vs. Predicted for $dz = -5.4$ mm, $f/50$

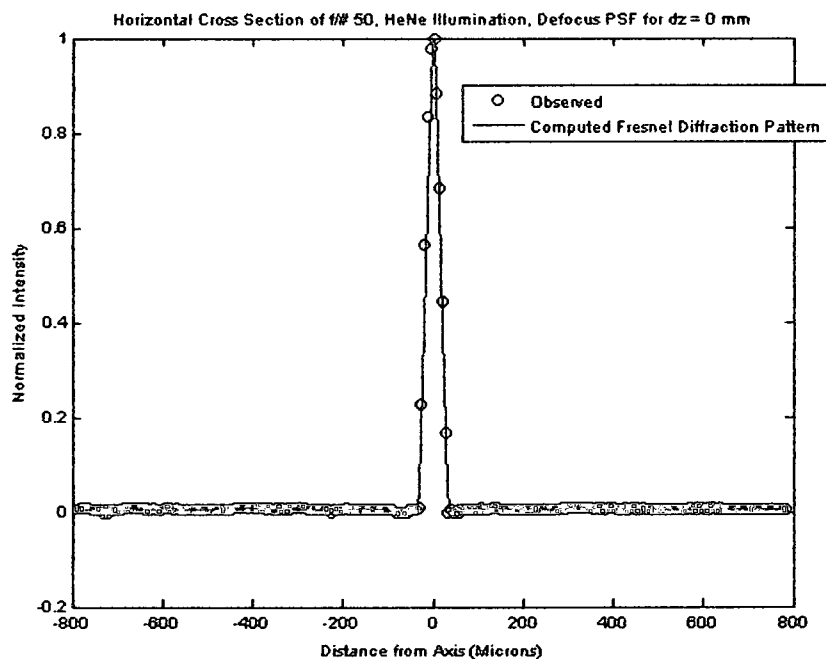


Figure 2-11: Observed vs. Predicted for $dz = 0$ mm, $f/50$

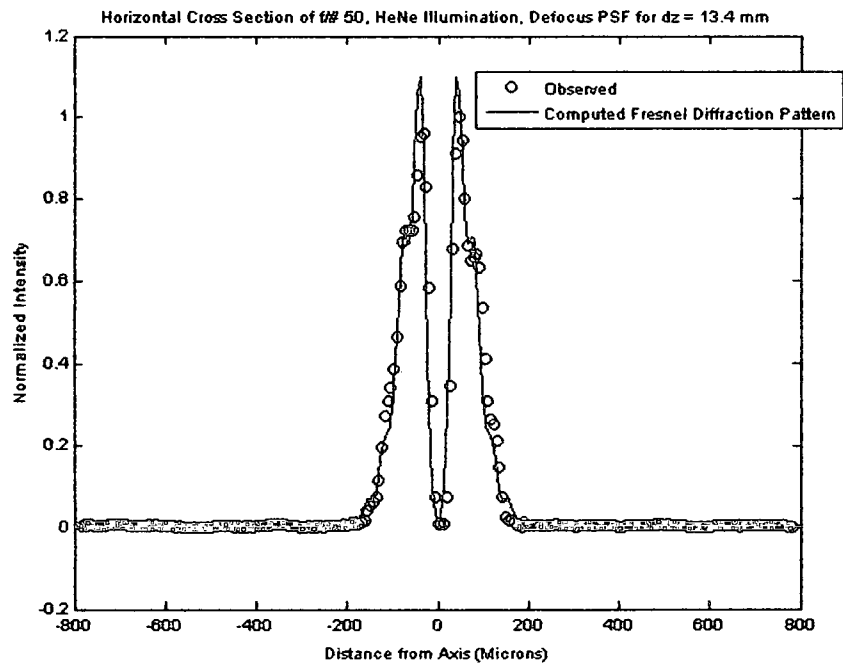


Figure 2-12: Observed vs. Predicted for $dz = 13.4$ mm, $f/50$

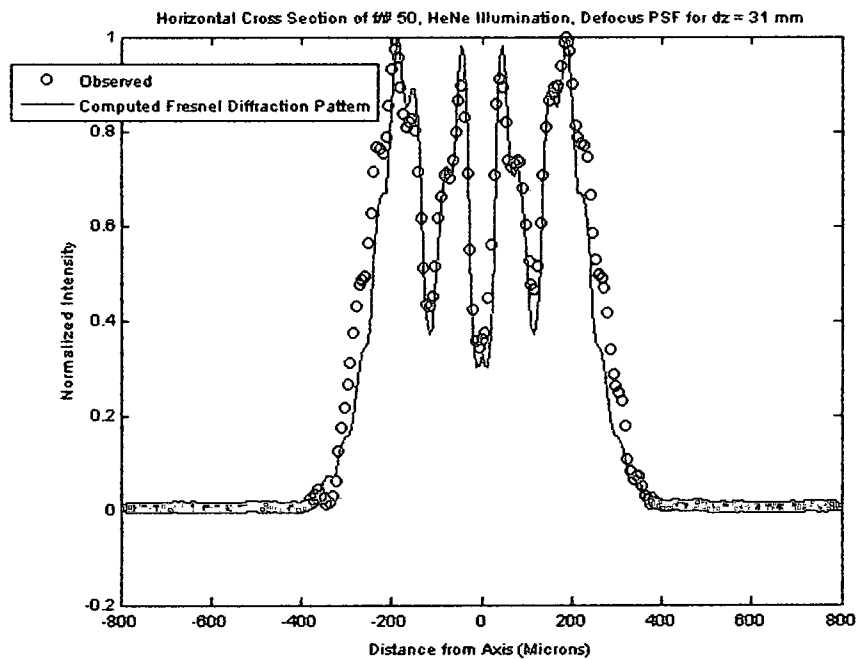


Figure 2-13: Observed vs. Predicted for $dz = 31$ mm, $f/50$

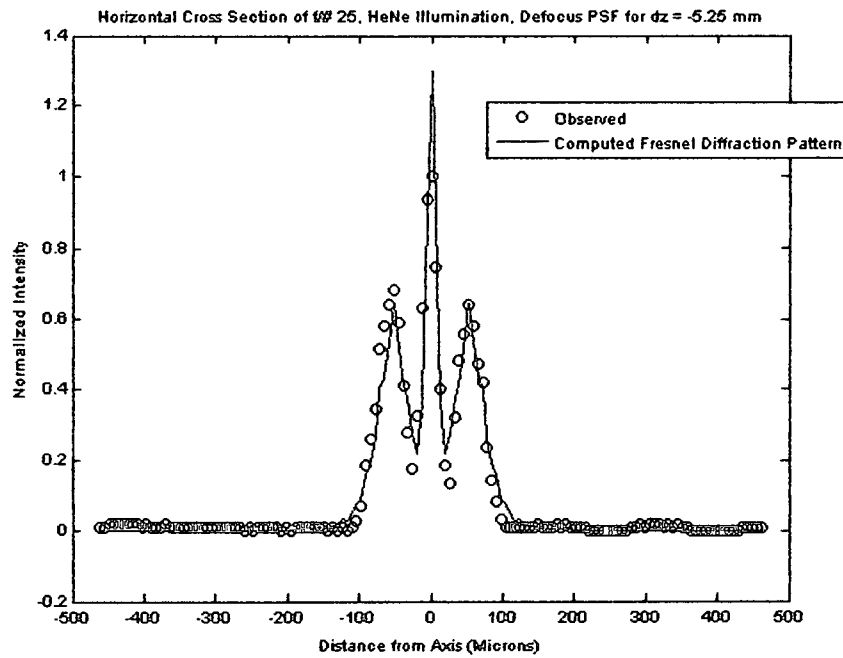


Figure 2-14: Observed vs. Predicted for $dz = -5.25$ mm, $f/25$

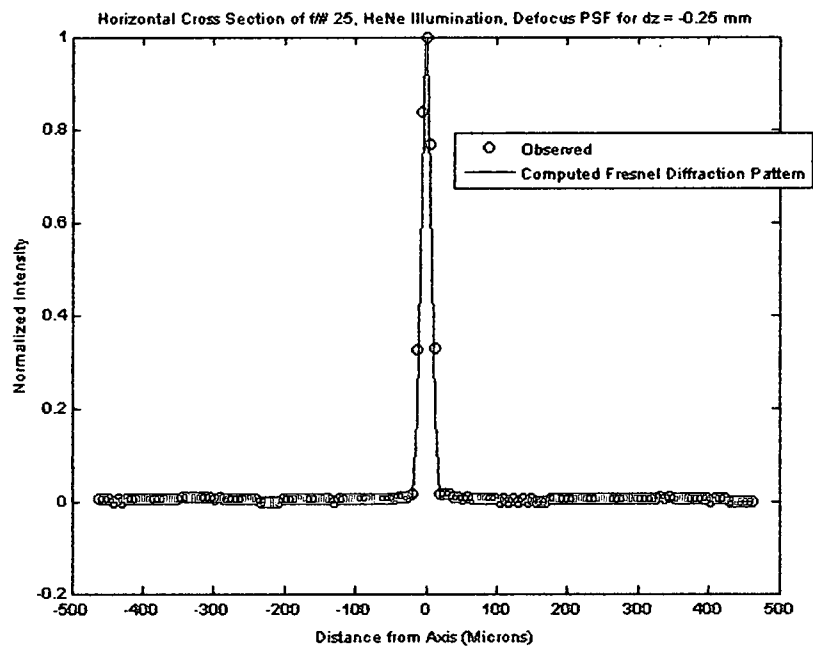


Figure 2-15: Observed vs. Predicted for $dz = -0.25$ mm, $f/25$

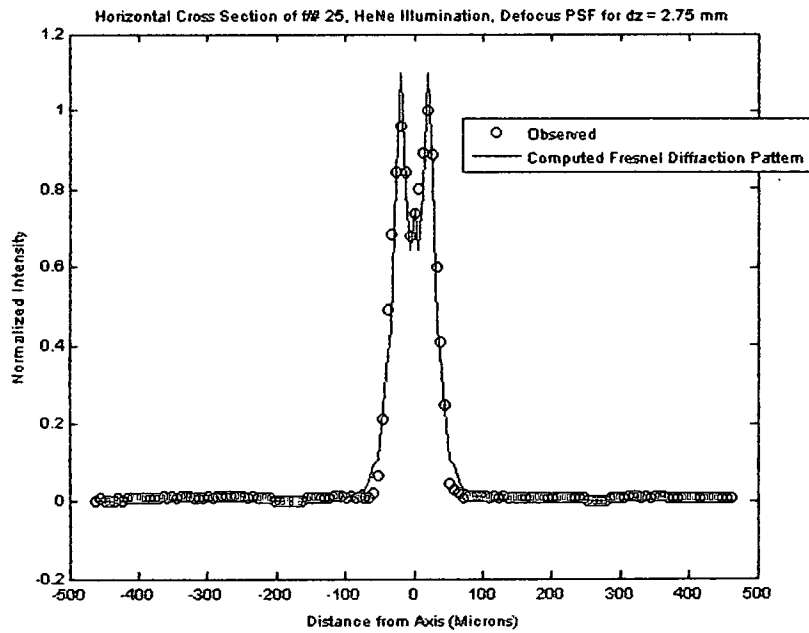


Figure 2-16: Observed vs. Predicted for $dz = 2.75$ mm, $f/25$

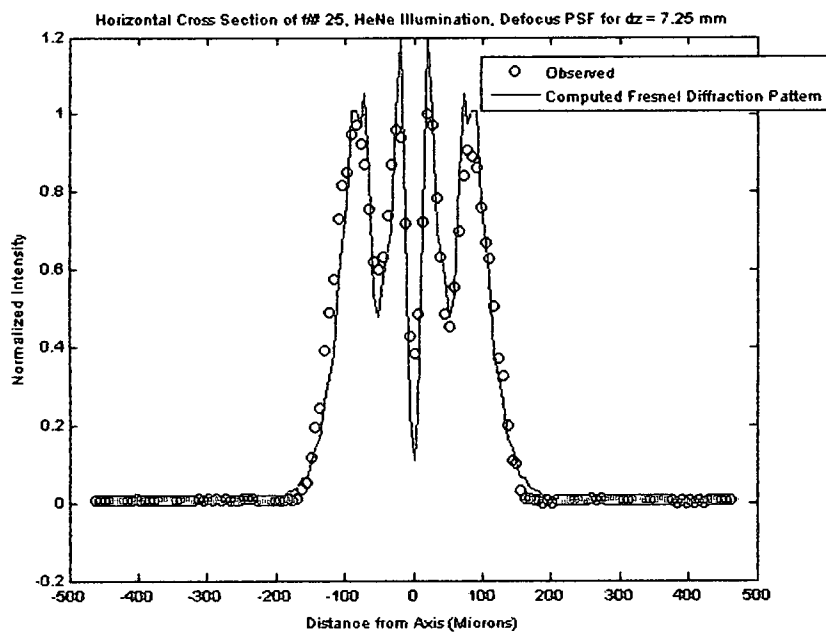


Figure 2-17: Observed vs. Predicted for $dz = 7.25$ mm, $f/25$

Assuming the total energy is a constant with defocus position, we can quantitatively compare the observed and predicted intensities by normalizing each intensity pattern by its integral. After this normalization was performed, the root-mean-square (RMS) intensity was calculated for each observed and predicted defocus PSF. The ratios of their RMS intensities are in Figures 2-18 and 2-19. For the $f/50$ configuration the average value of the ratio of RMS intensities of the Fresnel prediction to the observed value was 0.97 with a standard deviation of 0.03. For the $f/25$ configuration the average ratio was 0.97 with a standard deviation of 0.035.

One source of error that could explain the discrepancy in the RMS intensities is that a 500-micron pinhole was used for the source. This would cause the measured PSF to be slightly more spread out than a true point source and would cause the RMS intensity of the measured PSF to be slightly smaller than that predicted assuming a true point source. The result would cause the ratio of the RMS intensities to be less than one. This assessment is consistent with the results.

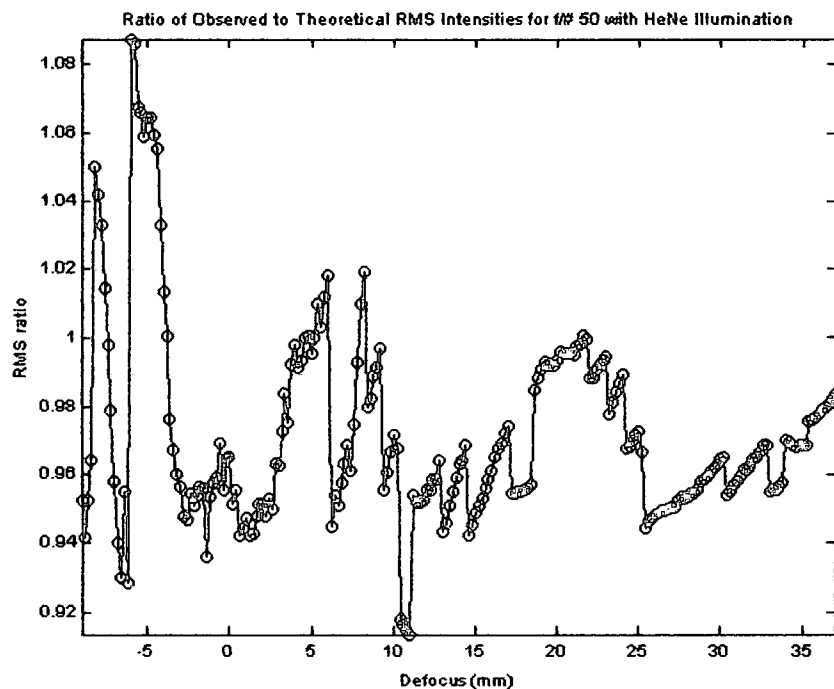


Figure 2-18: Ratio between Observed and Predicted RMS Intensities for $f/50$

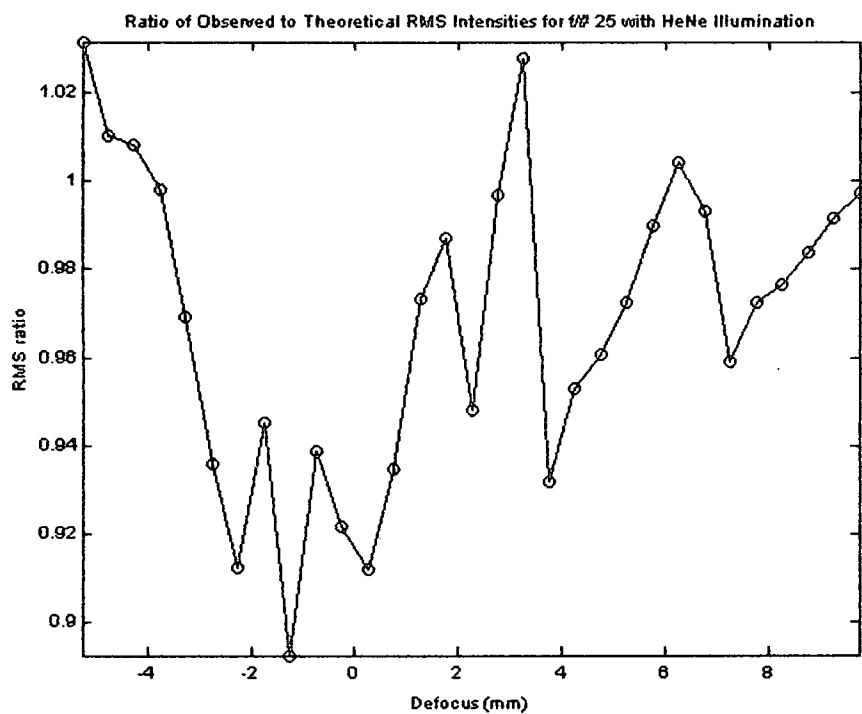


Figure 2-19: Ratio between Observed and Predicted RMS Intensities for $f/25$

CHAPTER 3

Imaging Defocus PSF and Image Restoration

Throughout this analysis, it is assumed that the imaging process is a linear one and can be characterized by a PSF. The image recorded by a sensor can then be treated as the convolution of this PSF with an “ideal” image. There is a considerable body of work on linear theory that can be exploited to retrieve this “ideal” image (For example [13] pgs. 261-270). It was decided to attempt to compute imaging PSFs rather than measure them and the method by which that was carried out is expounded upon here. The theory behind restoring images using a Wiener Filter as well as complications associated with restoring images are described as well.

3.1 Longitudinal Chromatic Aberration (LCA)

In all of the imaging systems examined (See Chapter 4), Longitudinal Chromatic Aberration (LCA) ([14], pg. 72-73), the variation of focal length with wavelength, was the dominant aberration as the system was defocused. It makes intuitive sense that the aberration defining how the focus for different wavelengths deviates from a single plane is important as the sensor is defocused. In particular, LCA causes the monochromatic PSFs to vary significantly with wavelength in a given plane on the z-axis. For example, the focal length of a thin lens with radii of curvature R_1 and R_2 and index of refraction, n , is ([14], pg. 74):

$$\frac{1}{f} = (n-1) \left(\frac{1}{R_1} - \frac{1}{R_2} \right) \quad (3-1)$$

However, the index of refraction varies with wavelength, $n = n(\lambda)$, and so the focal length varies with wavelength.

3.2 Imaging Defocus Point Spread Function (PSF)

The polychromatic PSF for narrowband incoherent illumination is the squared modulus of the monochromatic PSF associated with the center wavelength ([6] pg. 135). This assumes that the monochromatic PSFs are the same for all wavelengths in the band.

We provide a heuristic argument to extend this result to incorporate the effects of LCA. One can modify Goodman's derivation ([6] pgs. 131-135) by assuming the monochromatic PSFs vary with wavelength, that the light reflected from the object has a constant spectrum of $S(\lambda)$ across the object, and that the image fields corresponding to each wavelength vary independently from one another in time. This results in an incoherent polychromatic PSF that is proportional to the integral over the monochromatic incoherent PSFs weighted by the spectrum:

$$|u(x, y; z)|^2 \propto \int_{\lambda} S(\lambda) |U(x, y; \lambda, z)|^2 d\lambda \quad (3-2)$$

In Equation 3-2, $U(x, y; \lambda, z)$ corresponds to the defocus fields found from Equation 2-2 all evaluated in the same defocus plane even as both the distance to the image, d_i , and the defocus distance, Δz , vary with wavelength according to the effects of LCA. In effect, Equation 3-2 provides a polychromatic generalization of the monochromatic diffraction PSF. However, in most cases Equation 3-2 is merely an approximation because $S(\lambda)$ would vary over the imaged object. In this thesis, the representation of the LCA for an

imaging system that was used was the Focal Shift Curve. The focal shift is the distance the focus of a specific wavelength deviates from the focus of one reference wavelength. Figure 3-1 shows a sample computation of Equation 3-2 using the focal shift curve for the visible system detailed in Chapter 4.

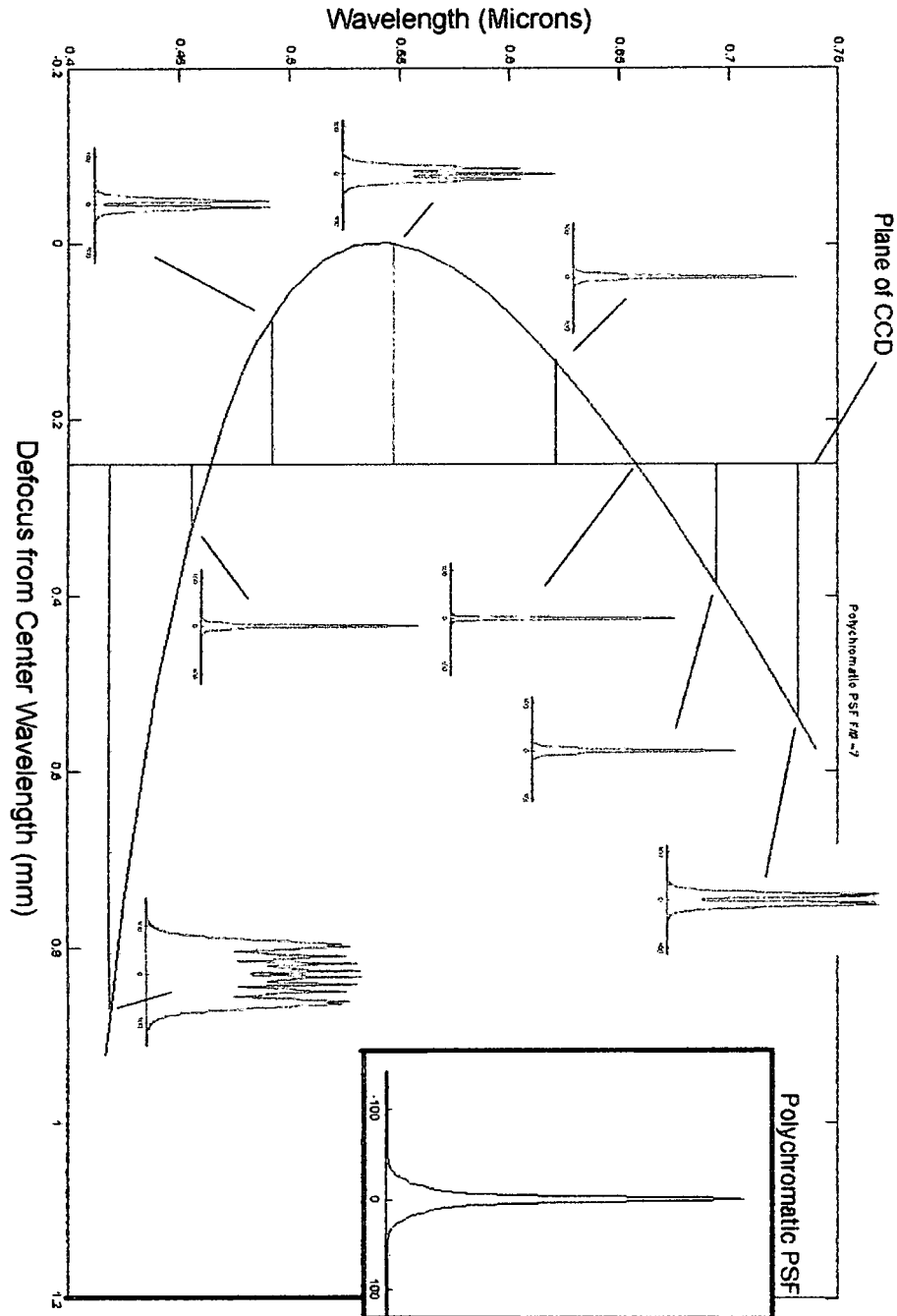


Figure 3-1: Sample Polychromatic Intensity PSF Computation (center wavelength of 532 nm)

In order to be able to make use of Equation 3-2, it is necessary to have an accurate model of how a sensor “sees” this polychromatic PSF and there are several pieces of information about the imaging system required to do that. Typically, each sensor has a unique wavelength dependant response curve, the Responsivity ([15] pg. 650-651), that describes the electrical current generated from incident optical power. The Responsivity is denoted here by the function $R(\lambda)$. Furthermore, the optics has a wavelength dependant transmission curve, the Transmittance ($T(\lambda)$), that describes the relative optical power transmitted. The other piece of information that is needed is the pixel dimensions where X is the horizontal spacing and Y the vertical spacing. It is assumed the fill factor is 100% between pixels. The defocus PSF as sampled by the sensor (Imaging Defocus PSF) is then given by

$$PSF(n,m;z) \propto \left(rect\left(\frac{x}{X}, \frac{y}{Y}\right) \otimes \int_{\lambda} S(\lambda)T(\lambda)R(\lambda)|U(x,y;\lambda,z)|^2 d\lambda \right) \Bigg|_{\substack{x=mX \\ y=nY}} \quad (3-3)$$

$$n = \dots -3, -2, -1, 0, 1, 2, 3 \dots$$

$$m = \dots -3, -2, -1, 0, 1, 2, 3 \dots$$

The $rect(\frac{x}{X}, \frac{y}{Y})$ function is a unit amplitude rectangle with width X , height Y , and center $(0,0)$. The proportionality sign can be replaced with equality by dividing by the summation of the PSF over all n and m values for normalization. In other words, the PSF as sampled by the sensor (Equation 3-3) is the integral over the monochromatic PSFs, weighted by the spectrum of the source illumination time the Transmittance of the optics times the Responsivity of the sensor convolved with the pixel PSF and then down-sampled to the pixel spacing of the sensor. It is a function of both the pixel coordinates as well as the z -axis coordinate that, in this paper, is the distance from the exit pupil of

the optics to the position of the sensor. Appendix B contains a Matlab function that computes the PSF defined by Equation 3-3.

Again, one issue that needs to be emphasized is that this PSF is likely an approximation because it assumes $S(\lambda)$ is not a function of spatial coordinates. Therefore, if there is significant chromatic variation over the object, the true PSF will vary spatially and the PSF in Equation 3-3 will be at best an approximation. Obtaining $S(\lambda)$ at each object point for simple black and white sensors for a random object seems impossible. For imaging systems for which a spectrum could be obtained at each pixel it would be possible to compute a more accurate space-varying PSF and possibly better restorations of defocused imagery could be obtained than presented in Chapter 4.

3.3 Image Restoration with Wiener Deconvolution Filters

The Wiener filter is a mathematically optimized filter designed to minimize the mean-square error between the restored (or “estimate”) image and the true image (See [1] pgs. 218-229 for derivation of the one dimensional Wiener filter and examples). Figure 3-1 shows a schematic for the observation and subsequent restoration. The “blur filter”, $h(x,y)$, in Figure 3-1 for this application is the imaging PSF.

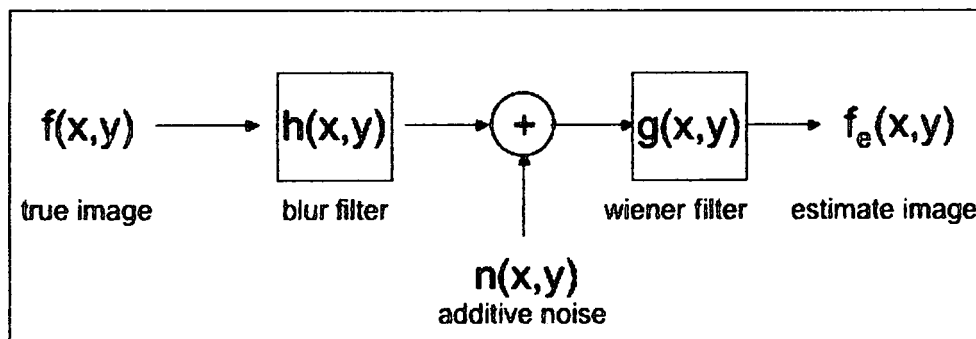


Figure 3-2: Observation and Restoration Model in the Space Domain

Figure 3-2 shows this process with continuous space variables. However, the recorded images are sampled, discrete, versions of the true intensity images and some complications arise from this fact. In order for the discrete processing of the sampled image to be equivalent to processing of the continuous image, the sampling process must satisfy the Nyquist Condition. This condition requires that the sampling frequency (number of pixels per unit length) be twice the cutoff frequency of the optics. If this condition is met, then by the Sampling Theorem the sampled image uniquely determines the continuous image it sampled ([12] pg. 176) and so long as the continuous imaging process is linear, then so is the discrete imaging process. If the Nyquist Condition is not met, then the system is not linear and can't be modeled as a convolution of a true image with a point-spread-function. In such a case, if an image has significant energy above the Nyquist Frequency then restoration using a linear method such as Wiener deconvolution could result in significant aliasing artifacts.

The two-dimensional Wiener deconvolution filter in the frequency domain is ([1] pgs. 390-391)

$$G(u,v) = \frac{H^*(u,v)}{|H(u,v)|^2 + \frac{P_n(u,v)}{P_f(u,v)}} \quad (3-4)$$

In Equation 3-4, $H(u,v)$ is the transfer function of the system, $H^*(u,v)$ is the complex conjugate of $H(u,v)$, and the functions $P_n(u,v)$ and $P_f(u,v)$ are the power spectral

densities (PSD) of the noise and true image respectively. So long as the ratio $\frac{P_n(u,v)}{P_f(u,v)}$ is

small (implying a high SNR) and the magnitude of the blur, $H(u,v)$, is not zero, the

Wiener filter is approximately an inverse filter at the frequency (u,v) . Although it is a

simplification, it is assumed that the PSDs of the image and noise are constants and

therefore the ratio $\frac{P_n(u,v)}{P_f(u,v)}$ is a constant, denoted Γ . This simplification is often assumed

because the power spectrums of the true image and of the noise are not known ([13] pg.

263). Typically Γ is varied manually to obtain the restored image of the highest quality.

Prior to restoration, it is necessary to pad the image to be restored. The reason is that multiplication in the frequency domain by means of the Discrete Fourier Transform (Known as the DFT – the transform utilized by Fast Fourier Transform algorithms) is equivalent to circular convolution. Circular convolution is less desirable than convolution as it couples pixel data from opposite edges of the image. Multiplication in the frequency domain more closely approximates a true convolution if the blurred image is pre-padded. That is, additional rows and columns of pixels must be added to the image ([1] pgs. 154-155). In this work, the padded rows and columns were filled with mirrored pixels from the original image. After padding, the restoration proceeds by taking the Fourier Transforms of the image and the computed PSF, computing G , multiplying the Fourier Transform of the image by G , and then inverse Fourier Transforming their product to obtain the padded restored image. The extra padded columns and rows are then stripped away.

Except in the most ideal cases, the Wiener filter provides more satisfactory results than the naïve inverse filter ($\frac{1}{H(u,v)}$) that disregards noise and the possibility of a zero in $H(u,v)$ (See [13] pg. 264 for a comparison). There are other comparable methods of restoration that could be considered ([13] pgs. 261-270), however, it was found

application of a Wiener filter produced satisfactory results (See Chapter 4) and, in addition, is much faster than iterative methods.

3.4 Quantitative Error Metric of Restoration

The motivation in defining a quantitative error metric is twofold. First, it provides insight into how the quality of the restored images decreases as defocus increases. Secondly and more importantly, the global minimum of $E(z)$ (Defined in Equation 3-6) was used to locate the image plane relative to the LCA curve for a given imaging system in Chapter 4.

Assuming that the Power Spectral Densities for the true image and for the noise are constants, it can be shown ([16]) that the Power Spectral Density (PSD) of the error between the true image and the estimate image is given by

$$SE(u,v;z) = SF \frac{\Gamma}{|H(u,v;z)|^2 + \Gamma} \quad (3-5)$$

In Equation 3-5, $SE(u,v)$ is the PSD of the error, SF is a constant approximating the PSD of the true image, and Γ is the ratio of the PSD of the noise to the PSD of the true image assuming both are constants. The Γ parameter is the Noise to Signal Ratio (NSR) with typical values from .1 to .001. The error metric made use of in this work is the fractional integrated PSD error:

$$E(z;\Gamma) = \frac{\iint SE(u,v;z) du dv}{\iint SF du dv} = \frac{\iint \frac{\Gamma}{|H(u,v;z)|^2 + \Gamma} du dv}{\iint du dv} \quad (3-6)$$

In Equation 3-6, z is the location of the sensor in relation to the exit pupil of the optics and the integrals are over spatial frequencies below the cutoff frequency of the optics.

The function $E(z)$ ranges from $\Gamma < E(z) < 1$ because $\Gamma \approx \frac{\Gamma}{1 + \Gamma} < \frac{\Gamma}{|H(u,v;z)|^2 + \Gamma} < 1$.

3.5 Effect of Zeros in the MTF on Image Restoration – Upper Bounds on Defocus

The Modulation Transfer Function (MTF) of an imaging system is the magnitude of the Fourier Transform of the PSF (given by Equation 3-3 in this paper) of the system ([6], pg. 139). The MTF is a function of the horizontal and vertical spatial frequencies and dictates how well the system “transfers” contrast associated with these frequencies. A value of one for a given spatial frequency means the system perfectly transfers that component while a value of zero means the system does not transfer that component at all (a sine wave at that frequency would be mapped to a constant).

Once defocus is great enough, the MTF obtains zeros ([6] pgs. 150-151). That is, at certain spatial frequencies less than the cutoff frequency of the optics, the magnitude of the transfer function is zero. With increasing defocus, the spatial frequencies at which zeros occur decreases – eventually moving below the Nyquist frequency of the optics if they started above it. Thus, if the true image has components at one of those spatial frequencies, that information is lost in the imaging process (The actual image is the convolution of the “true” image with the imaging PSF). Note that while Equation 3-3 contains a convolution with the pixel PSF of the sensor, the sensor transfer function does not add zeros to the MTF itself. A trivial derivation shows that the Fourier Transform of a rect function of width L (1-dimensional model of a pixel) is a sinc function with its first

zero at the frequency $f = \frac{1}{L}$. However, the Nyquist rate for such a rect is $f_N = \frac{1}{2L}$.

Hence, the zeros that the pixel transfer function would contribute are irrelevant because the imaging system does not transfer those frequency components.

Restoration of an image with a Wiener deconvolution filter can still be performed even when there are zeros in the MTF. However, the restored image can be distorted due to the loss of spatial frequency components of the true image through the imaging process. For this reason the application of a Wiener deconvolution filter to defocused images for which the MTF does not have zeros provides more satisfactory estimate images than if the MTF did have zeros. A contrived 1-D example of zeros in a transfer function resulting in a distorted restored image is provided in Figure 3-3 as motivation. A rectangle was blurred using two similar transfer functions save that one goes to zero and the other doesn't. The resulting restored images show a dramatic difference with the estimate image restored from the transfer function with a zero exhibiting substantial distortions. Therefore, in analyzing specific imaging systems in Chapter 4, the defocus distances for which the first new zeros in the MTF occurred are taken as practical upper bounds on defocus.

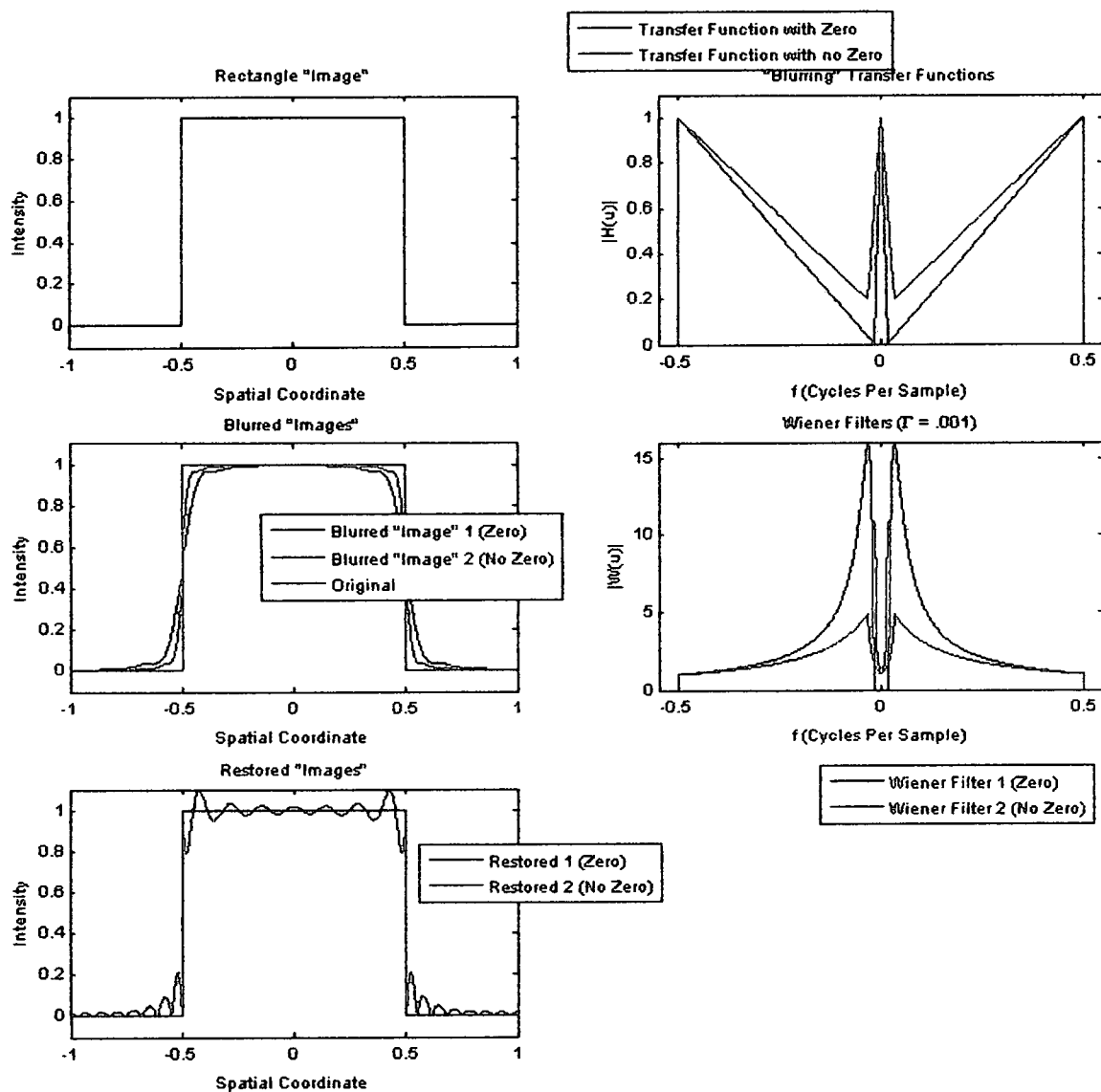


Figure 3-3: 1-D Example of Distorted Restored Images Caused by Zeros in the Transfer Function

CHAPTER 4

Application to Imaging Systems

The defocused imaging and restoration model represented by Chapters 2 and 3 were applied to two imaging systems: a simple visible imaging system consisting of one achromatic doublet and a Silicon board CCD and a prefabricated MWIR ultra narrow field of view imager consisting of many optical components and an InSb FPA.

Each system was modeled with the optical modeling software Zemax so that the longitudinal chromatic aberration could be obtained. The Transmittance for both imaging systems was assumed to be a constant over imaging wavelengths. In the case of the visible system this was justified from the specifications of the lens in that the Transmittance was over 95% over imaging wavelengths. For the MWIR system it was assumed without justification and could be a source of error. Along with the spectral response curve (relative Responsivity) and the assumption that the illumination was incoherent white light, this allowed for the defocused imaging PSF (Equation 3-3) to be computed for incremental positions for the sensor in relation to the focal shift curve (the LCA curve). The error metric defined in Equation 3-6 could then be computed, the minimum of which was assumed to be the in-focus image plane. Locating the in-focus image plane in relation to the focal shift curve was of vital importance in appropriately connecting the defocus model to experimental image data. The defocus locations for

which new zeros in the MTF occur were also noted. These positions were determined by manual inspection of the computed MTFs (magnitude of the Fourier transform of the computed PSFs) as defocus was varied. Incrementally defocused image data through focus for each system were then restored with the computed PSFs and by application of a Wiener deconvolution filter.

4.1 Visible Imaging System Specification and Characterization

The visible imaging system, represented in Figure 4-1, used a Newport PAC088 250 mm focal length (in this configuration the distance to the image was 278 mm) achromatic doublet to image incoherently illuminated opaque objects onto a Sony ICX408AL board CCD with pixels dimensions of 7.5x6.4 microns.

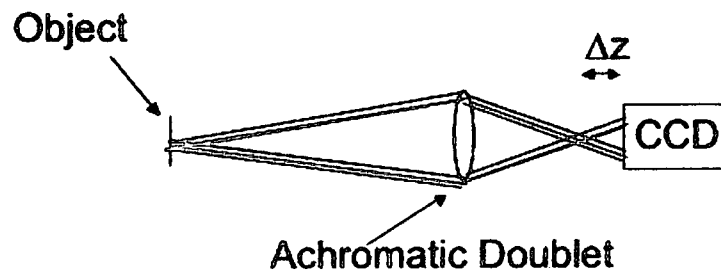


Figure 4-1: Defocused Visible Imaging System

This 2-inch diameter lens provided an $f/6.78$ imaging system (a portion of the outer diameter of the lens was blocked by the lens holder). A tube and cloth were used to keep stray light not originating from the object (2405 mm object distance) from reaching the CCD. For the visible system, all components were stationary except the sensor whose location was incremented through focus. The modeled focal shift curve is shown in Figure 4-2 and the spectral sensitivity of the sensor in Figure 4-3.

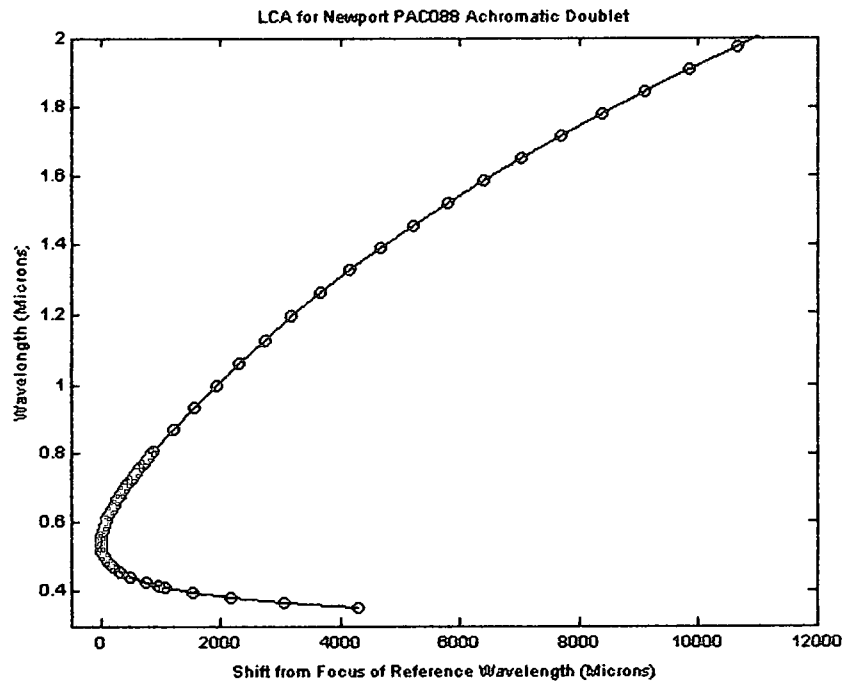


Figure 4-2: Newport PAC088 Achromatic Doublet Modeled Focal Shift Curve

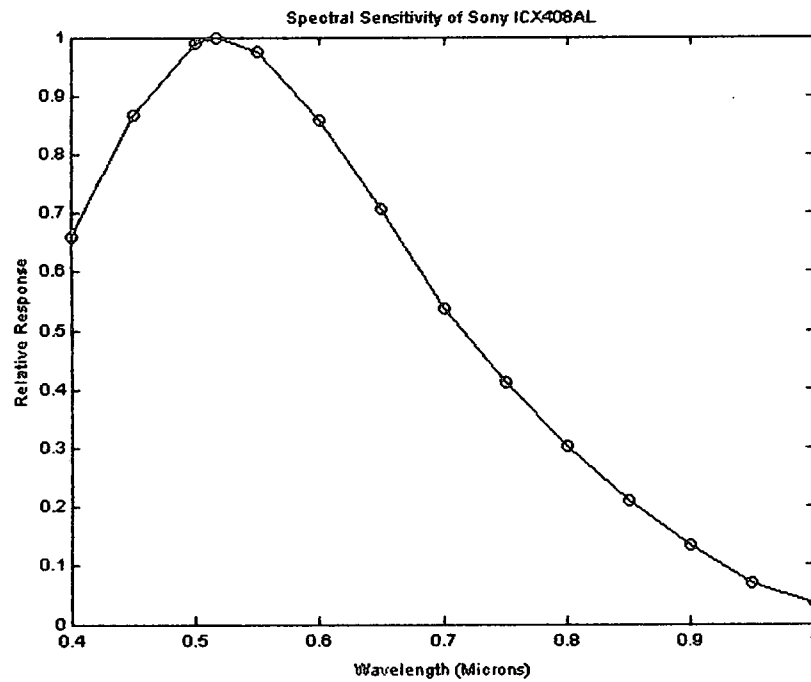


Figure 4-3: Relative Spectral Response for Sony ICX408AL CCD

The location of the image plane relative to the focal shift curve, the location of the defocus positions at which zeros appeared in the MTF, and a plot of the error metric defined in Equation 3-6 are in Figure 4-4. The values of the important distances are in Table 4-1.

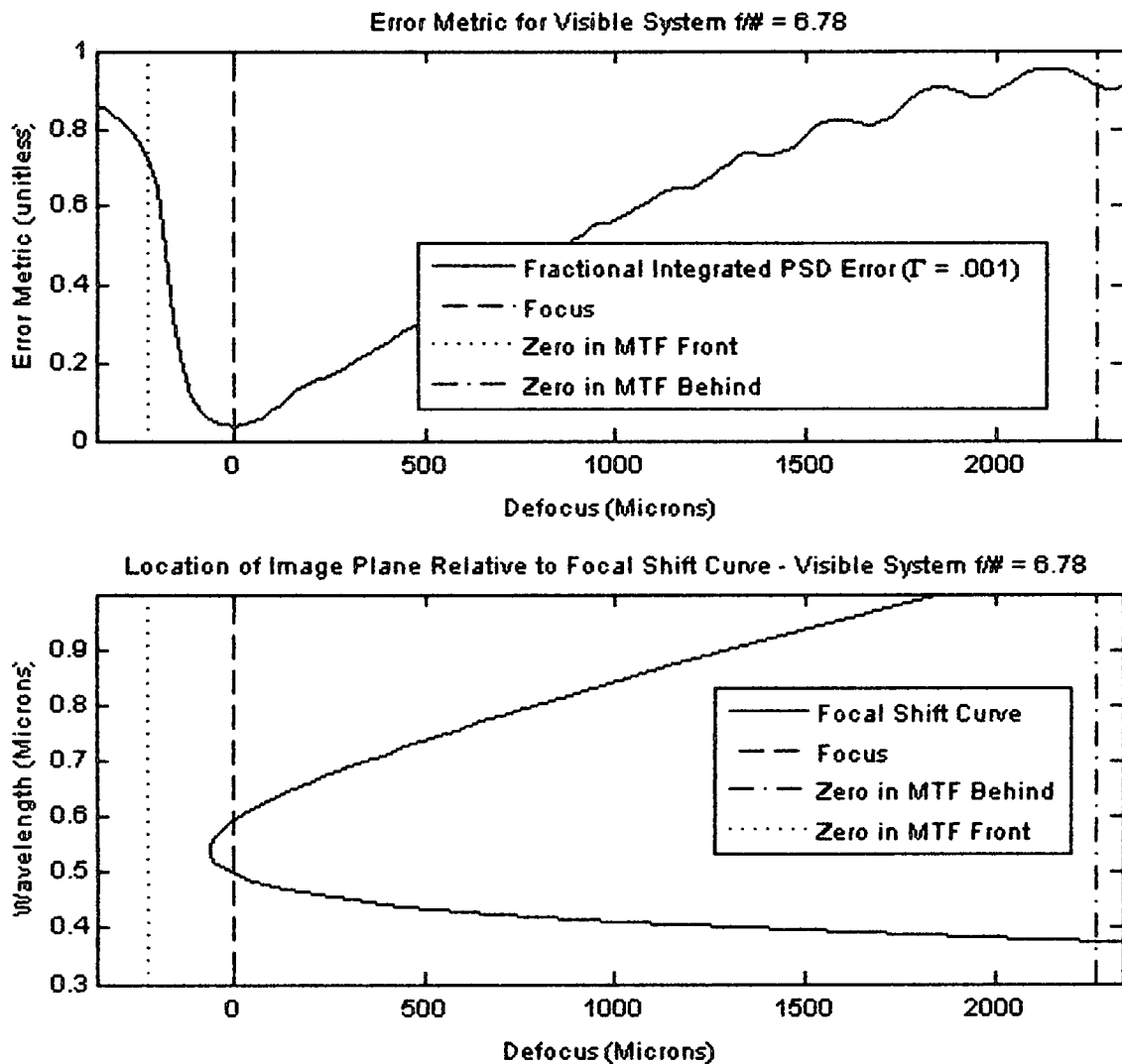


Figure 4-4: Visible System Model Analysis

The location of the first zeros appearing in the MTF in front of the image plane and behind the image plane are asymmetric due to the asymmetry of the focal shift curve. That is, the first zero in front of the image plane occurs much closer to the image plane

than the first zero behind the image plane because there are wavelengths in focus for distances far behind the image plane. This can be seen from the bottom of the two plots in Figure 4-4. In addition, although it is not pictured in Figure 4-4, the fractional integrated PSD error varies with Γ . From Section 3-4, Equation 3-6 gives the fractional integrated PSD error:

$$E(z;\Gamma) = \frac{\iint SE(u,v;z)dudv}{\iint SFdudv} = \frac{\iint \frac{\Gamma}{|H(u,v;z)|^2 + \Gamma} dudv}{\iint dudv}$$

In the limit as $\Gamma \rightarrow 0$ (very low noise system) we have $E(z;\Gamma \rightarrow 0) = 0$ which holds so long as the MTF does not contain a zero. As $\Gamma \rightarrow 0$ the error curve in Figure 4-4 would approach zero for defocus values in between the locations of the zeros in the MTF. Upon reaching these zeros, the error metric would increase sharply and begin to approach 1. In the limit $\Gamma \rightarrow \infty$ (very high noise system) we have $E(z;\Gamma \rightarrow \infty) = 1$ everywhere. There is a family of curves bounded by these limiting cases with a lower Γ for a given imaging system translating into a larger effective defocus range (bounded by location of zeros).

Table 4-1: Important Visible System Distances

Location of 1 st Zero in MTF in Front of Image Plane	Location of Image Plane Relative to Reference Wavelength Focus (550 nm)	Location of 1 st Zero in MTF in Front of Image Plane
-226.9 +/- 22.7 Microns	63.02 +/- 22.7 Microns	2270 +/- 22.7 Microns

Figure 4-4 was generated from 12,000 computations of the Fresnel Defocus Diffraction Integral (Equation 2-1) using the algorithm presented in Section 2-2 and the subsequent computation of the defocused imaging PSF (Equation 3-3) with defocus distances from the image plane ranging from -400 microns to +2500 microns (The range was selected so as to contain both of the positions at which zeros in the defocus MTF appear) and an

increment of about 22.7 microns. The values of relevant parameters used in generating Figure 4-4 were $\tau = .05$, $\varepsilon = .05$, and $\Gamma = .001$ where ε and τ are defined in Section 2-2. The number of radial points sampled per computed PSF was 150 (before down-sampling to the pixel frequency of the sensor). This was chosen so that the cutoff of the optics was below the Nyquist frequency.

Figure 4-5 shows horizontal cross-sections of the computed imaging PSFs for select defocus positions and Figures 4-6 through 4-11 show horizontal cross-sections of the associated MTFs. The MTF plots show the optical MTFs, the system MTFs, and the effective MTFs upon Wiener deconvolution.

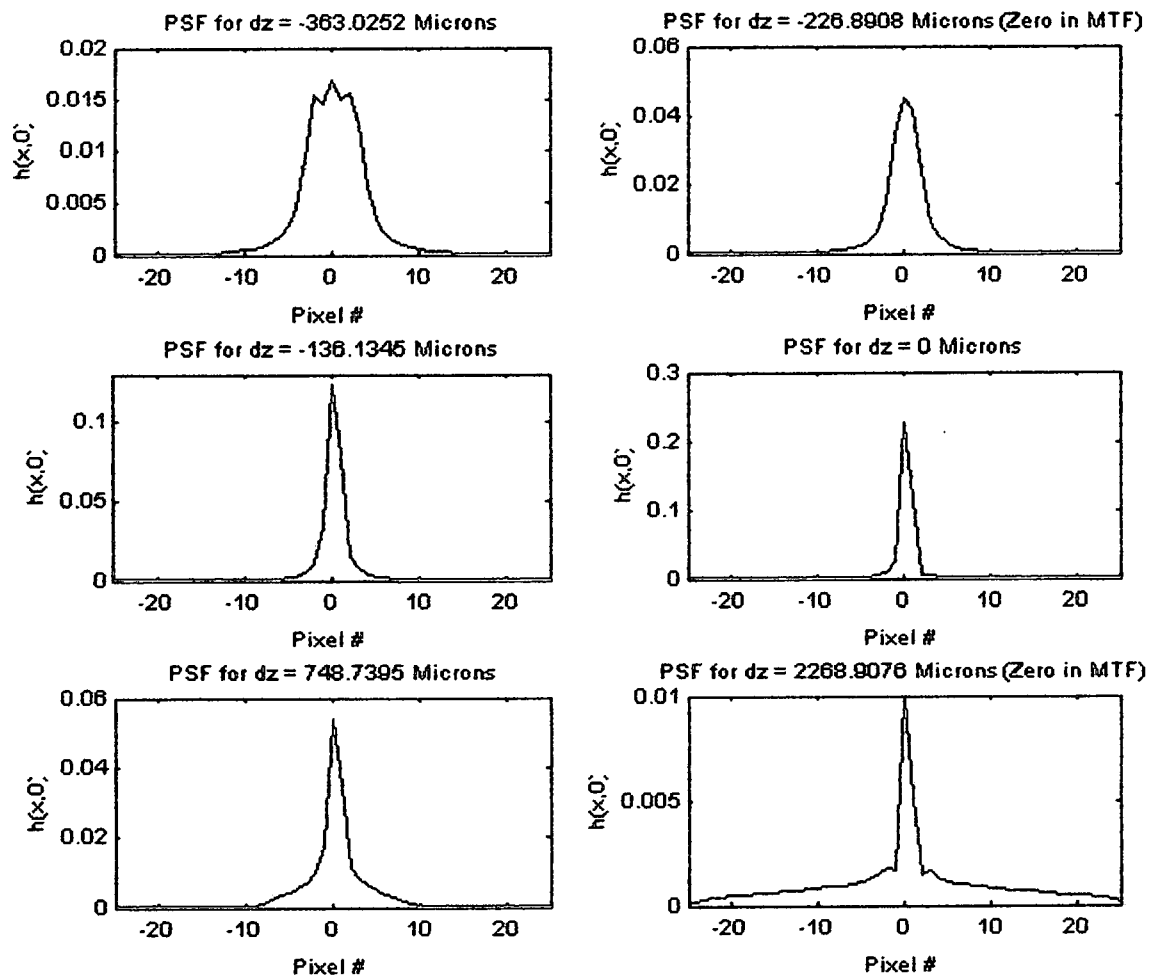


Figure 4-5 Horizontal Cross Sections of Modeled Imaging Defocus PSFs

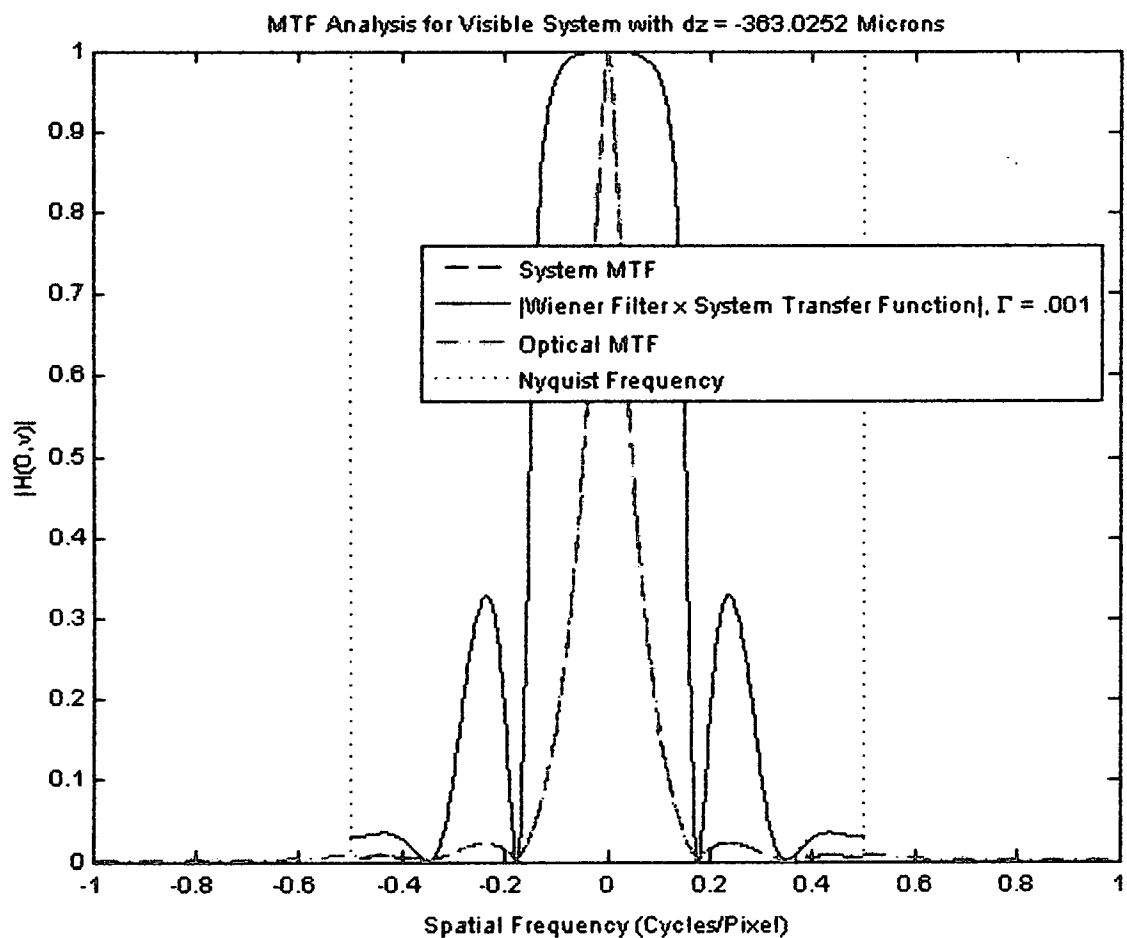


Figure 4-6: Modeled Defocus MTF for Visible System with $dz = -363$ Microns

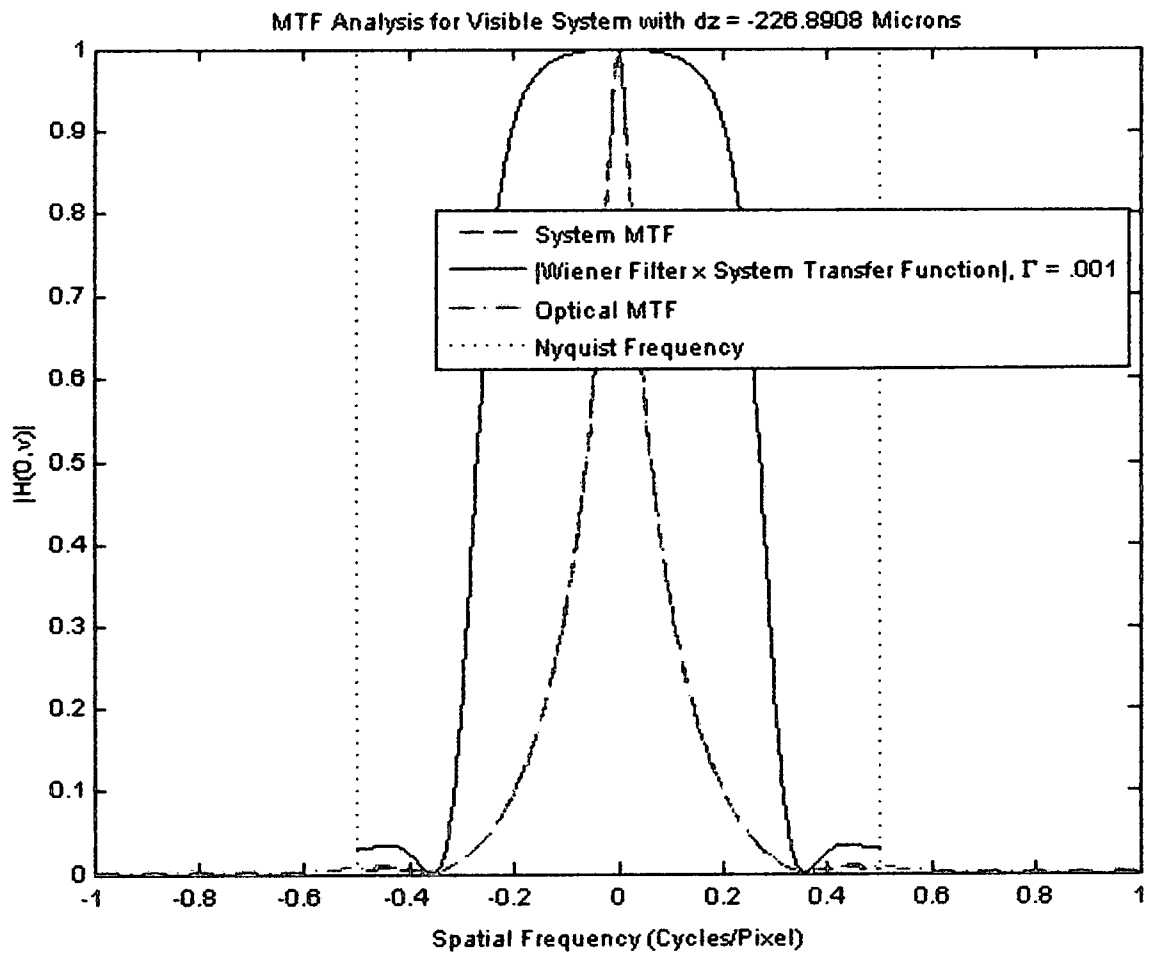


Figure 4-7: Modeled Defocus MTF for Visible System with $dz = -227$ Microns (1st Zero in MTF)

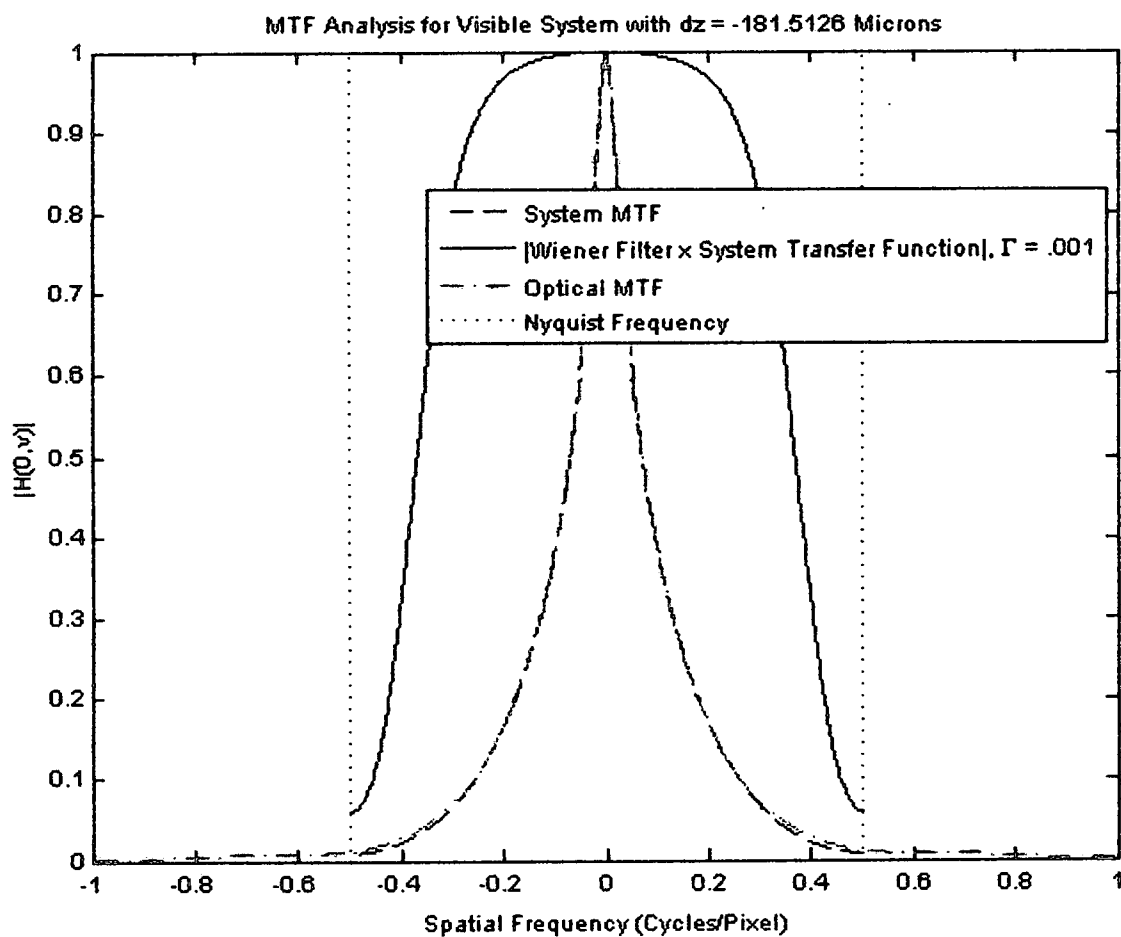


Figure 4-8: Modeled Defocus MTF for Visible System with $dz = -182$ Microns

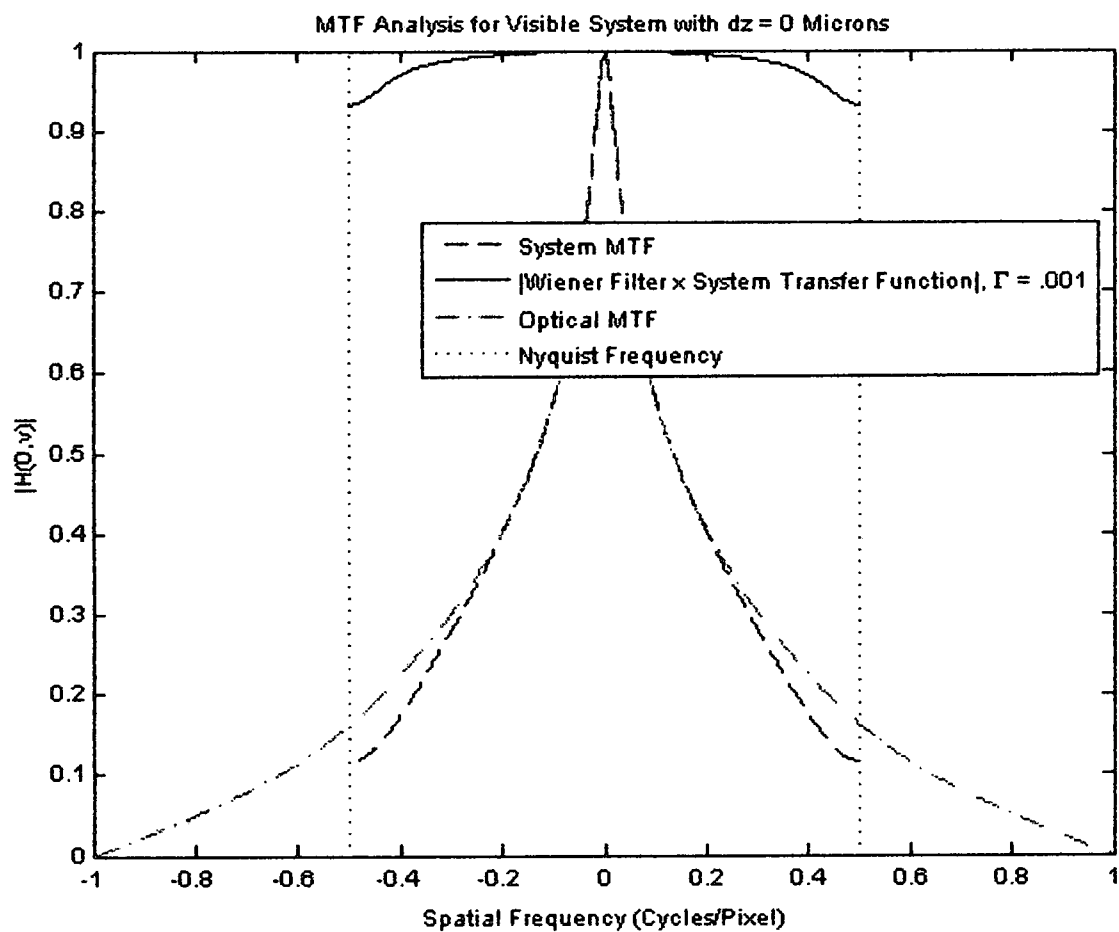


Figure 4-9: Modeled Defocus MTF for Visible System with $dz = 0$ Microns

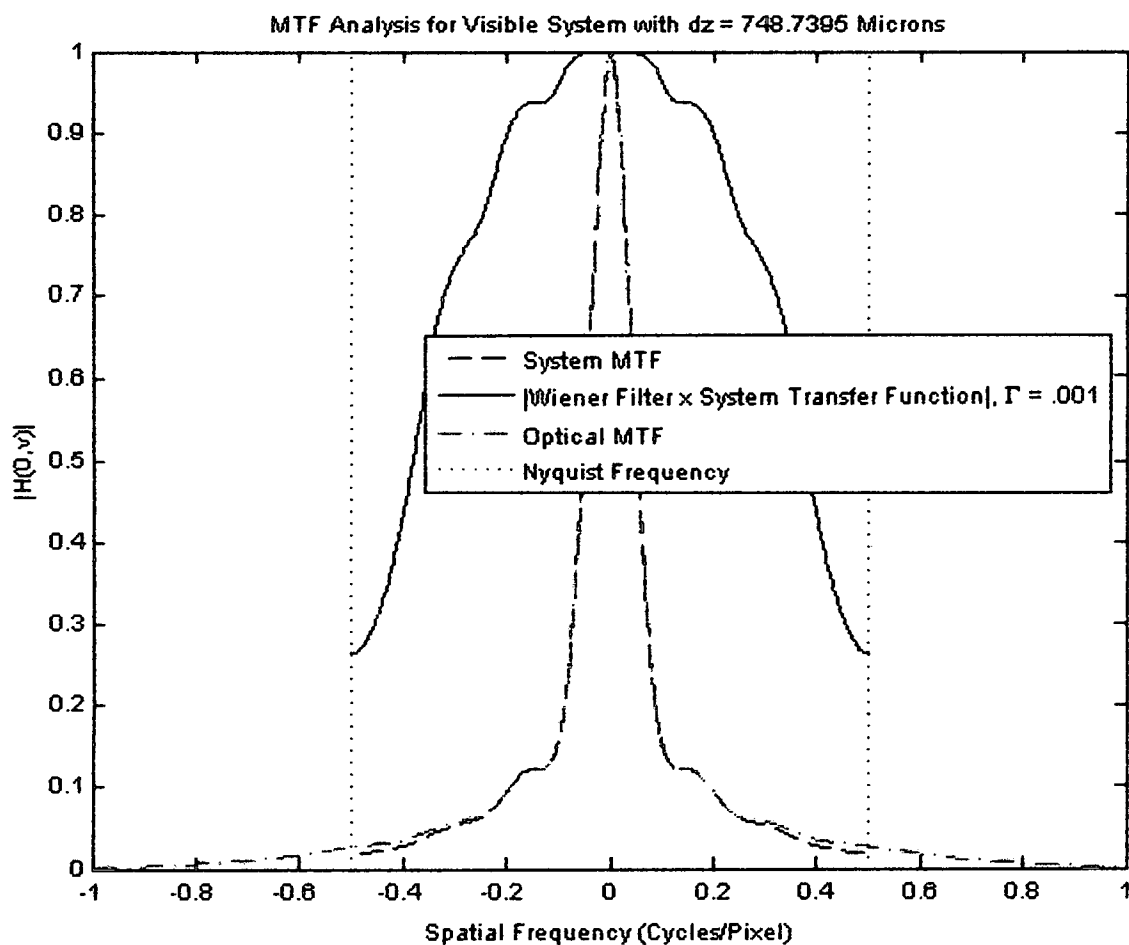


Figure 4-10: Modeled Defocus MTF for Visible System with $dz = 749$ Microns

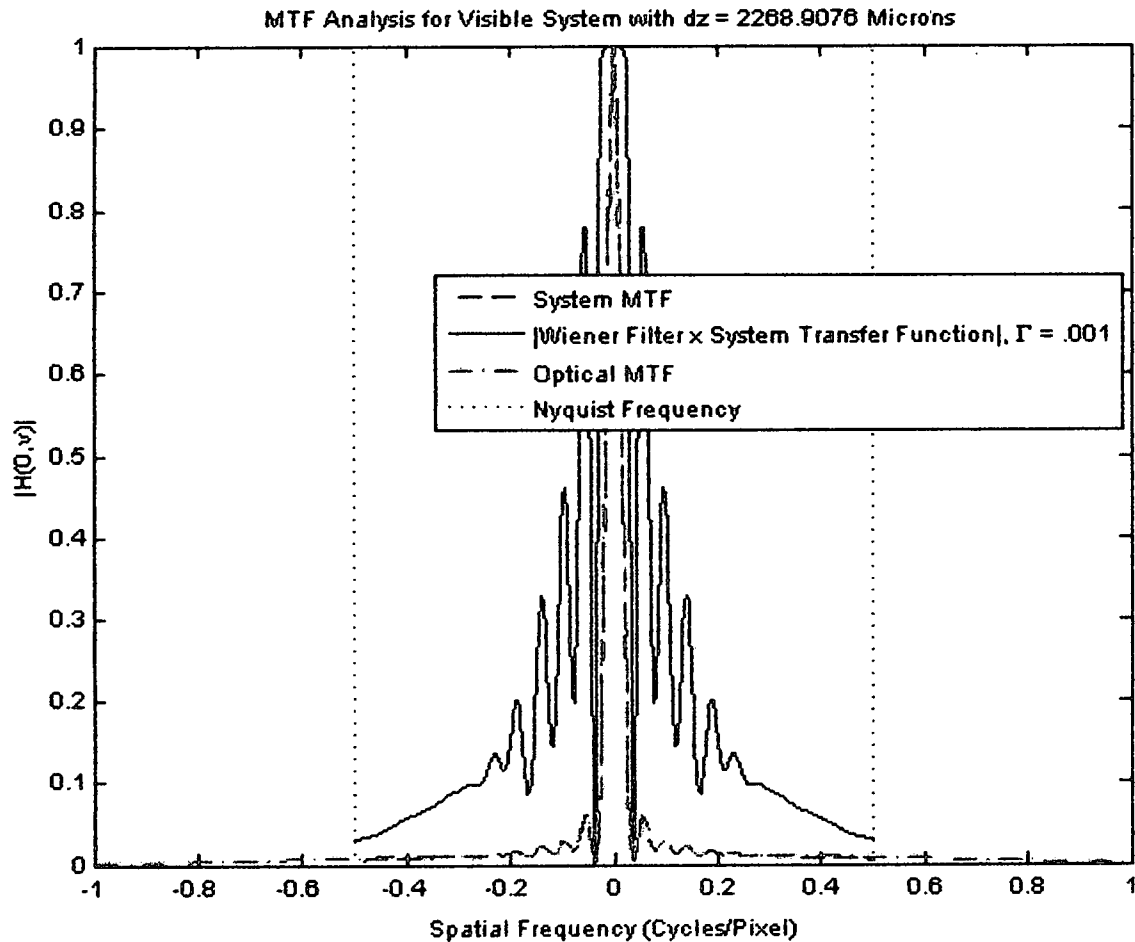


Figure 4-11: Modeled Defocus MTF for Visible System with $dz = 2269$ Microns (1st Zero in MTF)

From Figures 4-6 through 4-11, it can be seen that other than for planes close to the image plane the optical MTF obtains only vanishingly small values above the Nyquist frequency and it is therefore expected aliasing will not be a major factor in the restoration (See Section 3-3 for discussion). It can also be seen that for defocus positions near the image plane, the effective MTF upon restoration can be better than the diffraction-limited MTF. Figures 4-7 and 4-11 show the MTFs for the defocus positions for which new zeros first appear in front and behind the image plane.

4.2 Results of Restoring Imagery from the Visible System

A Bar Target and a Circuit were imaged by the visible system with the defocus distance incremented by 25 microns through image focus. A Bar Target was selected because a black and white object should satisfy the assumption of a constant reflected spectrum required for Equation 3-3 to be accurate. A Circuit was selected for comparison because it has chromatic variation and finer detail. For both sets 100 images for each defocus position were averaged to produce high SNR imagery. The defocused imagery was restored using Wiener deconvolution filters following the procedure outlined in Section 3.3. The Matlab file used to implement the Wiener filter is given in Appendix C. The PSFs used in the restorations were generated in an identical fashion as those in Figure 4-5 and with the same input parameters except for the defocus distances.

Figures 4-12 through 4-25 show 256x256 square pixel sections of the defocused imagery, the restored imagery, and the in-focus image for reference. Each set of figures step through increasing z-distances starting before focus and ending after focus. Figures 4-26 through 4-29 then show full-page images for select blurred and restored images of the circuit object. Note that restored images for defocus distances within the range defined by setting the locations of the first zeros in the defocused image MTF as upper bounds (See Table 4-1) exhibit severe image distortions relative to the in-focus image. Restored images within these bounds are less distorted, although the quality does decrease with increasing defocus as expected from the MTFs in Figures 4-6 through 4-11 and from the error metric plotted in Figure 4-4.

In general, restored images taken from defocus positions where there is a zero in the MTF exhibit ringing effects (See Figure 3-3). The severity and wavelengths of the

distortions in the restored images is largely a function of the number of zeros in the MTF and of the spatial frequencies at which the zeros occur – the lower the spatial frequency the worse the distortions. The reason is that most of the content in an image contains lower frequency information while some of the content might not contain higher frequency information and could be unaffected by higher spatial frequency zeros. For defocus positions at which there are no zeros in the MTF, the restored images should approximate the in-focus image (or even obtain superior quality to the in-focus image) to varying degrees. The overall quality of the restored images should decline as the defocus position approaches the first zeros in the MTF on either side according to how the MTF changes (See Figures 4-6 through 4-11).

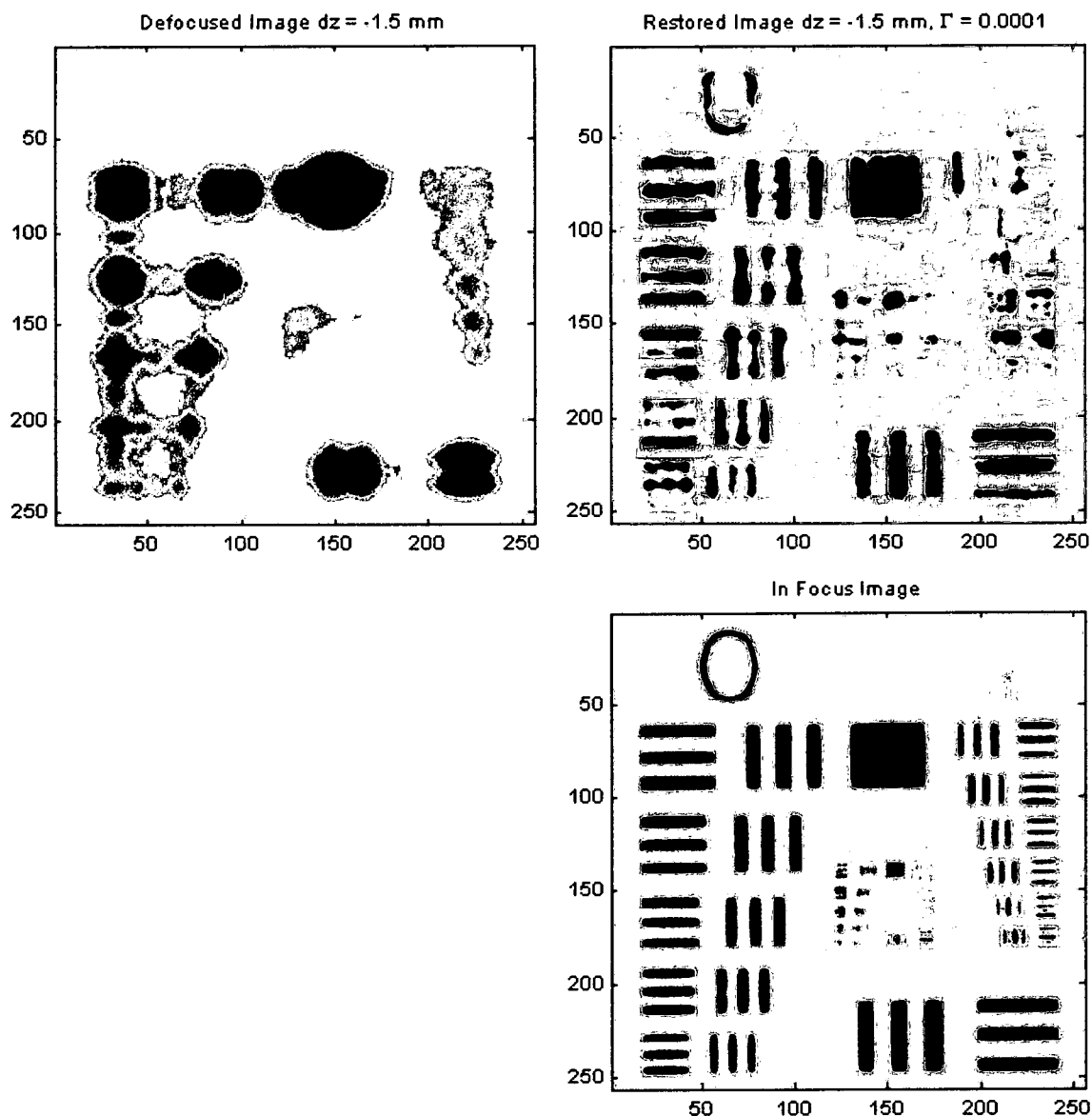


Figure 4-12: Bar Target, $dz = -1500$ Microns

The defocus position for Figure 4-12 was $dz = -1500$ microns while the first zero in the MTF occurs at $dz = -226$ microns. The MTF associated with this position would have more zeros and at lower spatial frequencies than the modeled MTF shown in Figure 4-6. Therefore, it would be expected that the restored image would be highly distorted in comparison to the in-focus image and this is what is seen.

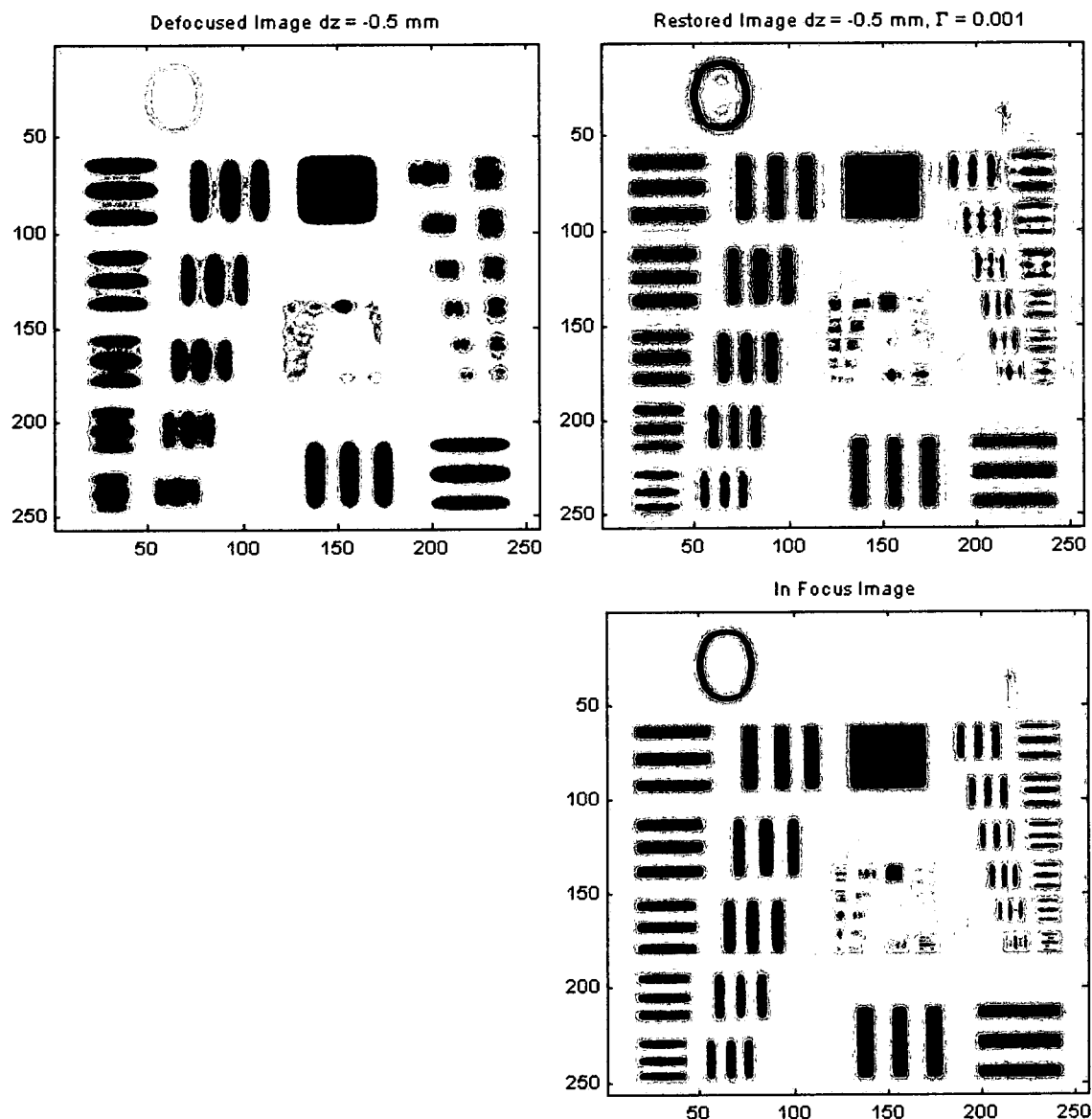


Figure 4-13: Bar Target, $dz = -500$ Microns

The defocus position for Figure 4-13 was $dz = -500$ microns while the first zero in the MTF occurs at $dz = -226$ microns. The MTF associated with this position would be slightly more attenuated than the modeled MTF shown in Figure 4-6. The zeros in the MTF are at higher frequencies than those in the MTF for Figure 4-12 and it would be expected the ringing would be at shorter wavelengths and distortions to be less severe.

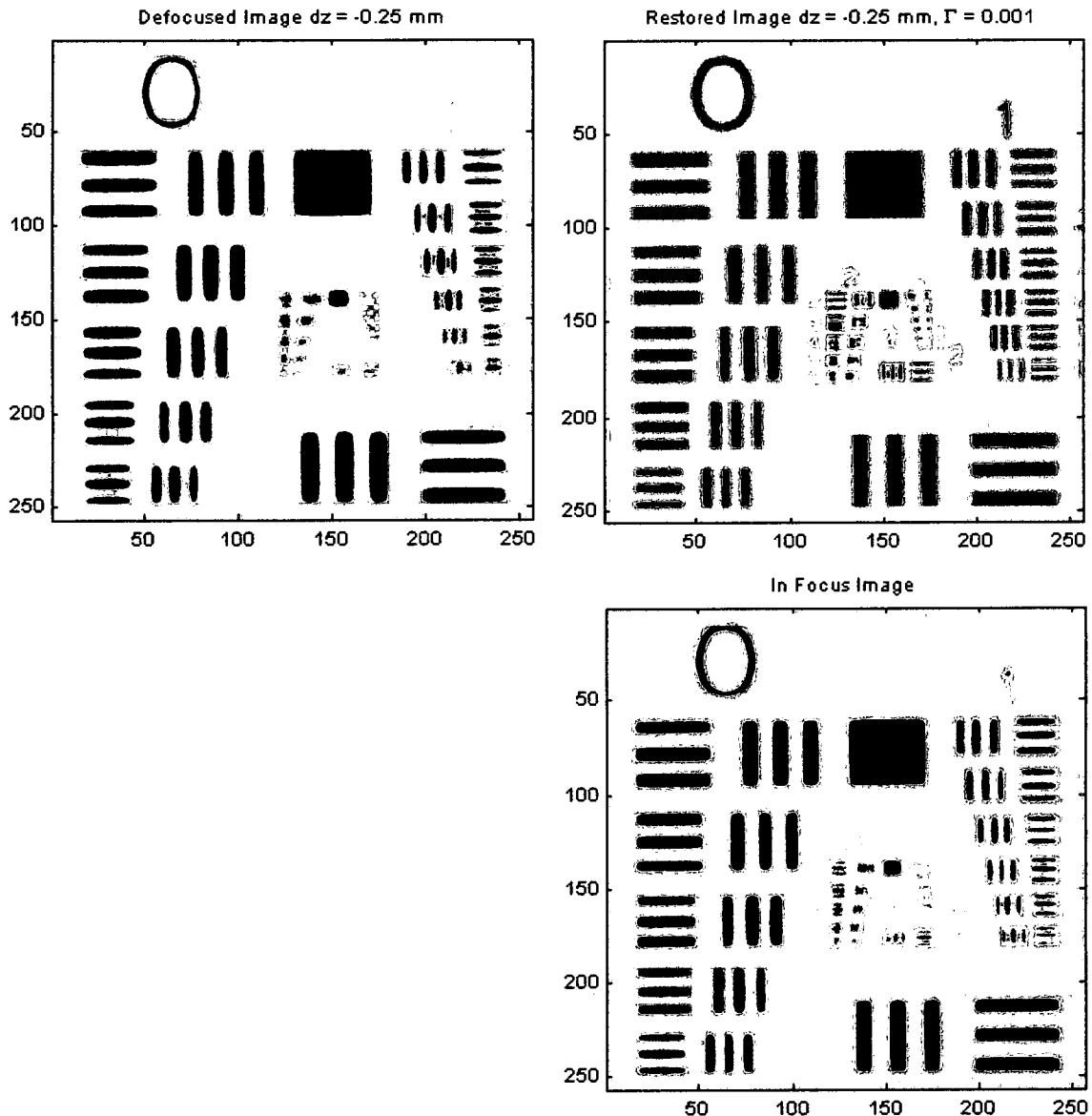


Figure 4-14: Bar Target, $dz = -250$ Microns

The defocus position for Figure 4-14 was $dz = -250$ microns while the first zero in the MTF occurs at $dz = -226$ microns. The MTF associated with this position would be similar to the modeled MTF shown in Figure 4-7. This defocus position is near the first occurrence of a zero in the MTF which occurs at a relatively high spatial frequency. It would be expected that the restored image might exhibit small amounts of ringing at a small wavelength, but otherwise look like the in-focus image. This is what is seen.

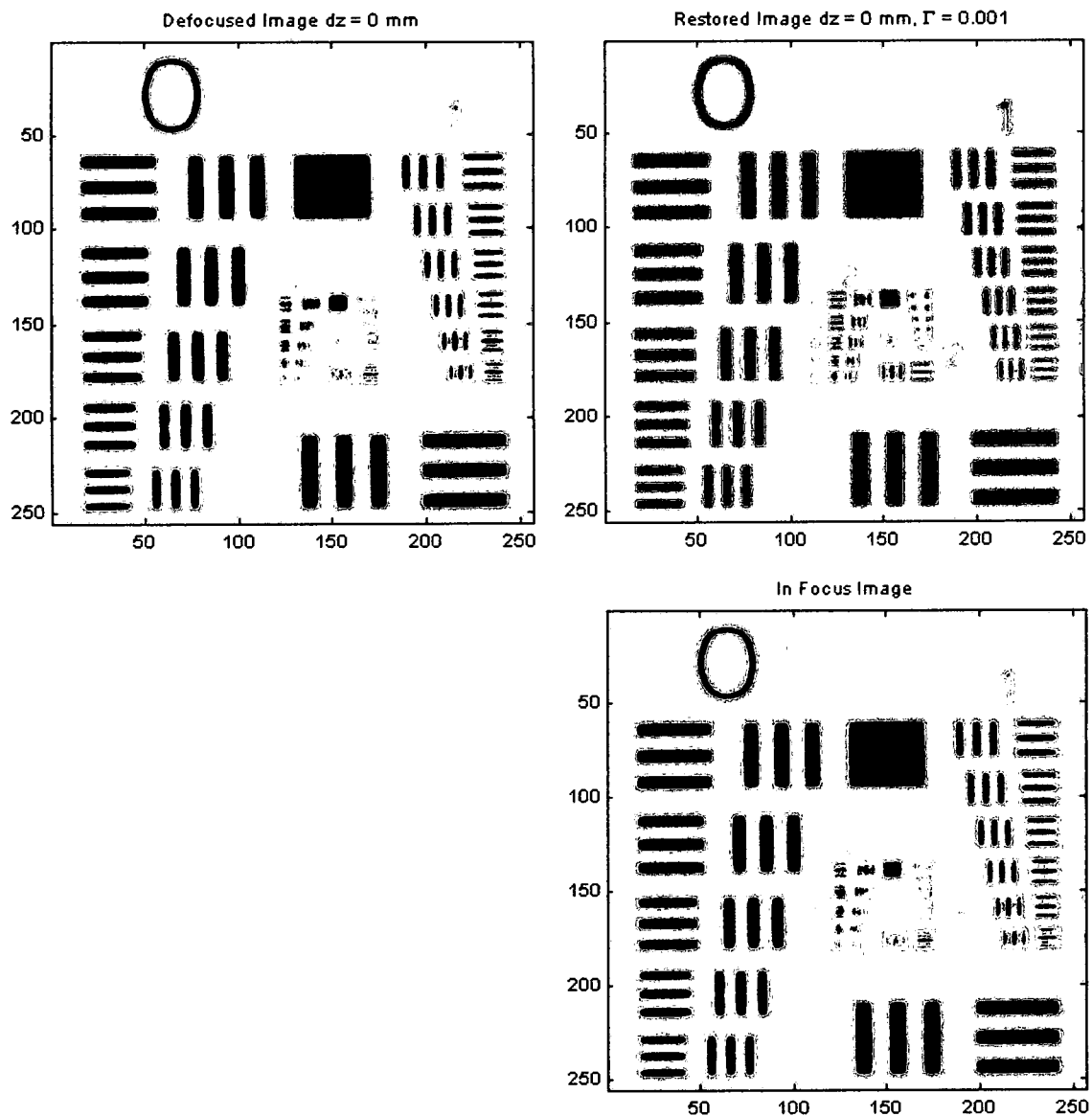


Figure 4-15: Bar Target, Image Plane

The defocus position for Figure 4-15 was $dz = 0$ microns (focus) while the first zero in the MTF occurs at $dz = -226$ microns. The MTF for this position should be similar to the MTF modeled in Figure 4-9 and the restored image should therefore exhibit slightly higher contrasts for all spatial frequencies than the in-focus image. The restored image is effectively the diffraction corrected in-focus image.

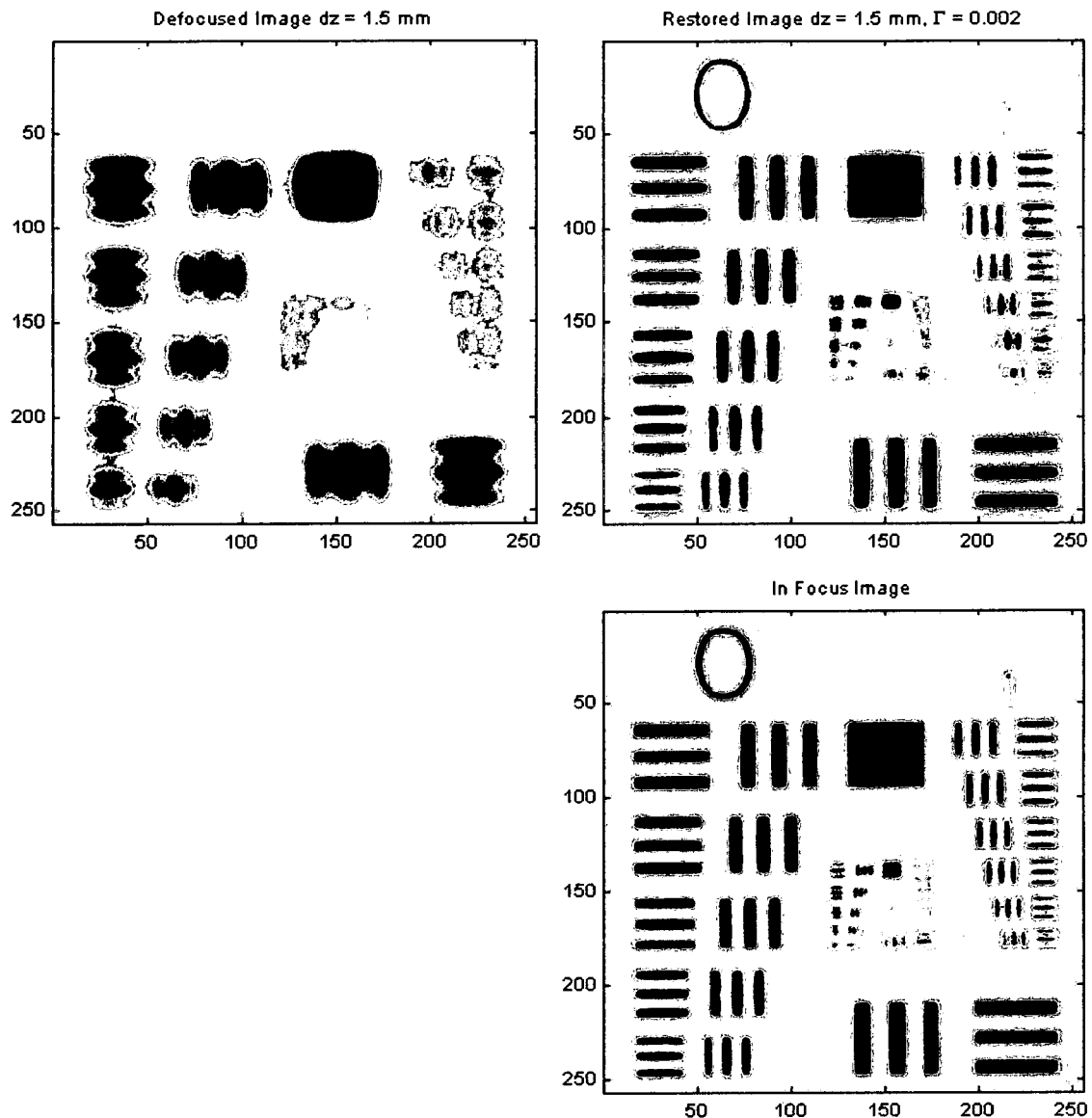


Figure 4-16: Bar Target, $dz = 1500$ Microns

The defocus position for Figure 4-16 was $dz = +1500$ microns while the first zero in the MTF occurs at $dz = 2270$ microns. The MTF associated with this position would be between the modeled MTFs in Figures 4-10 and 4-11. There are no zeros in this MTF, however, the magnitude of the MTF for many spatial frequencies is low. Therefore, it is expected the restored image should approximate the in-focus image but with diminished contrast.

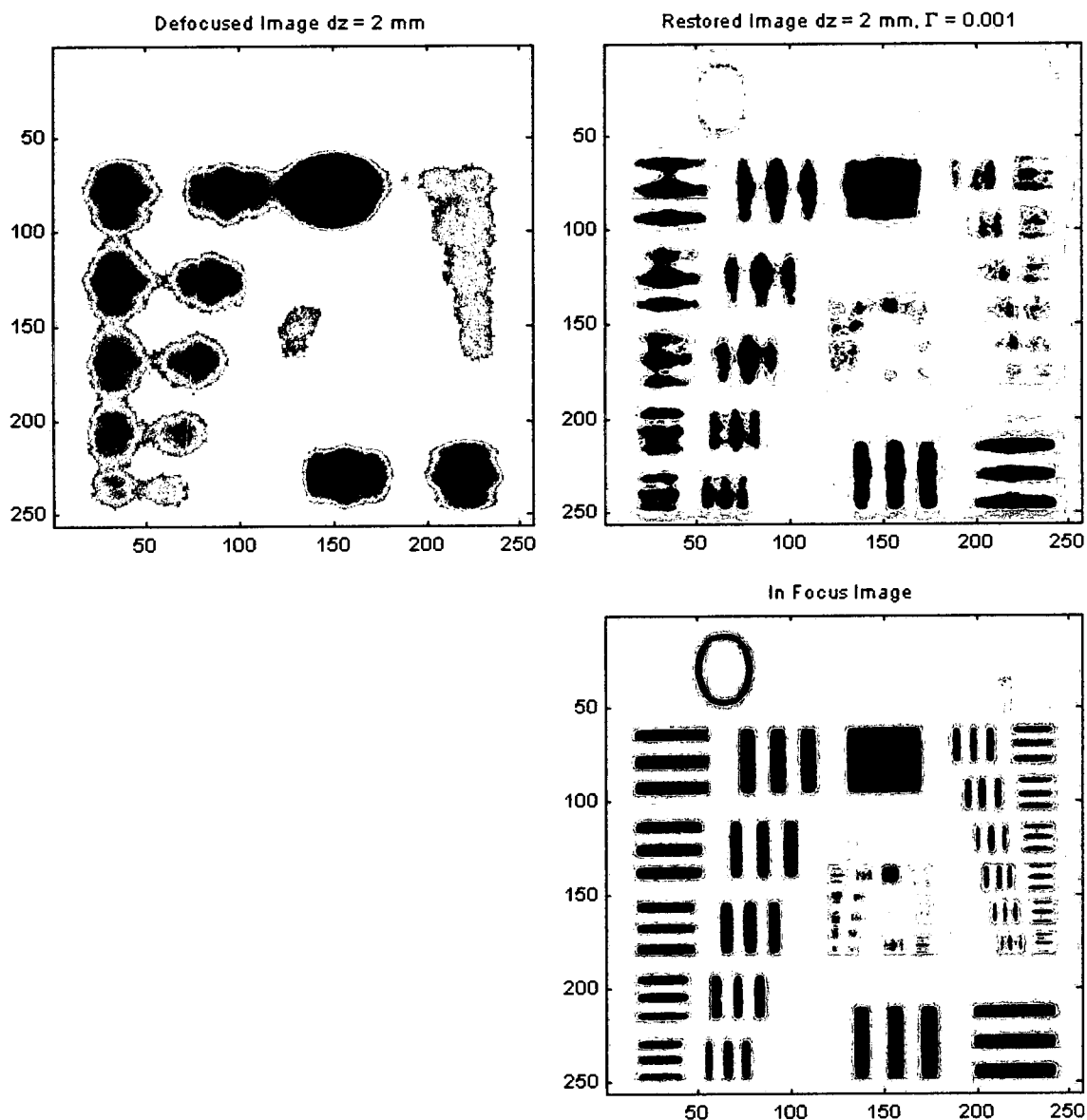


Figure 4-17: Bar Target, $dz = 2000$ Microns

The defocus position for Figure 4-17 was $dz = +2000$ microns while the first zero in the MTF occurs at $dz = 2270$ microns. The MTF associated with this position would be similar to the modeled MTF in Figure 4-11 but without the zero. It is expected the restored image should approximate the in-focus image but with an even further diminished contrast than Figure 4-16.

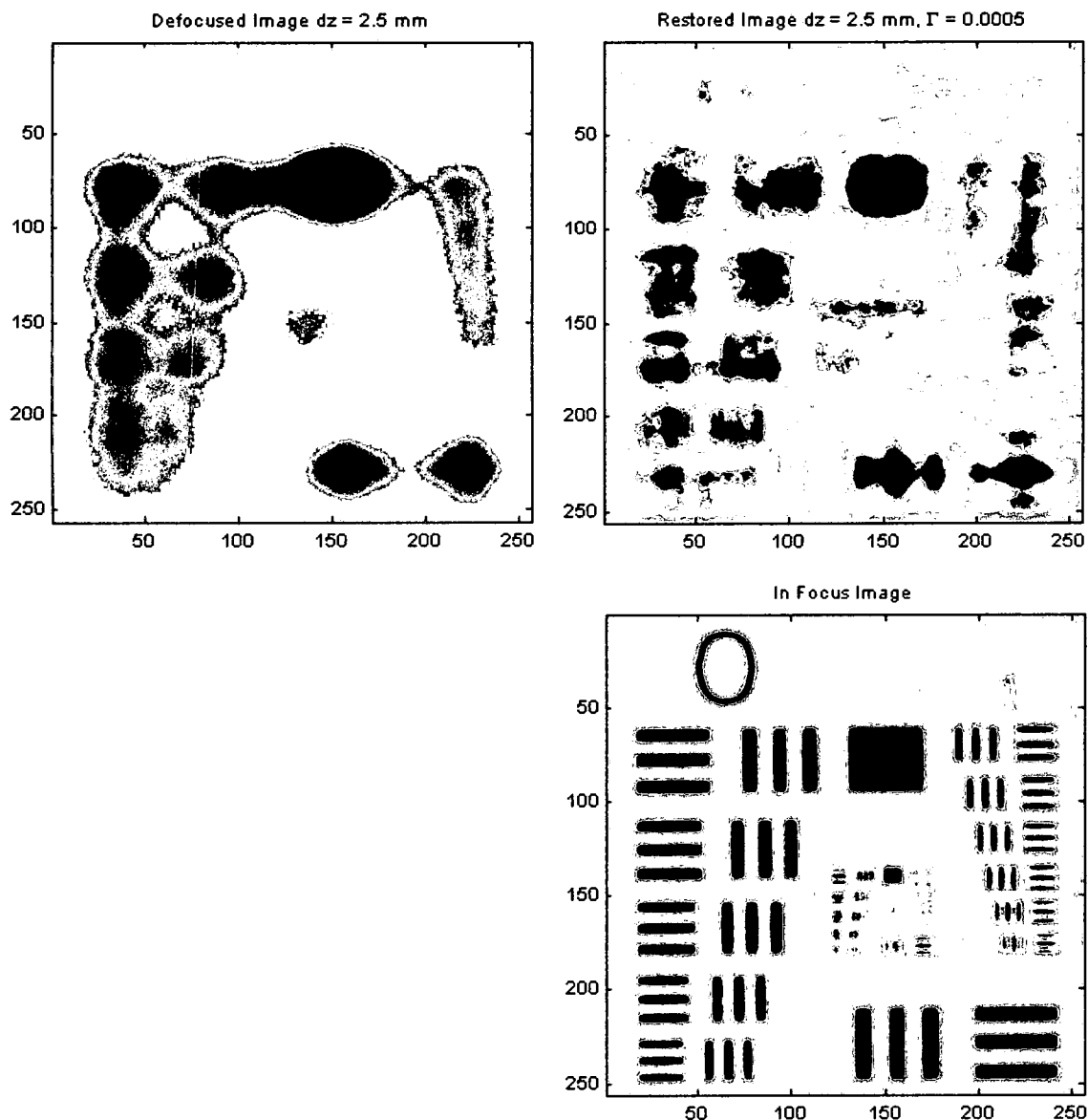


Figure 4-18: Bar Target, $dz = 2500$ mm

The defocus position for Figure 4-18 was $dz = +2500$ microns while the first zero in the MTF occurs at $dz = 2270$ microns. The MTF associated with this position would be similar to the modeled MTF in Figure 4-11. There is a zero in the MTF at this defocus position and from Figure 4-11 it appears at a low spatial frequency. Therefore, it is expected the restored image will be a highly distorted version of the in-focus image.

The circuit image series shows similar results to the bar target series except that

the image quality appears to decrease at a faster pace with defocus. There are several possible reasons for this. The first possibility is that the chromatic variation in the object caused the assumption of a constant spectrum across the object to fail. If this is the case then Equation 3-3 would produce an inaccurate PSF and the restored images would be distorted. Second, errors due to the sensor being saturated from the light reflecting off of metal parts on the circuit could cause increasing distortions with defocus. The other possibility is that the higher detail in the circuit image caused greater distortions in the restored images from zeros in the MTF.

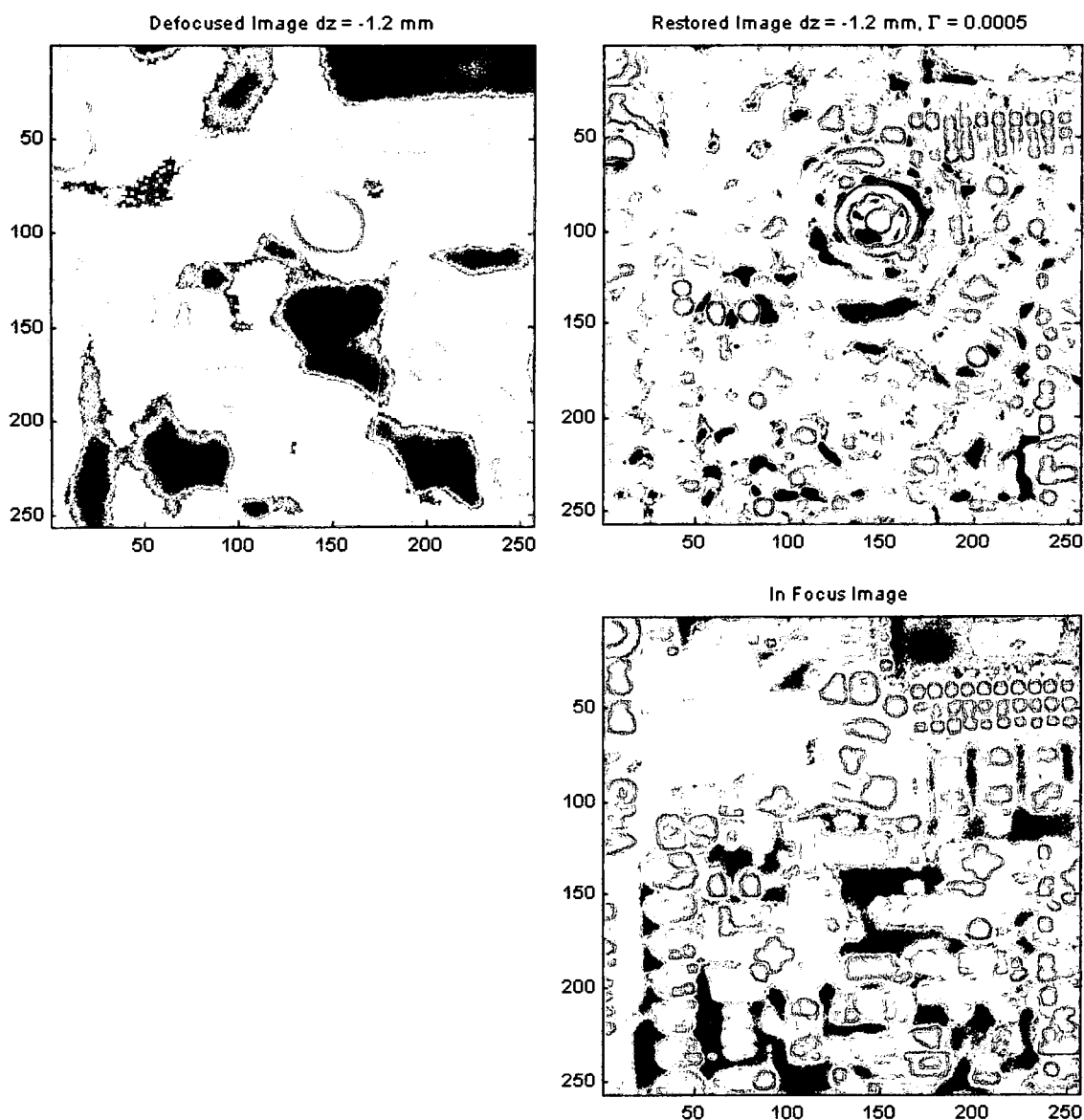


Figure 4-19: Circuit, $dz = -1200$ Microns

The defocus position for Figure 4-19 was $dz = -1200$ microns while the first zero in the MTF occurs at $dz = -226$ microns. The MTF associated with this position would have more zeros and at lower spatial frequencies than the modeled MTF shown in Figure 4-6. Therefore, it would be expected that the restored image would be highly distorted in comparison to the in-focus image and this is what is seen.

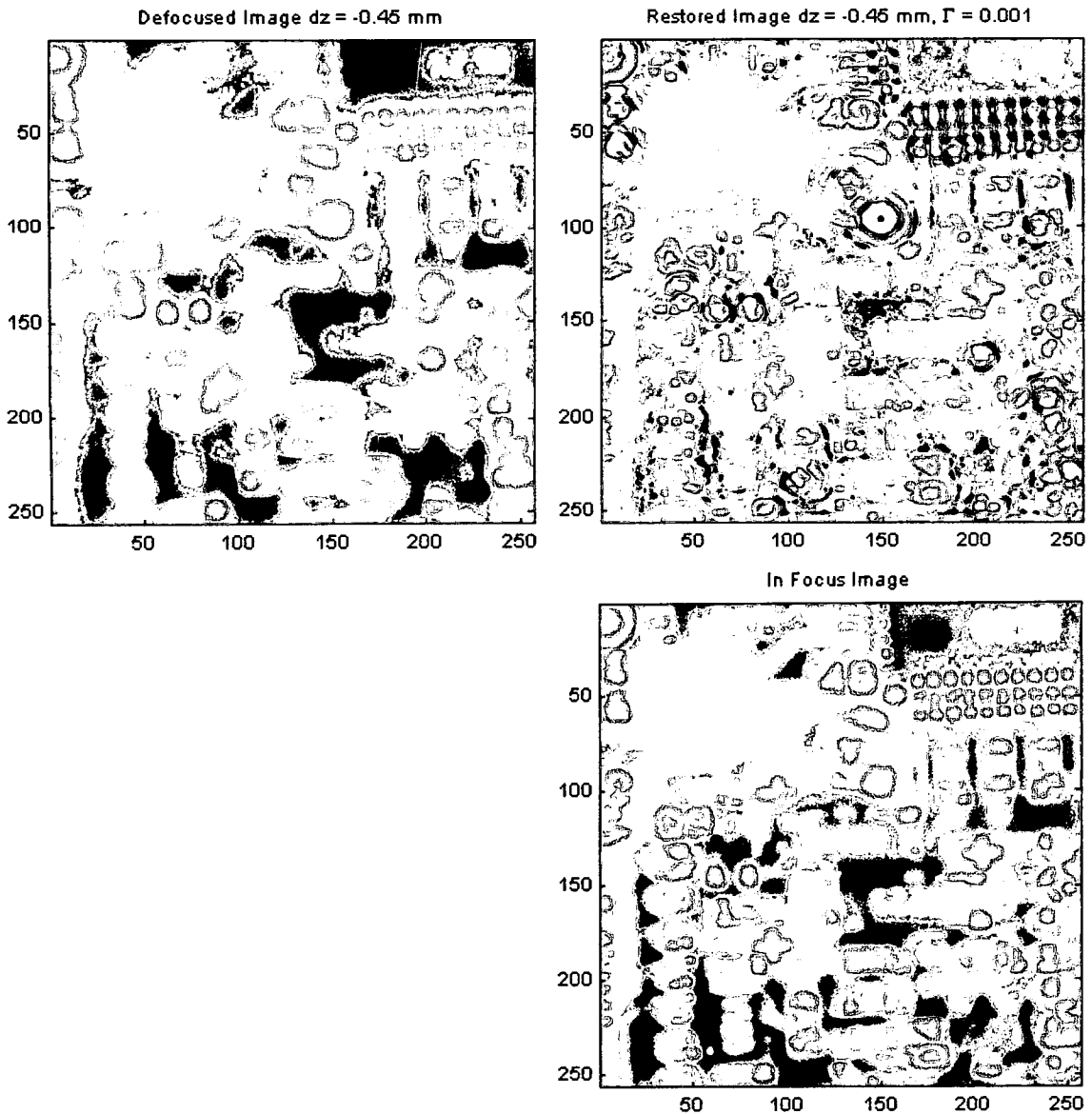


Figure 4-20: Circuit, $dz = -450$ Microns

The defocus position for Figure 4-20 was $dz = -450$ microns while the first zero in the MTF occurs at $dz = -226$ microns. The MTF associated with this position would be slightly more attenuated than the modeled MTF shown in Figure 4-6. The zeros in the MTF are at higher frequencies than those in the MTF for Figure 4-19 and it would be expected the ringing would be at shorter wavelengths and distortions to be less severe.

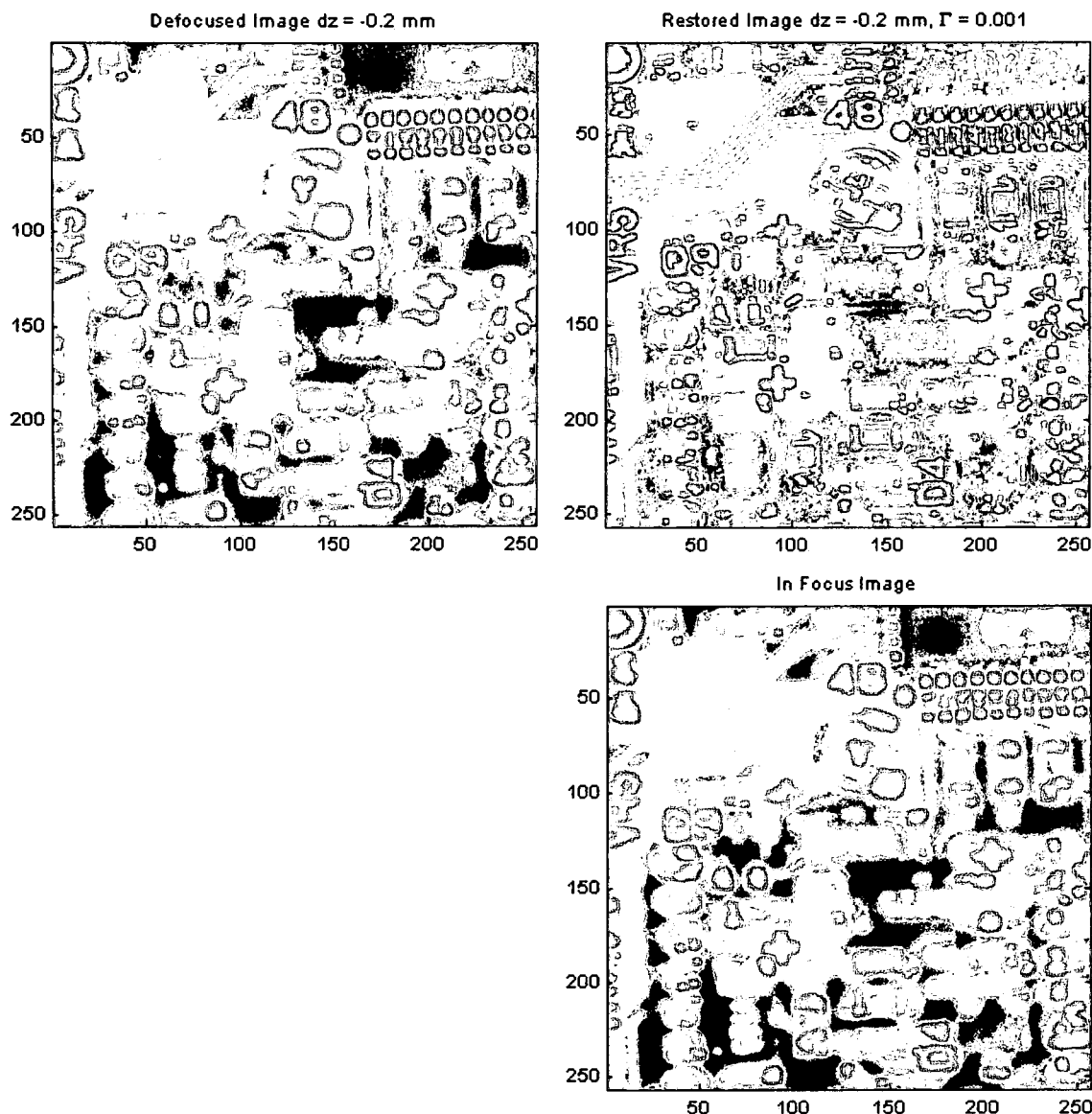


Figure 4-21: Circuit, $dz = -200$ Microns

The defocus position for Figure 4-21 was $dz = -200$ microns while the first zero in the MTF occurs at $dz = -226$ microns. The MTF associated with this position would be similar to the modeled MTF shown in Figure 4-8. There are no zeros in this MTF and from Figure 4-8, it is expected the restored image will be at least as good as the in-focus image.

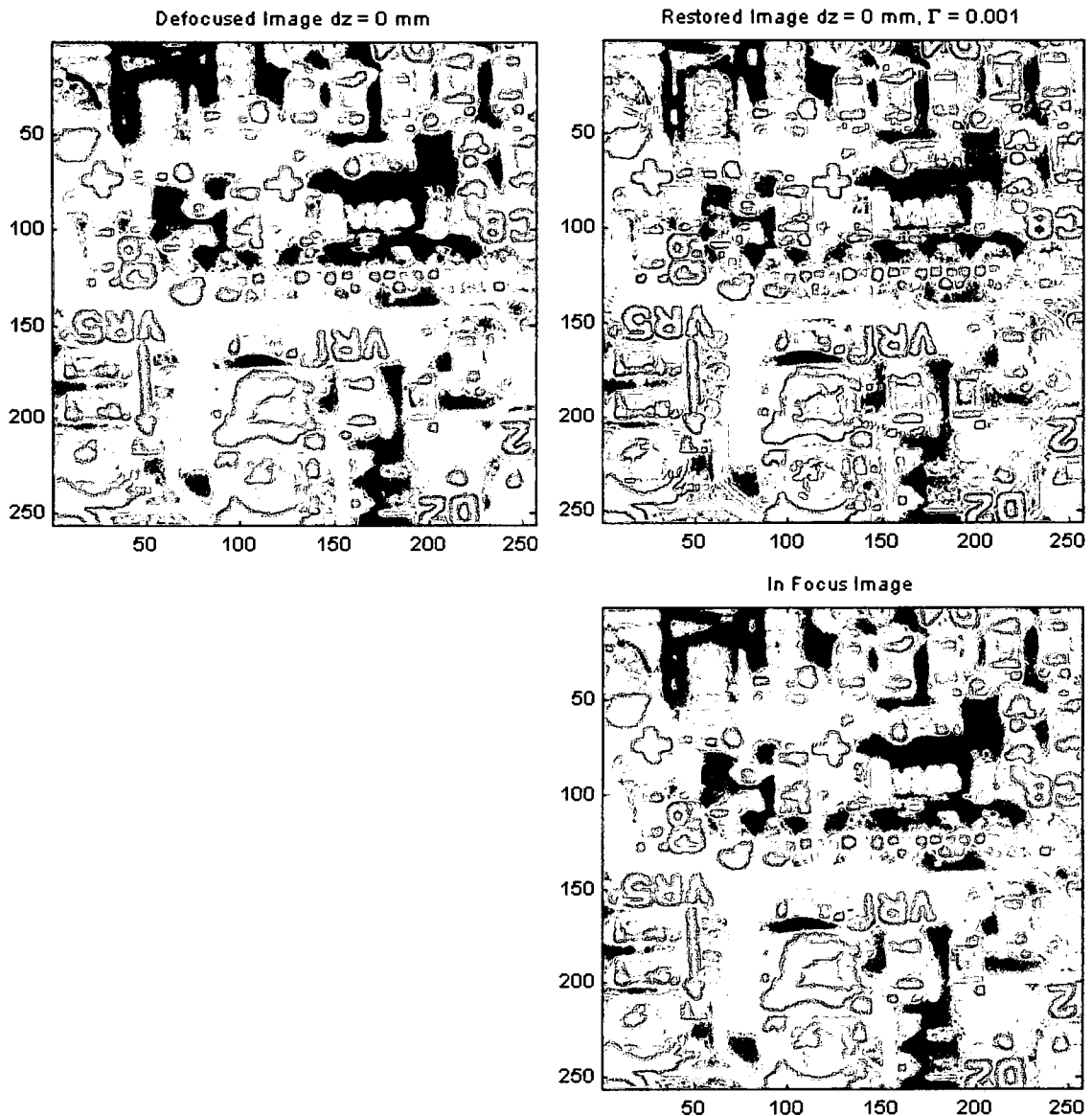


Figure 4-22: Circuit, Image Plane

The defocus position for Figure 4-22 was $dz = 0$ microns (focus) while the first zero in the MTF occurs at $dz = -226$ microns. The MTF for this position should be similar to the MTF modeled in Figure 4-9 and the restored image should therefore exhibit slightly higher contrasts for all spatial frequencies than the in-focus image. The restored image is effectively the diffraction corrected in-focus image.

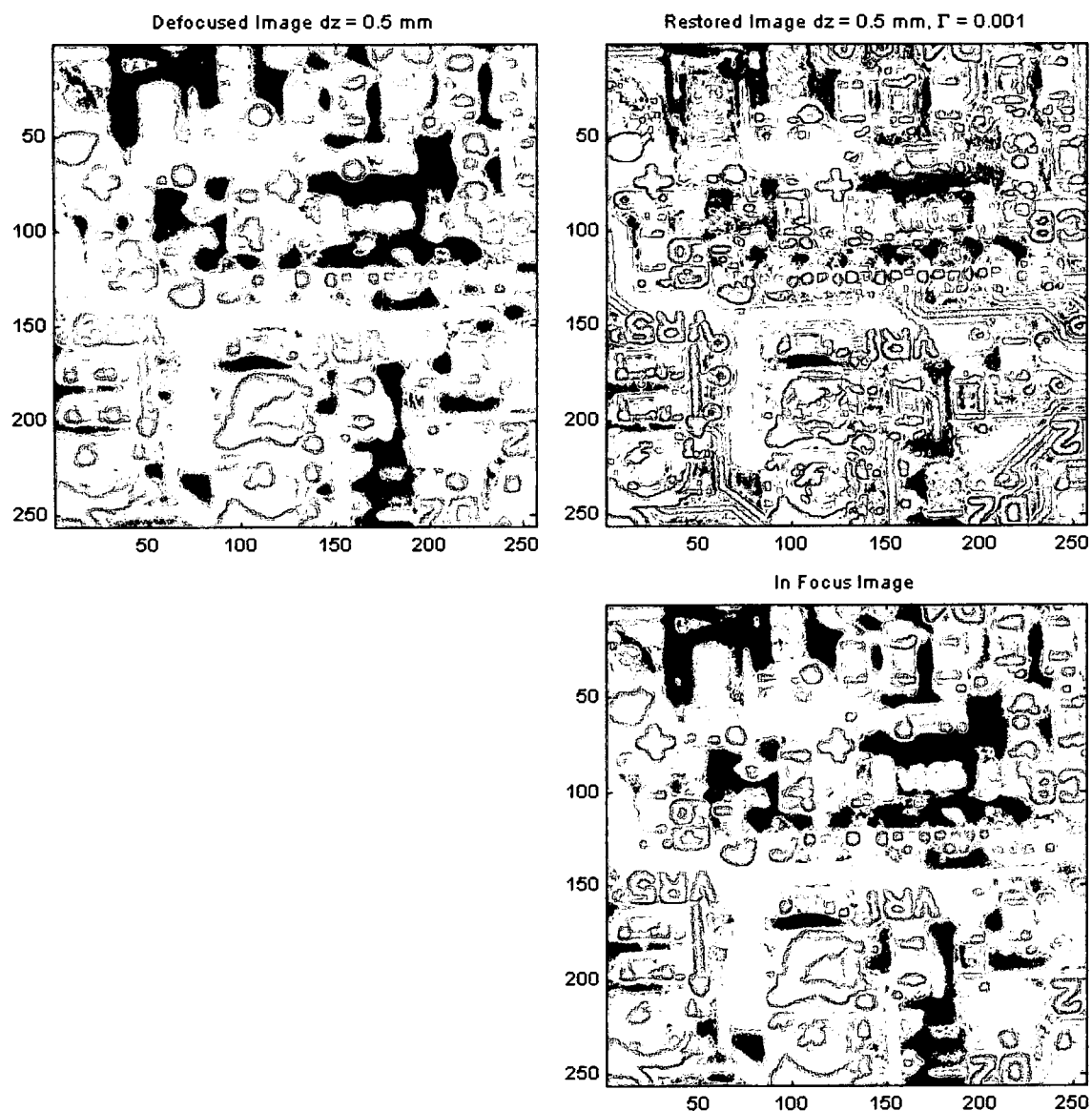


Figure 4-23: Circuit, $dz = 500$ Microns

The defocus position for Figure 4-23 was $dz = 500$ microns while the first zero in the MTF occurs at $dz = 2270$ microns. The MTF for this position should be similar to the MTF modeled in Figure 4-10 and it is expected the restored image should exhibit slightly higher contrasts for all spatial frequencies than the in-focus image.

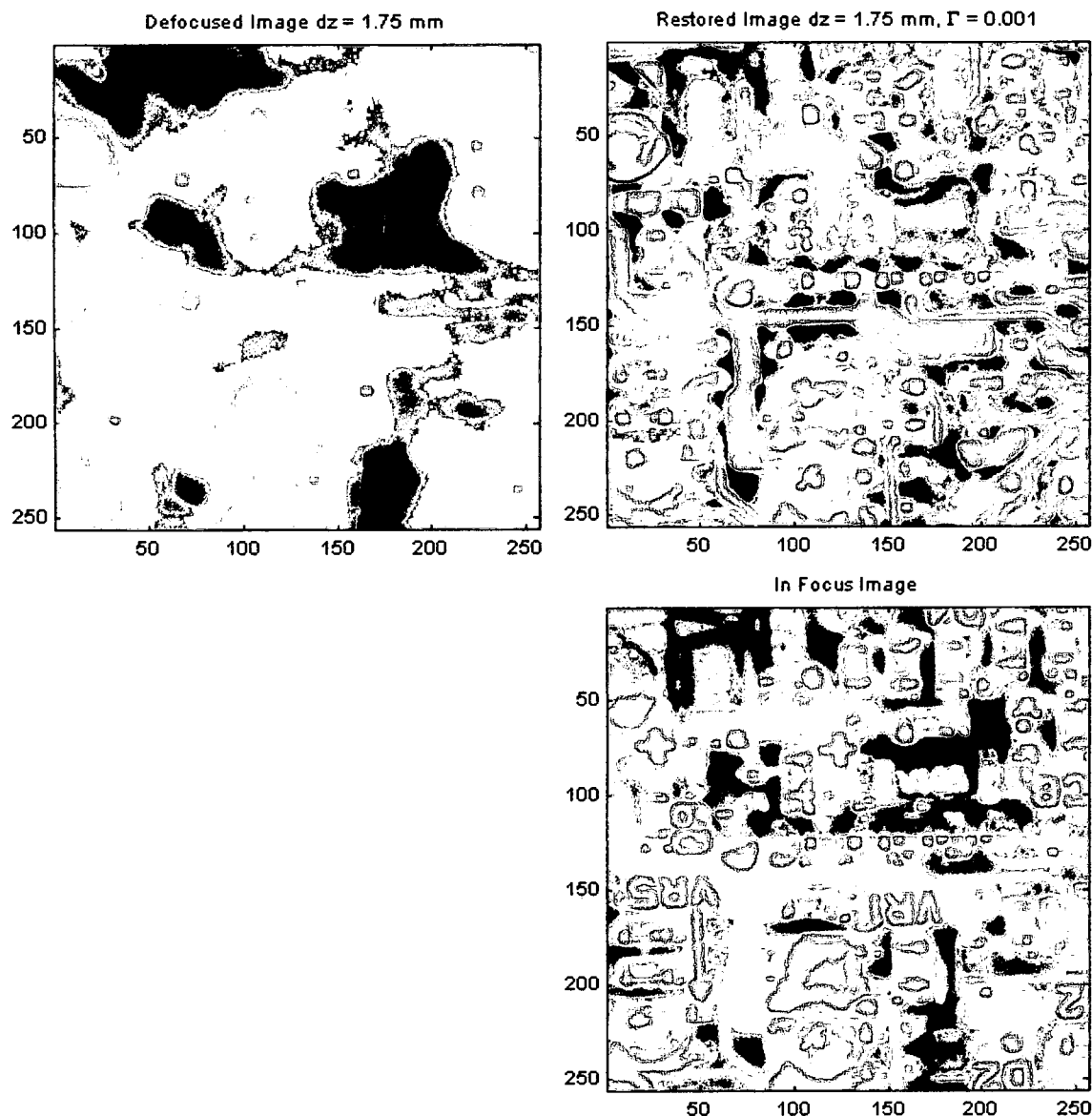


Figure 4-24: Circuit, $dz = 1750$ Microns

The defocus position for Figure 4-24 was $dz = +1750$ microns while the first zero in the MTF occurs at $dz = 2270$ microns. The MTF associated with this position would be between the modeled MTFs in Figures 4-10 and 4-11. There are no zeros in this MTF, however, the magnitude of the MTF for many spatial frequencies is low. Therefore, it is expected the restored image should approximate the in-focus image but with diminished contrast.

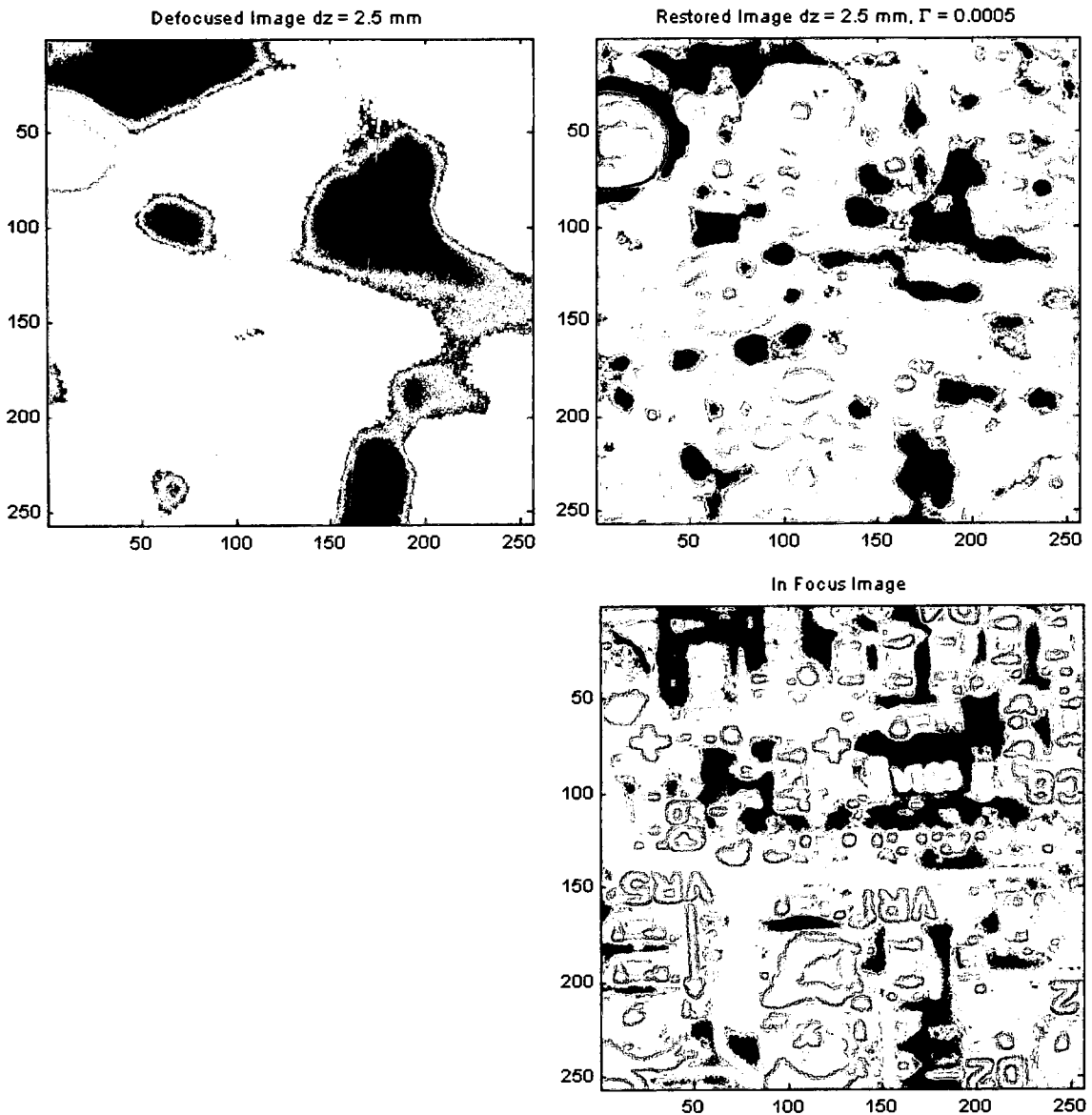


Figure 4-25: Circuit, $dz = 2500$ Microns

The defocus position for Figure 4-25 was $dz = +2500$ microns while the first zero in the MTF occurs at $dz = 2270$ microns. The MTF associated with this position would be similar to the modeled MTF in Figure 4-11. There is a zero in the MTF at this defocus position and from Figure 4-11 it appears at a low spatial frequency. Therefore, it is expected the restored image will be a highly distorted version of the in-focus image.

Defocused Image $dz = -0.46 \text{ mm}$



Figure 4-26: Sample Full-Size Blurred Circuit Image, $dz = -450 \text{ Microns}$ (Zero in MTF)

Restored Image $dz = -0.45 \text{ mm}$, $\Gamma = 0.001$

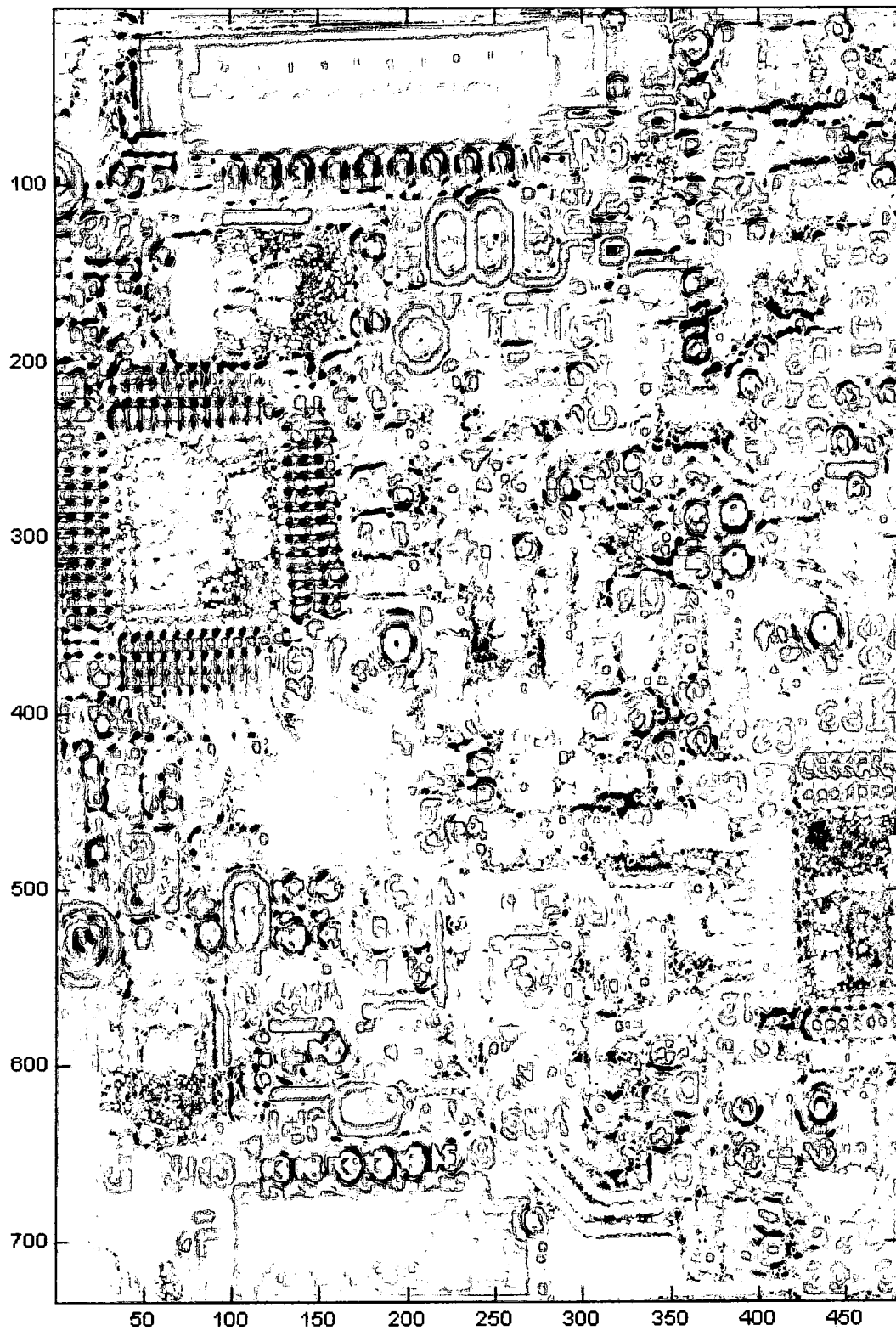


Figure 4-27: Sample Full-Size Restored Circuit Image, $dz = -450 \text{ Microns}$ (Zero in MTF)

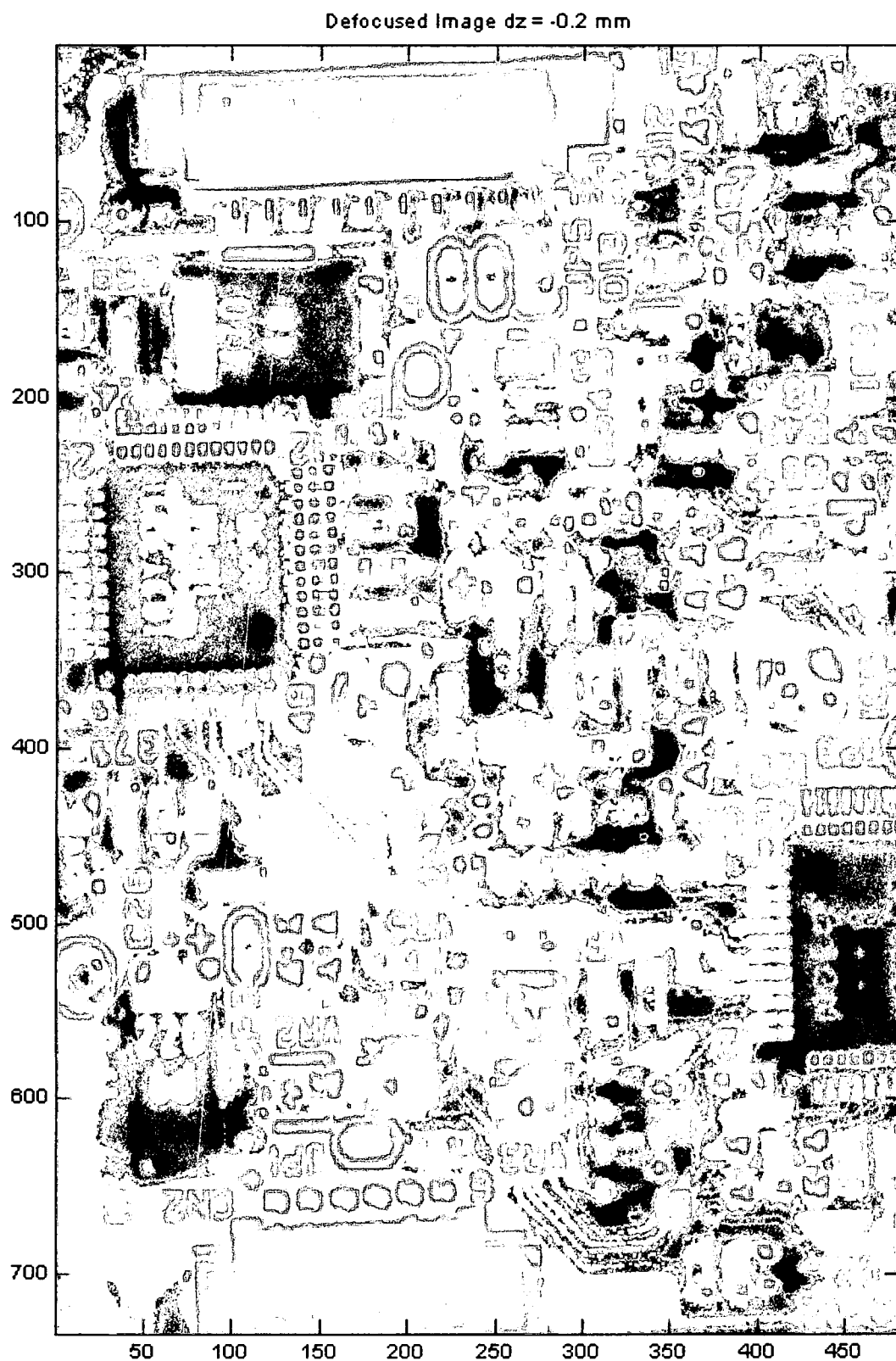


Figure 4-28: Sample Full-Size Defocused Circuit Image, $dz = -200$ Microns (No Zero in MTF)

Restored Image $dz = -0.2 \text{ mm}$, $\Gamma = 0.001$

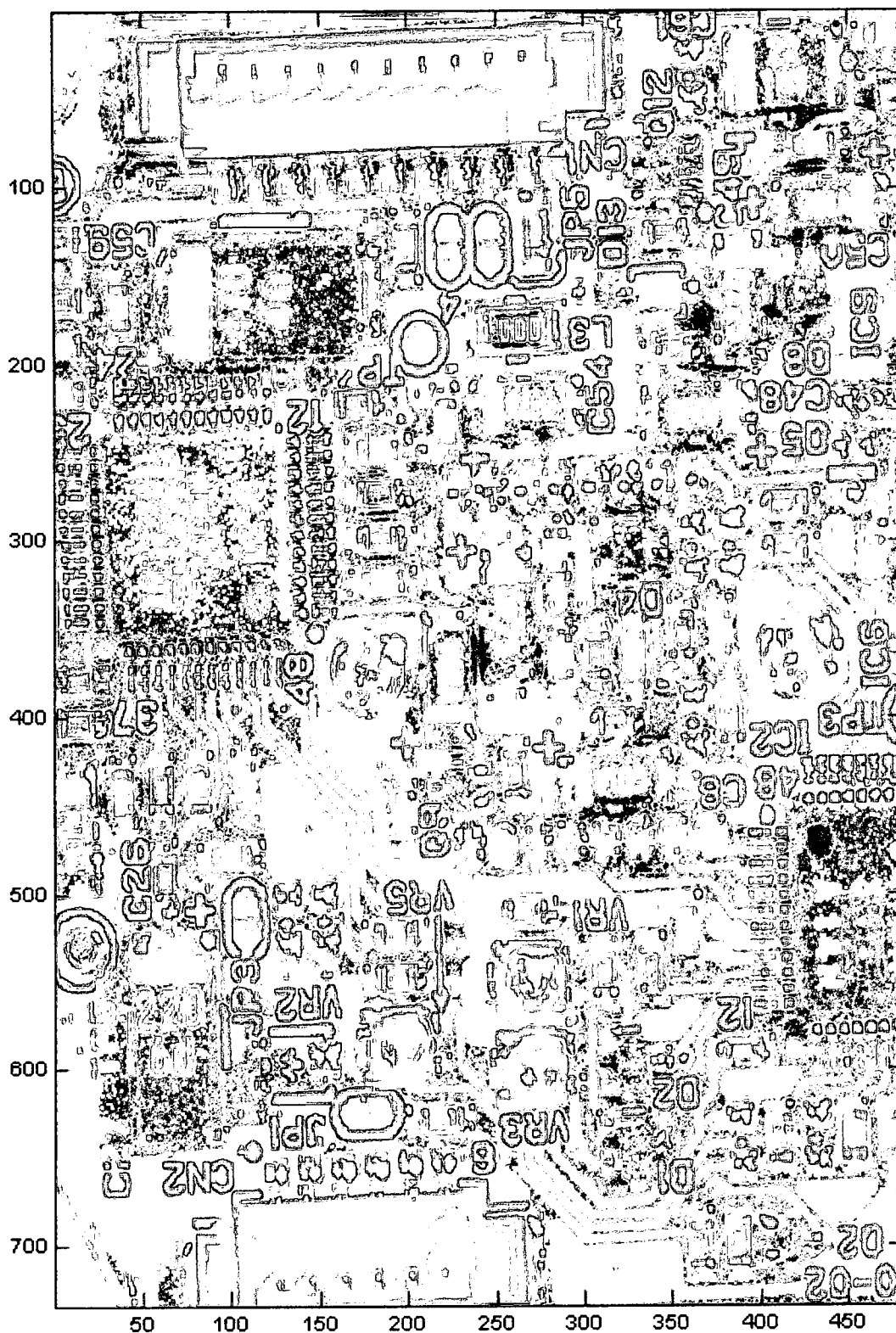


Figure 4-29: Sample Full-Size Restored Circuit Image, $dz = -200 \text{ Microns}$ (No Zero in MTF)

4.3 MWIR Imaging System Specification and Characterization

The MWIR imaging system was a prefabricated system consisting of many optical components and an InSb focal plane array (FPA) with 20-micron square pixels. The Zemax model diagram of the optics is in Figure 4-30. With the system in focus, the $f/\#$ was 5.9 with a distance from the exit pupil to image plane of 36.3 mm. The system was defocused by incrementally moving the focus lens group (see Figure 4-30) while the sensor was stationary.

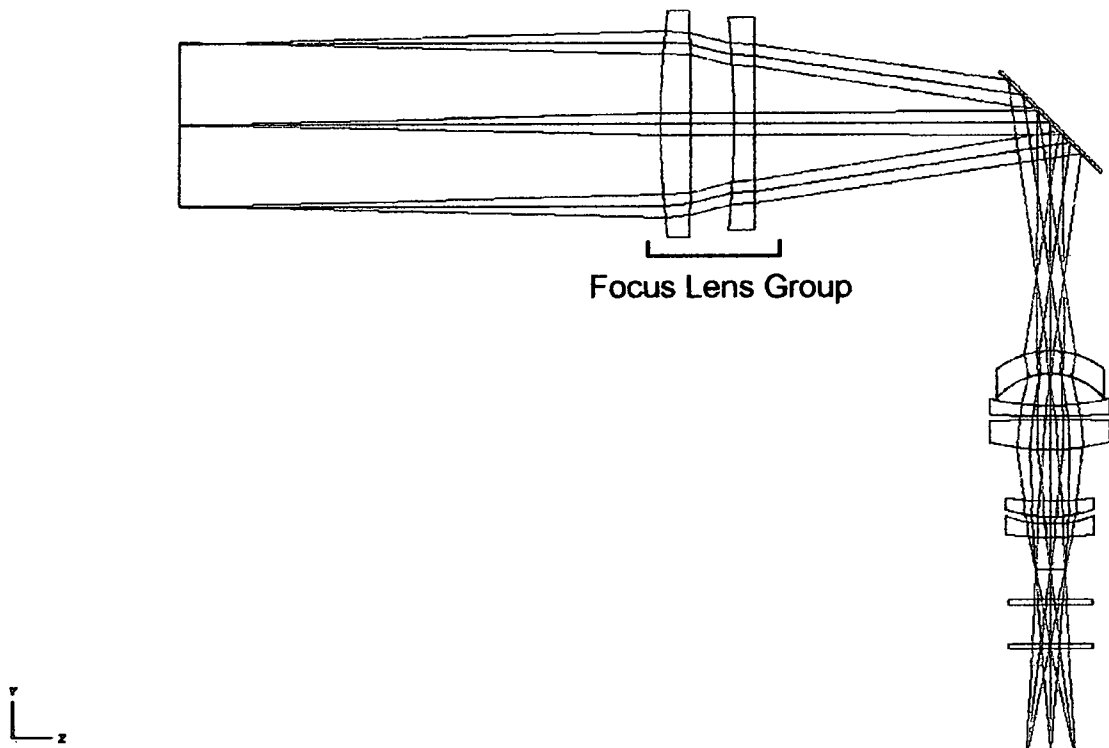


Figure 4-30: MWIR Zemax Model Diagram

The distances the lens group was moved were somewhat arbitrary and were measured with a micrometer. The effect of moving this lens group was to move the image plane

relative to the sensor which altered the distance to the image and therefore the $f/\#$ as well. In order to be able to process the defocused image data obtained from this system with the defocused image model presented in Chapters 2 and 3, it was necessary to determine the distance from the sensor to the image plane for each position of the lens group. This was done using the Zemax model of the system by altering the position of the focus lens group to the distances recorded that the lens group was moved. Zemax was then used to re-optimize the optical system which provided the necessary information.

The modeled focal shift curve is shown in Figure 4-31 and the spectral sensitivity of the sensor in Figure 4-32. Not that although the spectral sensitivity runs from .5 to 5.5 microns, it was assumed throughout that wavelengths not included in the range from 3 to 5 microns were filtered out by the optical system. The reason for this is that there were spectral filters in the optical train that passed light from 3 to 5 microns. The exact specifications of these filters were unavailable and therefore are a possible source of error.

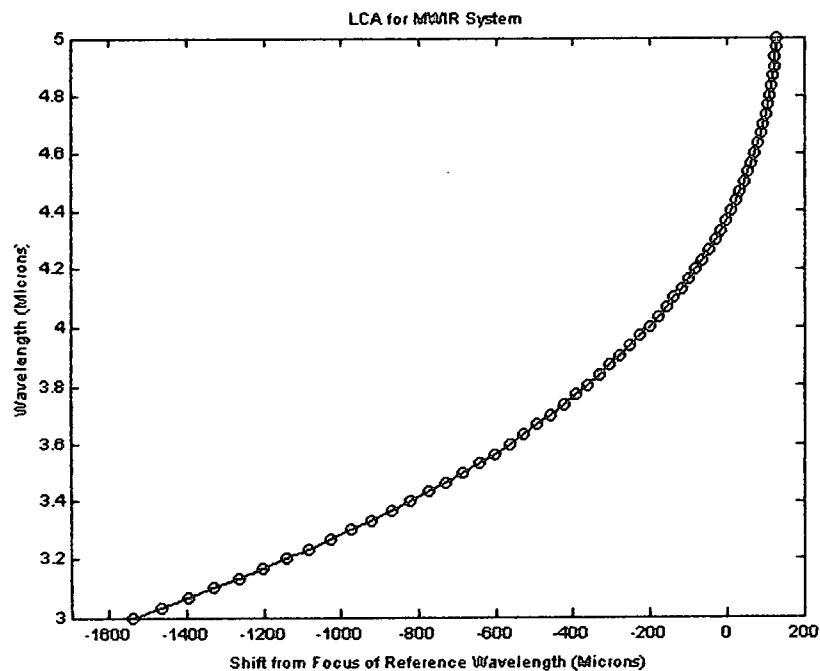


Figure 4-31: MWIR System Modeled Focal Shift Curve

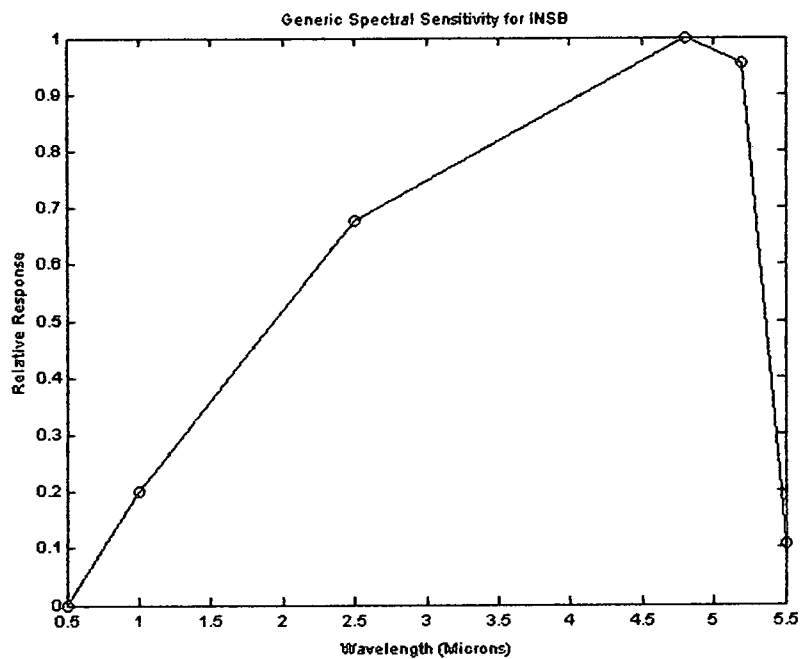


Figure 4-32: Generic InSb Spectral Sensitivity

The location of the image plane relative to the focal shift curve, the location of the defocus positions at which zeros appeared in the MTF, and a plot of the error metric defined in Equation 3-6 are in Figure 4-33 (Note that the first zeros in the MTF on either side of the image plane are asymmetric and the error metric curve varies with Γ . See Section 4-1 for a general discussion.).

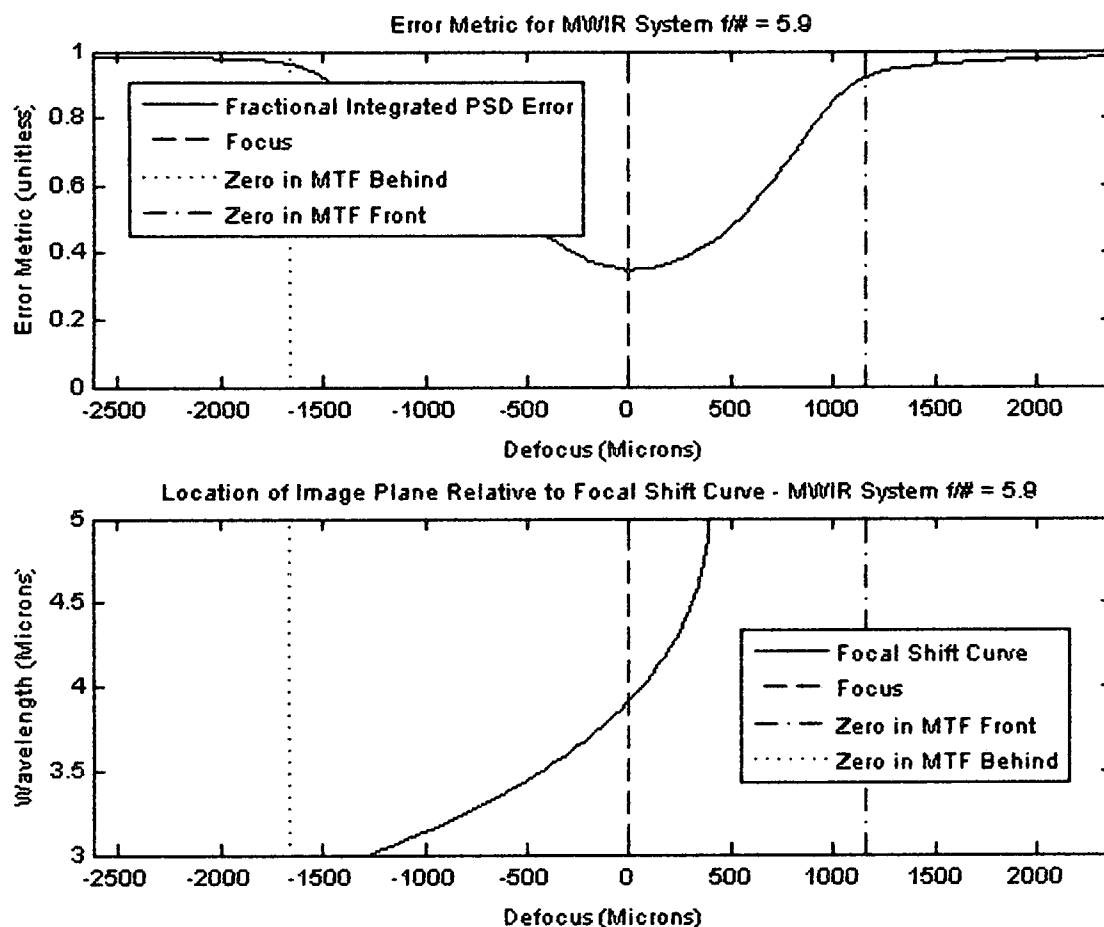


Figure 4-33: MWIR System Model Analysis

The values of the important distances are in Table 4-2. Figure 4-33 was generated from 10,000 computations of the Fresnel Defocus Diffraction Integral (Equation 2-1) using the algorithm presented in Section 2-2 along with the subsequent computation of the defocused image PSF (Equation 3-3) with defocus distances from the image plane

ranging from about -2500 microns to +2500 microns (The range was selected so as to contain both of the positions at which zeros in the defocus MTF appear) and an increment of about 50.5 microns. The values of relevant parameters used in generating Figure 4-33 were $\tau = .05$, $\varepsilon = .05$, and $\Gamma = .01$ where ε and τ are defined in Section 2-2. The number of radial points sampled per computed PSF was 100 (before down-sampling to the pixel frequency of the sensor). This was chosen so that the cutoff of the optics was below the Nyquist frequency.

Table 4-2: Important MWIR System Distances

Location of 1 st Zero in MTF in Front of Image Plane	Location of Image Plane Relative to Reference Wavelength Focus (4.8 Microns)	Location of 1 st Zero in MTF in Front of Image Plane
-1667 +/- 50.5 Microns	-373.7 +/- 50.5 Microns	1162 +/- 50.5 Microns

Figure 4-34 shows horizontal cross-sections of the computed imaging PSFs for select defocus positions and Figures 4-35 through 4-40 shows horizontal cross-sections of the associated MTFs. The MTF plots show the optical MTFs, the system MTFs (optical MTFs after downsampling), and the effective MTFs upon Wiener deconvolution. From Figures 4-35 through 4-40, it can be seen that other than for planes close to the image plane the optical MTF obtains only small values above the Nyquist frequency and it is therefore expected aliasing will not be a major factor in the restoration (See Section 3-3 for discussion). Figures 4-35 and 4-39 show the MTFs for the defocus positions for which new zeros first appear in front and behind the image plane.

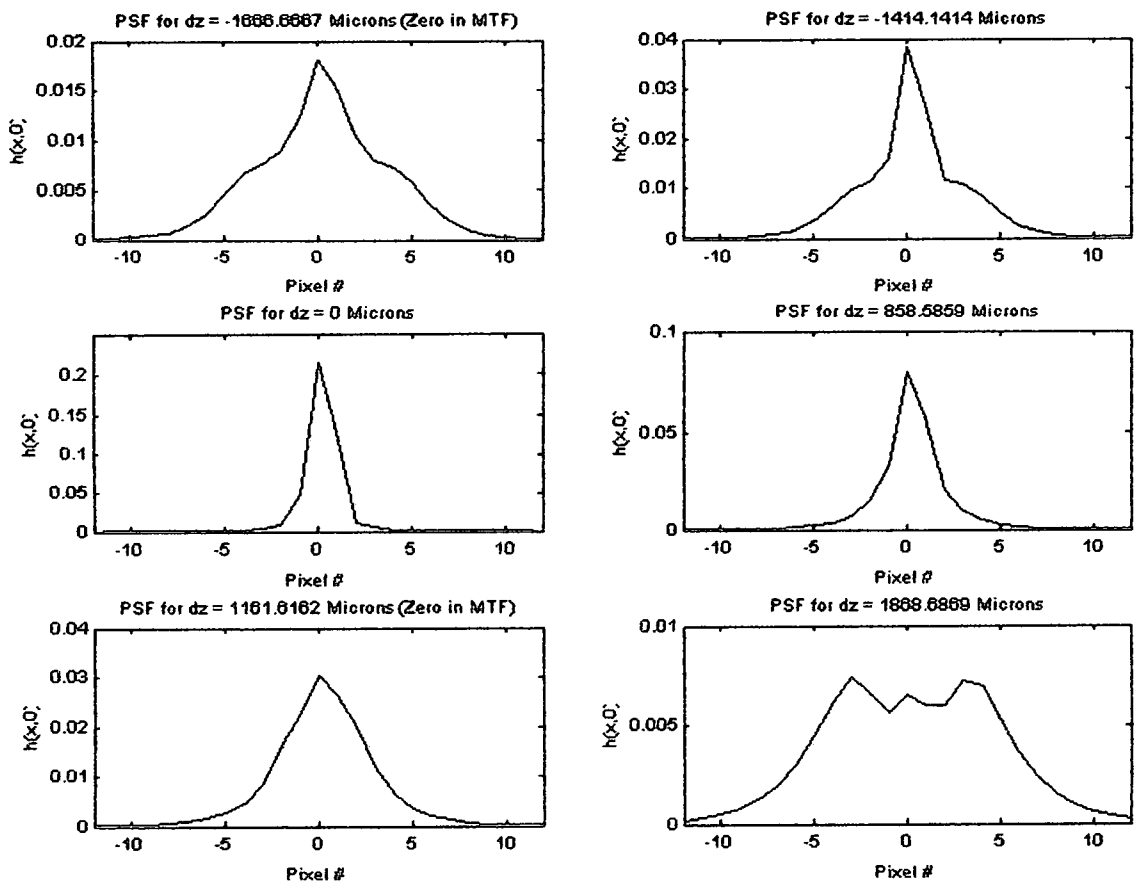


Figure 4-34: Horizontal Cross Sections of Modeled Imaging Defocus PSFs

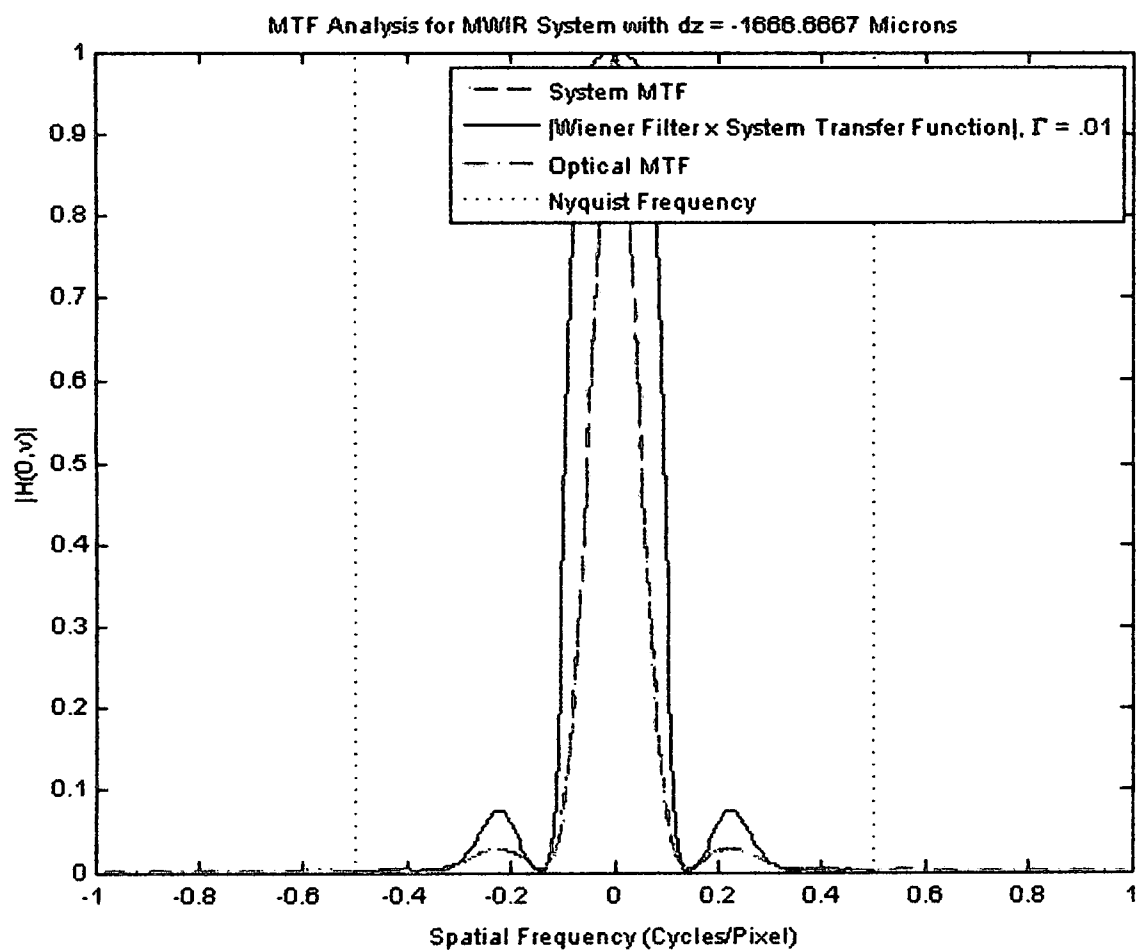


Figure 4-35: Modeled Defocus MTF for MWIR System with $dz = -1667$ Microns (1st Zero in MTF)

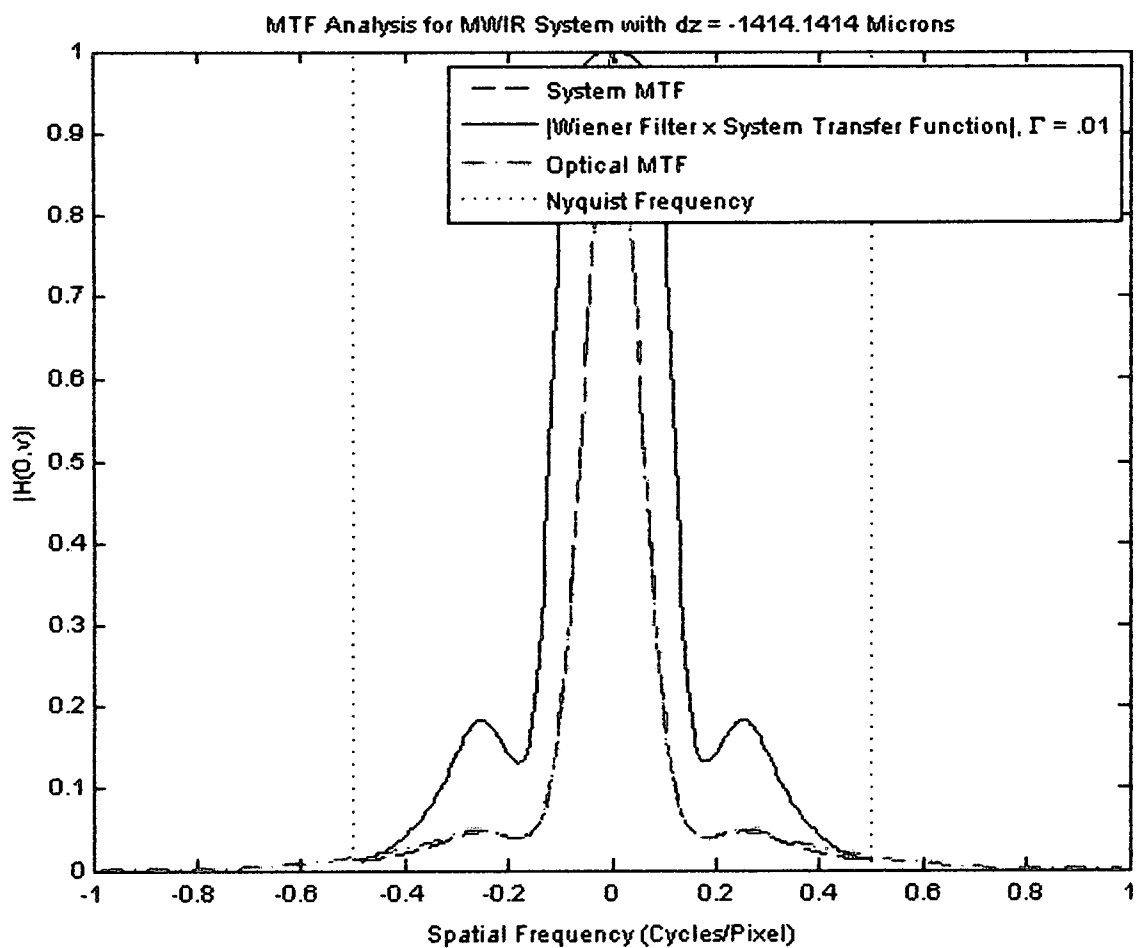


Figure 4-36: Modeled Defocus MTF for MWIR System with $dz = -1414$ Microns

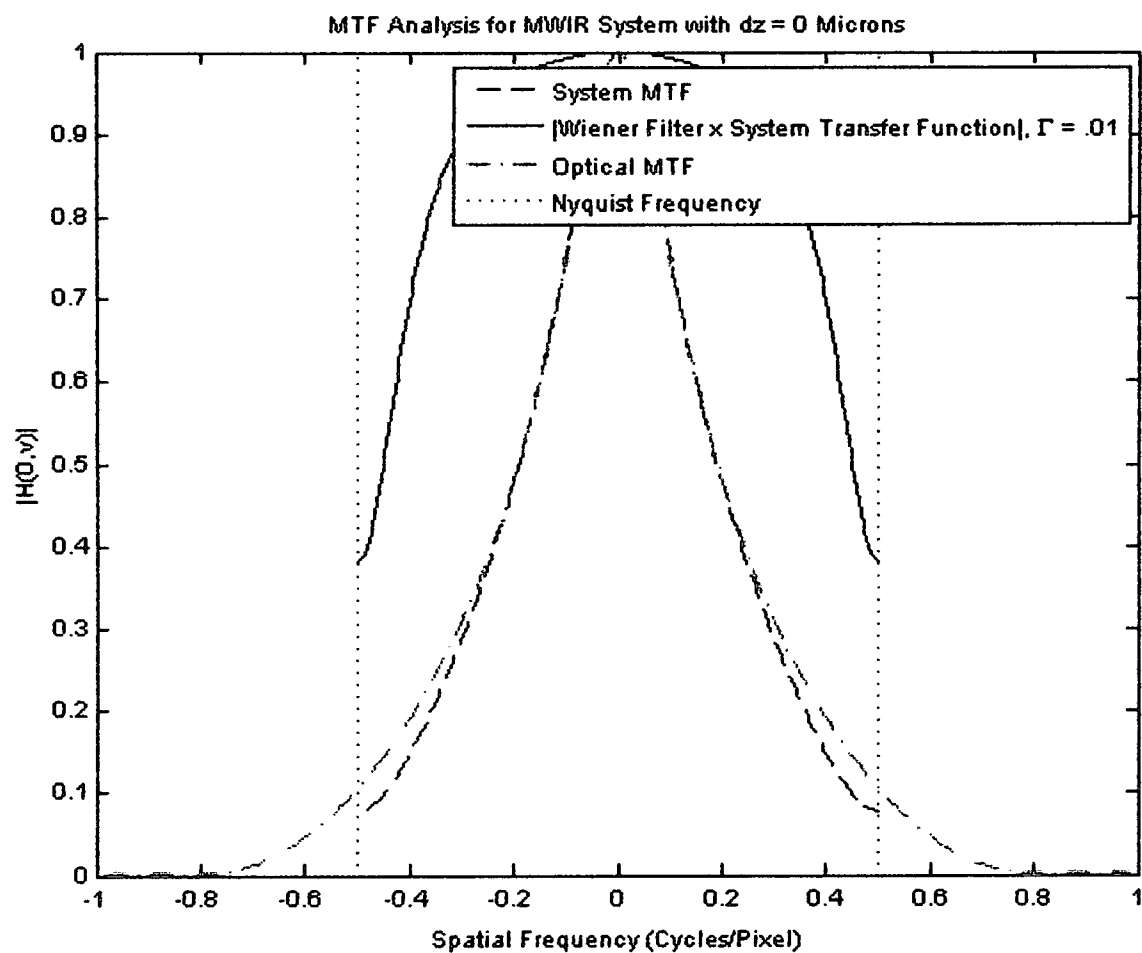


Figure 4-37: Modeled Defocus MTF for MWIR System, Image Plane

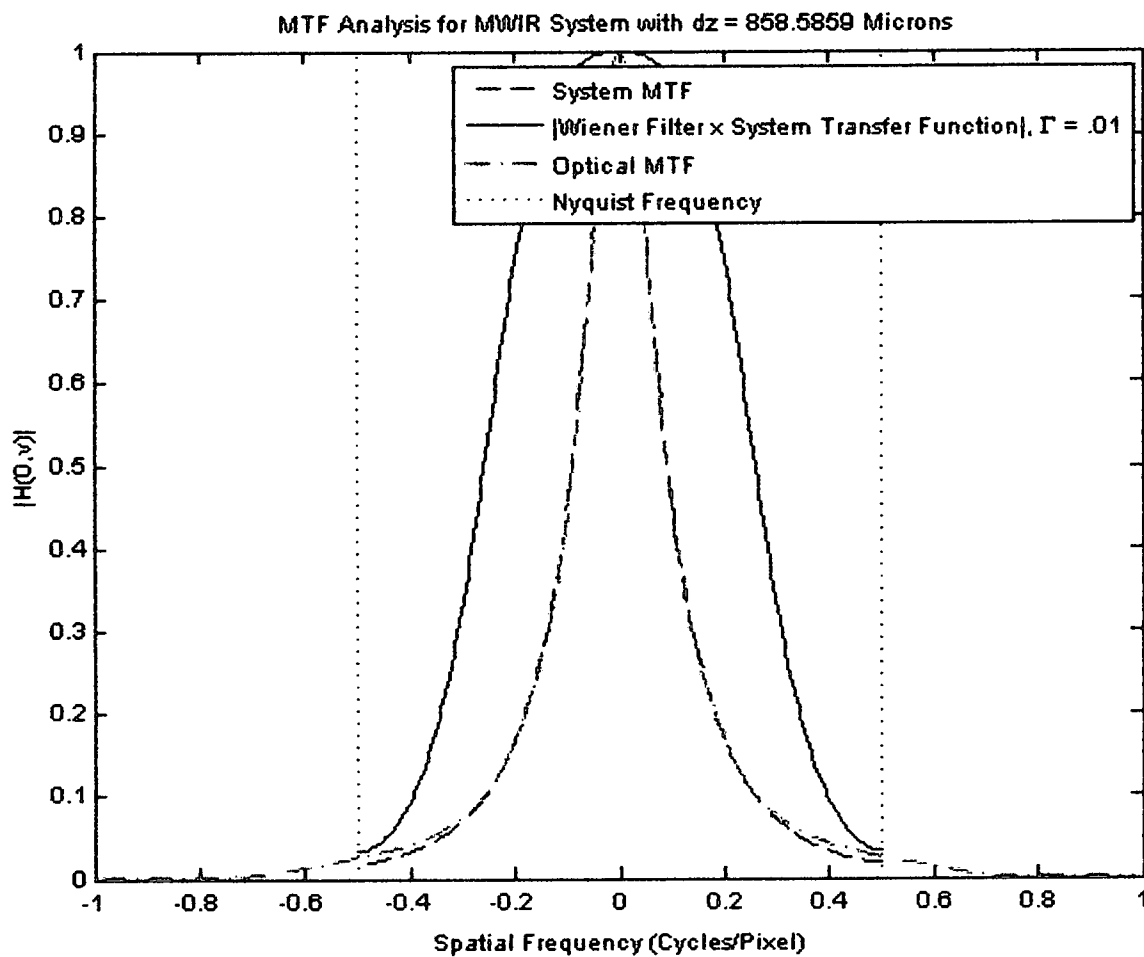


Figure 4-38: Modeled Defocus MTF for MWIR System with $dz = 859$ Microns

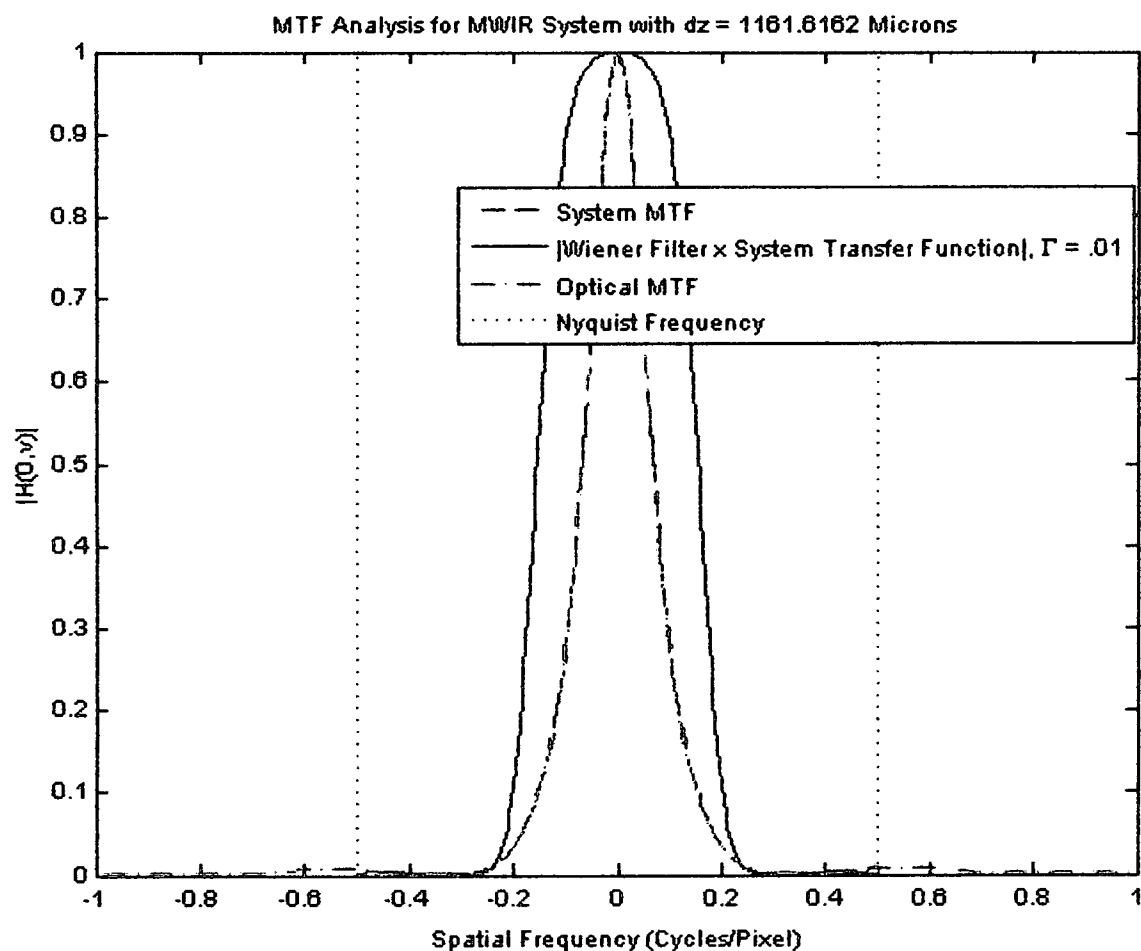


Figure 4-39: Modeled Defocus MTF for MWIR System with $dz = 1162$ Microns (1st Zero in MTF)

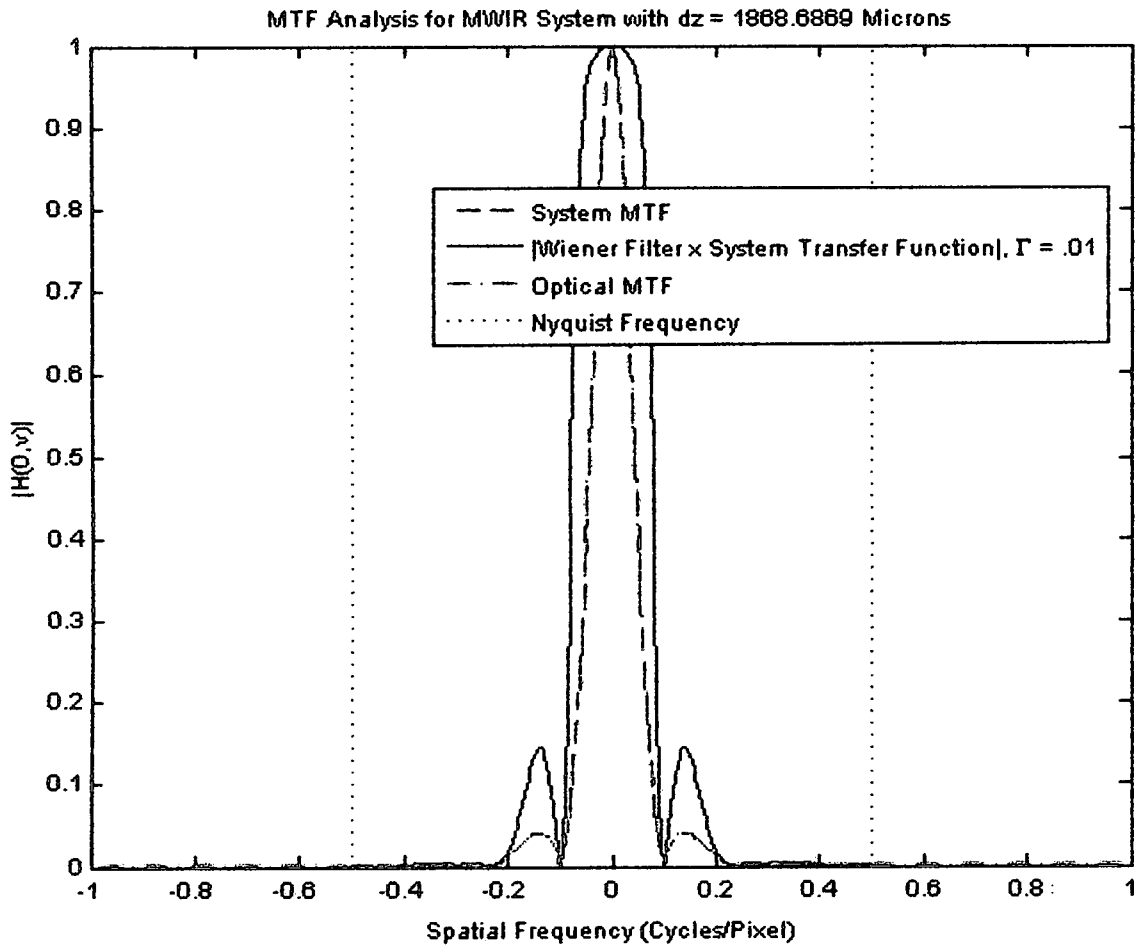


Figure 4-40: Modeled Defocus MTF for MWIR System with $dz = 1869$ Microns

4.4 Results of Restoring Imagery from the MWIR System

For the MWIR system there is only one set of defocused imagery (of a house) that is both noisier and exhibits scintillation effects. Figures 4-41 through 4-48 show 256x256 square pixel sections of the defocused imagery, the restored imagery, and the in-focus image for reference. These figures step through increasing z -distances starting before focus and ending after focus. Figures 4-49 through 4-52 show full-page images for select blurred and restored images. The defocused imagery was restored using Wiener deconvolution filters following the procedure outlined in Section 3.3. The matlab

file used to implement the Wiener filter is in Appendix C. The PSFs used in the restorations were generated in an identical fashion as those in Figure 4-34 and with the same input parameters except for the defocus distances.

As with the restored images from the visible system, restored images for defocus distances within the range defined by setting the locations of the first zeros in the defocused image MTF as upper bounds (See Table 4-2) exhibit severe image distortions relative to the in-focus image. Restored images within these bounds are less distorted, although the quality does decrease with increasing defocus as expected from the MTFs in Figures 4-35 through 4-40 and from the error metric plotted in Figure 4-33. See Section 4-2 for a more general discussion of restoration distortions.

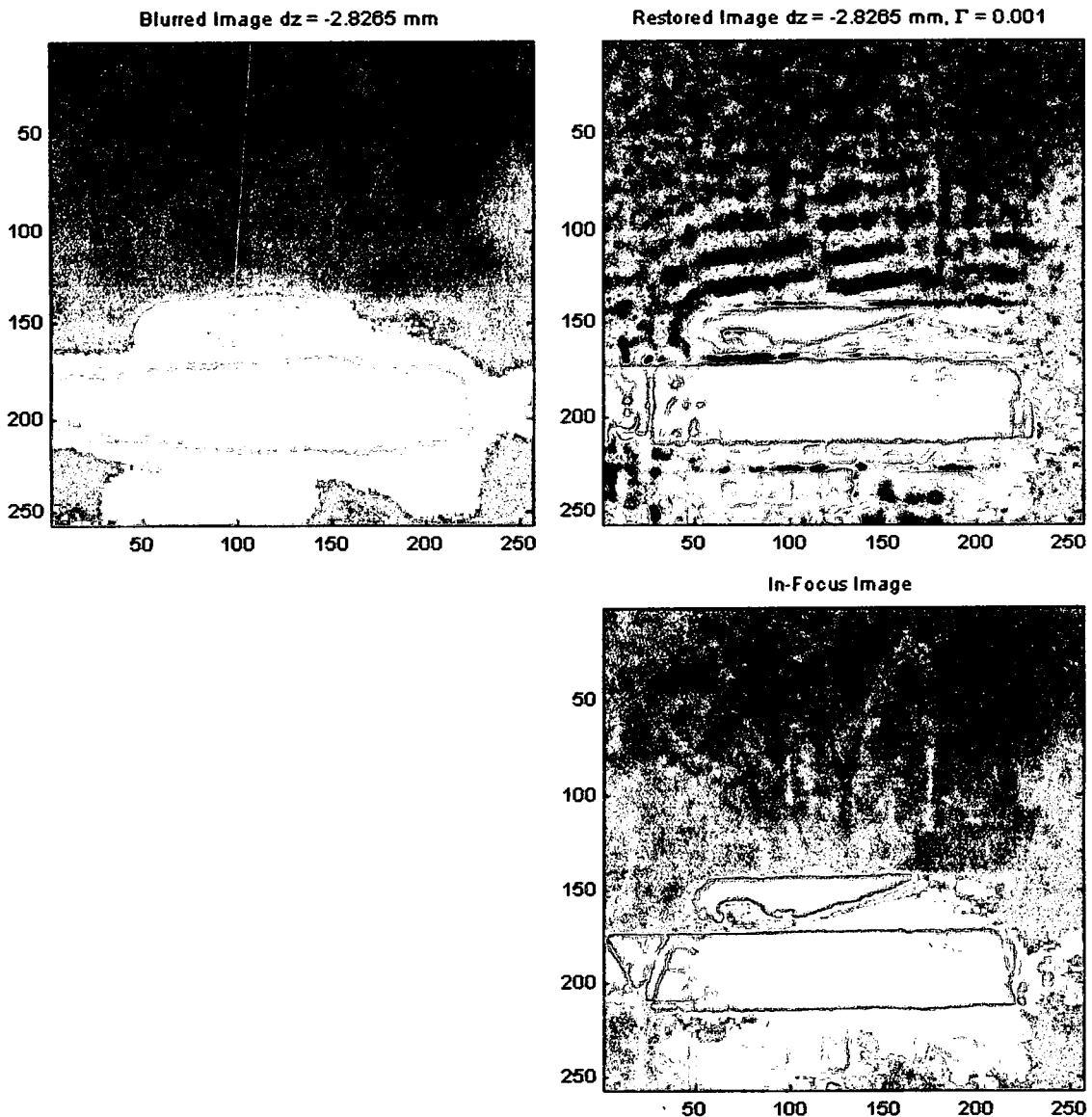


Figure 4-41: MWIR Imagery, $dz = -2827$ Microns

The defocus position for Figure 4-41 was $dz = -2827$ microns while the first zero in the MTF occurs at $dz = -1667$ microns. The MTF associated with this position would have more zeros and at lower spatial frequencies than the modeled MTF shown in Figure 4-35. Therefore, it would be expected that the restored image would be highly distorted in comparison to the in-focus image and this is what is seen.

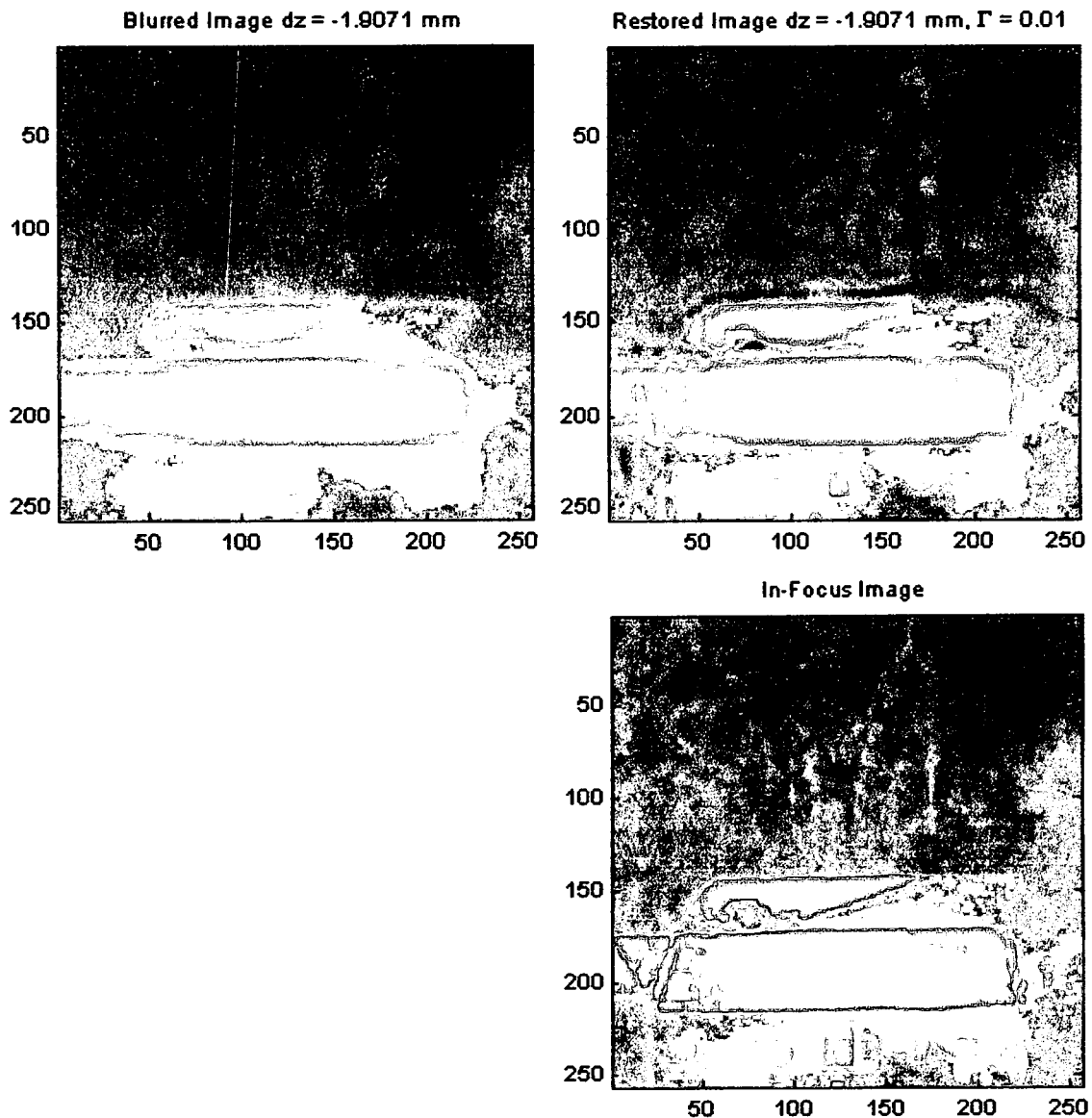


Figure 4-42: MWIR Imagery, $dz = -1907$ Microns

The defocus position for Figure 4-42 was $dz = -1907$ microns while the first zero in the MTF occurs at $dz = -1667$ microns. The MTF associated with this position would have more zeros and at lower spatial frequencies than the modeled MTF shown in Figure 4-35. Therefore, it would be expected that the restored image would be highly distorted in comparison to the in-focus image, but perhaps less so than Figure 4-41.

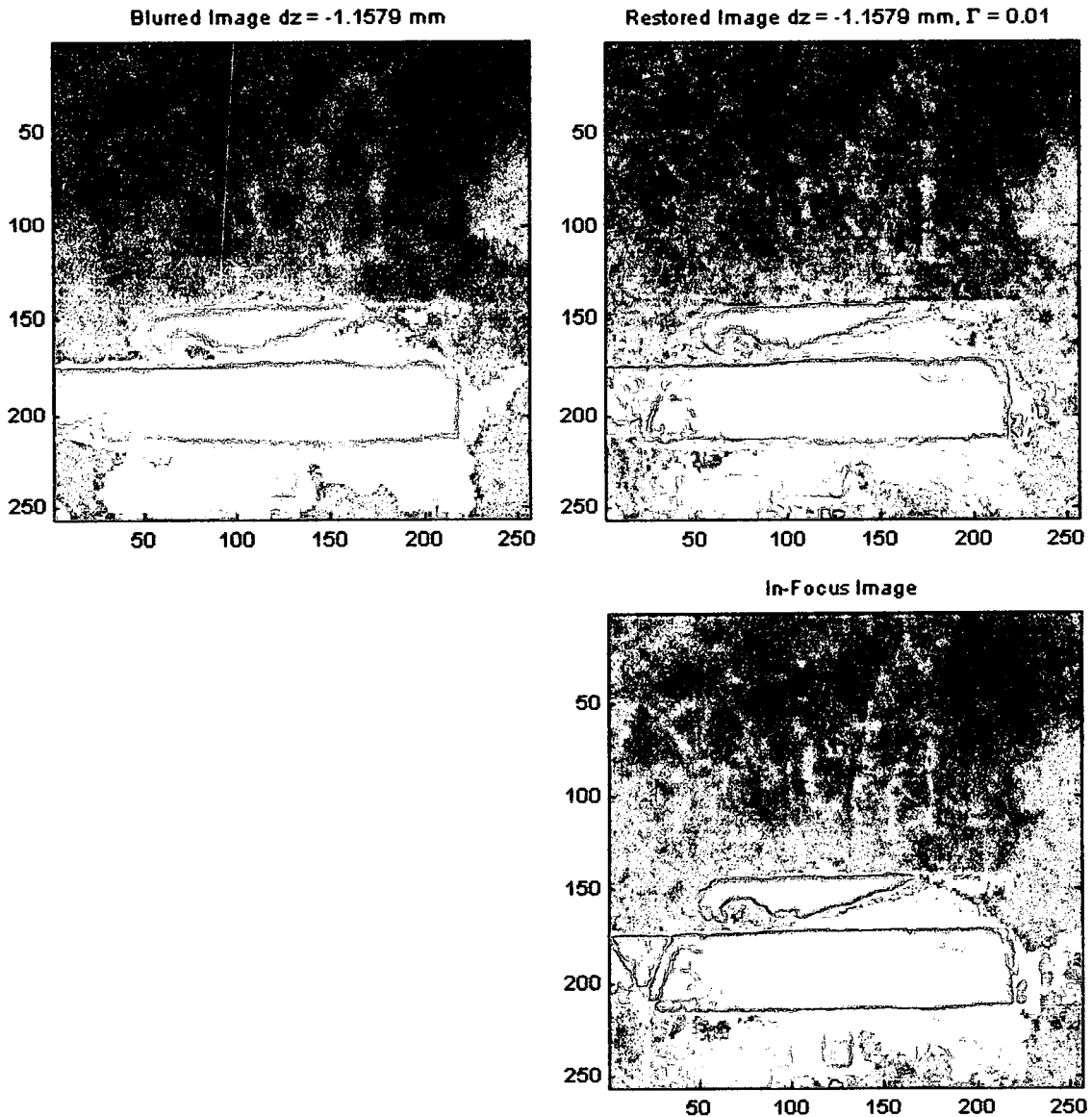


Figure 4-43: MWIR Imagery, $dz = -1158$ Microns

The defocus position for Figure 4-43 was $dz = -1158$ microns while the first zero in the MTF occurs at $dz = -1667$ microns. The MTF associated with this position would be similar to the modeled MTF in Figure 4-36. There are no zeros in the MTF and it is expected the restored image will approximate the in-focus image (Figure 4-36 shows an effective MTF upon restoration similar to the in-focus, un-restored MTF in Figure 4-37).

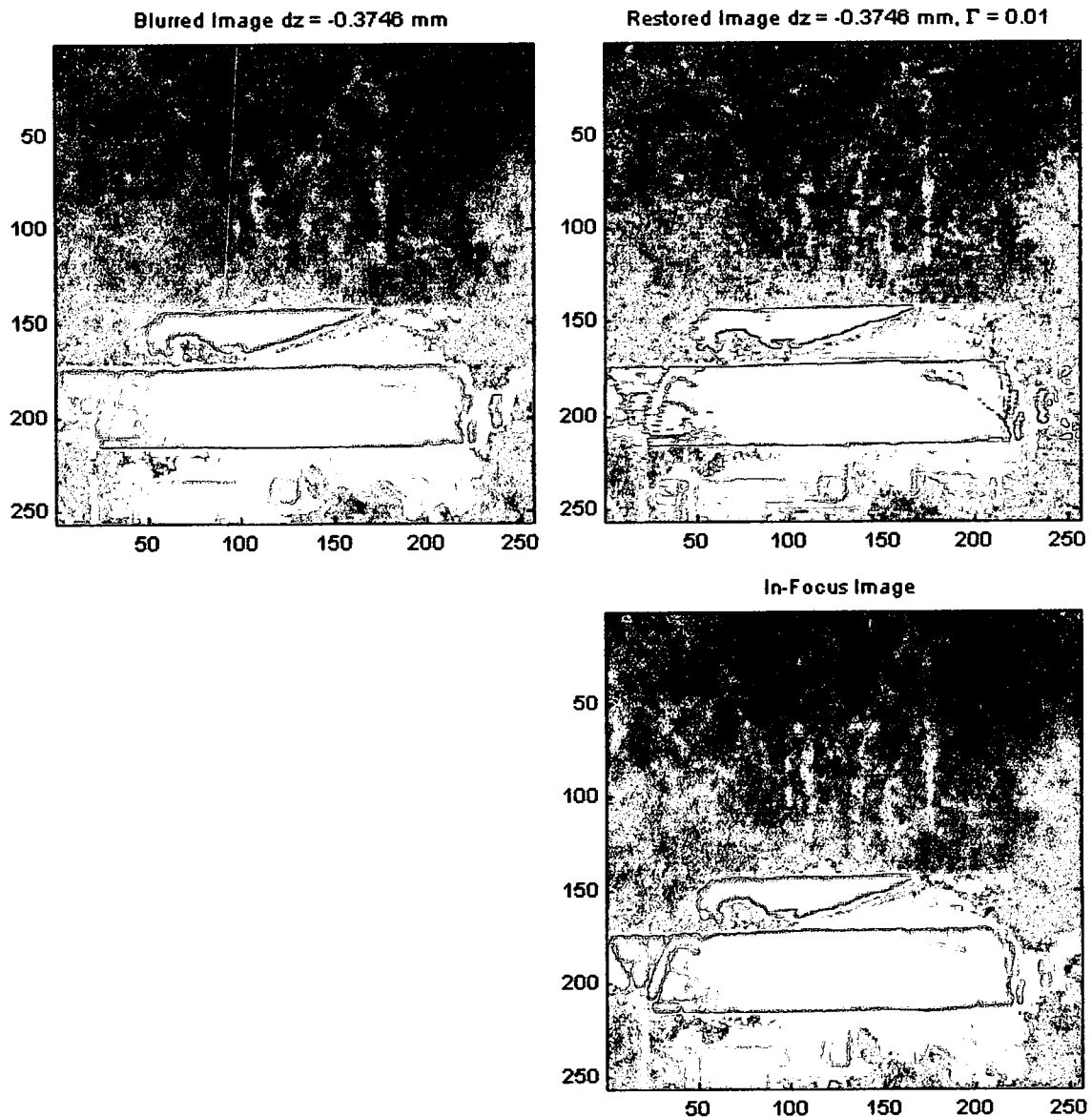


Figure 4-44: MWIR Imagery, $dz = -375$ Microns

The defocus position for Figure 4-44 was $dz = -375$ microns while the first zero in the MTF occurs at $dz = -1667$ microns. The MTF associated with this position would be similar to the modeled MTF in Figure 4-37. There are no zeros in the MTF and from Figure 4-37, it is expected the restored image will exhibit greater a greater contrast than even the in-focus image for all wavelengths.

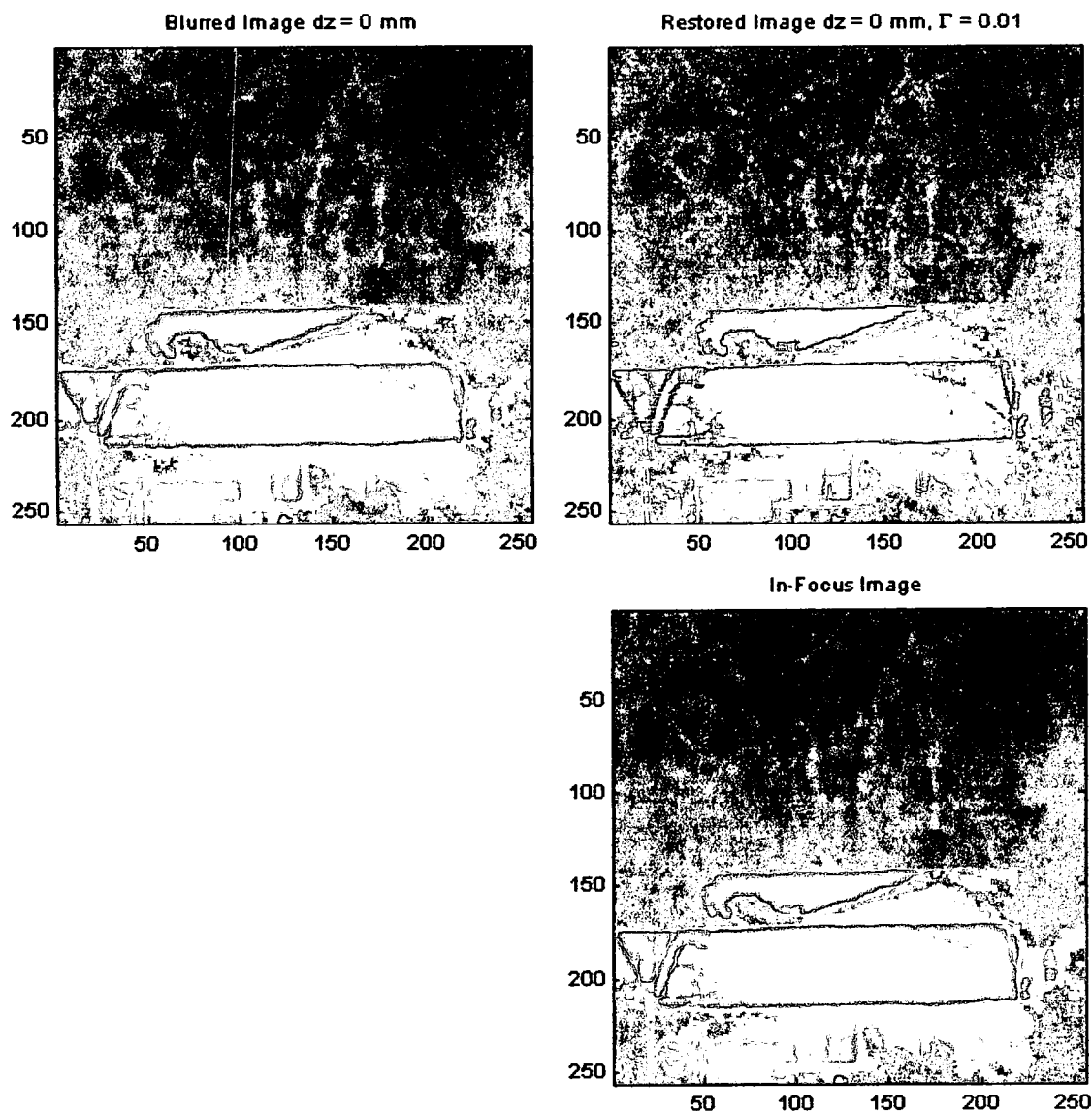


Figure 4-45: MWIR Imagery, Image Plane

The defocus position for Figure 4-45 was $dz = 0$ microns while the first zero in the MTF occurs at $dz = -1667$ microns. The MTF associated with this position would be similar to the modeled MTF in Figure 4-37. From Figure 4-37 it is expected the restored image will produce an image of even a higher quality than the in-focus image. The restored image is effectively the diffraction corrected in-focus image.

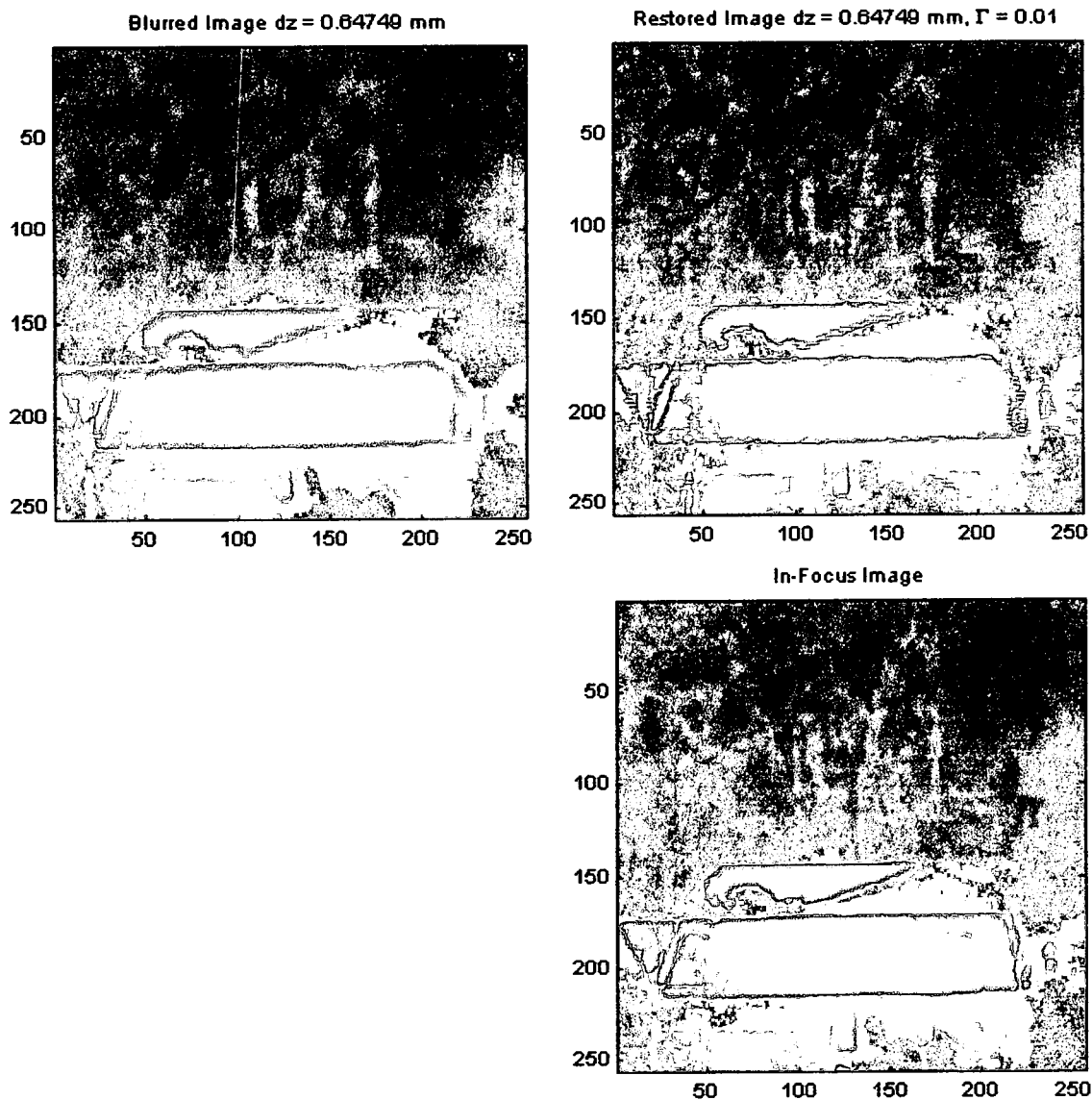


Figure 4-46: MWIR Imagery, $dz = 647$ Microns

The defocus position for Figure 4-46 was $dz = 647$ microns while the first zero in the MTF occurs at $dz = 1162$ microns. The MTF associated with this position would be similar to the modeled MTF in Figure 4-38. There are no zeros in the MTF and it is expected the restored image will approximate the in-focus image (Figure 4-38 shows an effective MTF upon restoration similar to the in-focus, un-restored MTF in Figure 4-37).

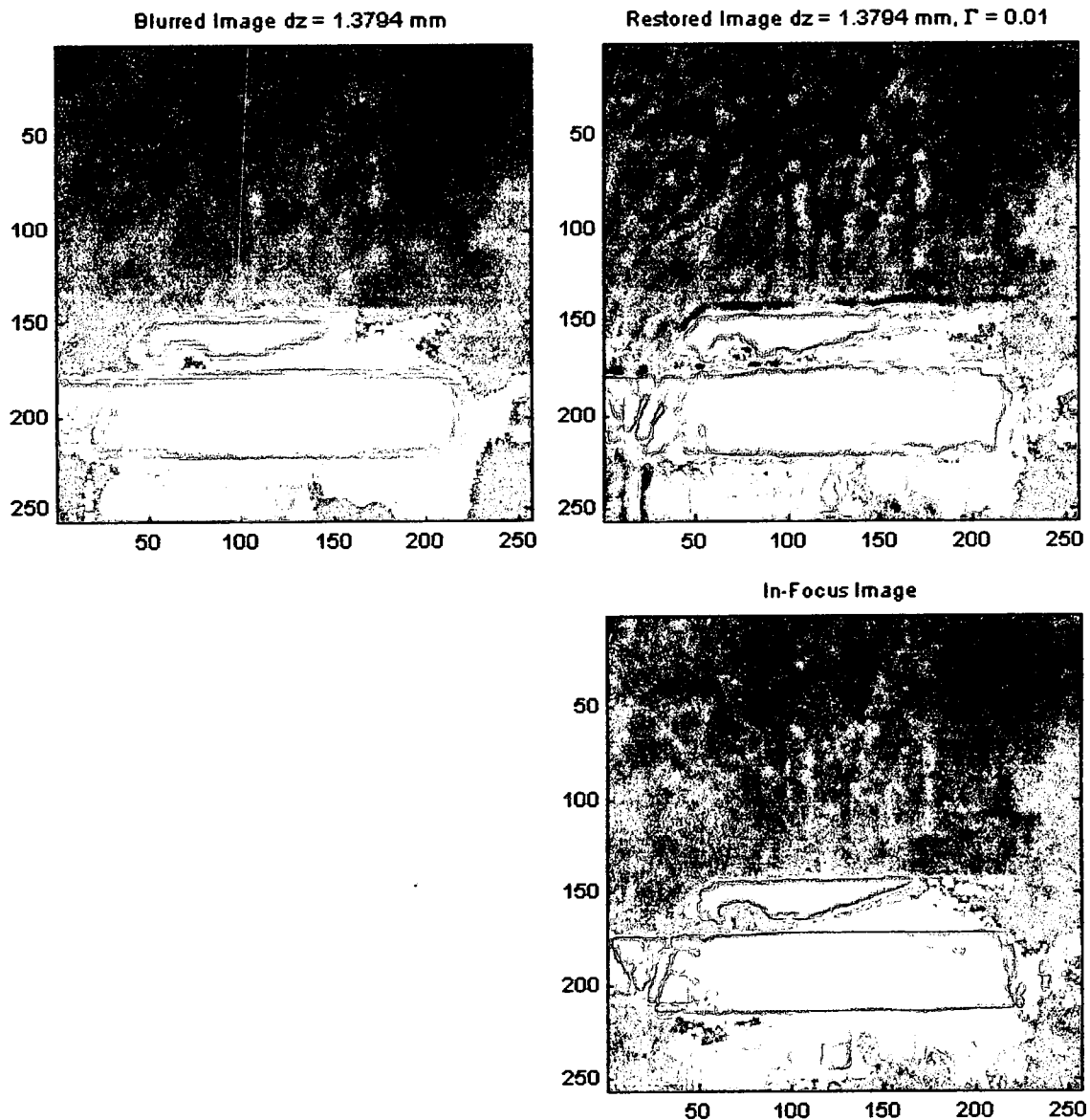


Figure 4-47: MWIR Imagery, $dz = 1379$ Microns

The defocus position for Figure 4-47 was $dz = 1379$ microns while the first zero in the MTF occurs at $dz = 1162$ microns. The MTF associated with this position would be similar to the modeled MTF in Figure 4-39. This MTF has a zero and therefore it is expected the restored image will exhibit distorting ringing effects.

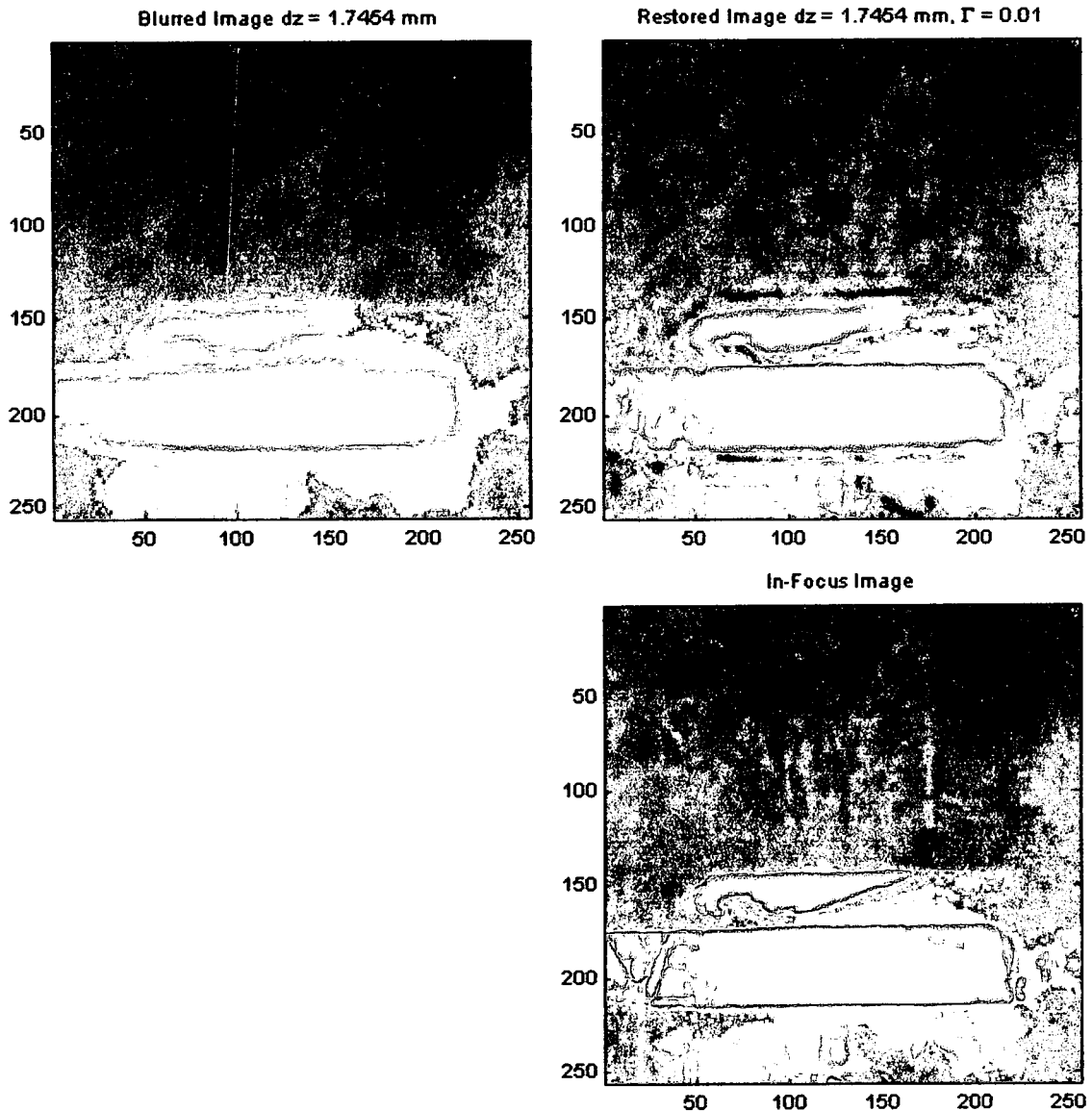


Figure 4-48: MWIR Imagery, $dz = 1745$ Microns

The defocus position for Figure 4-48 was $dz = 1745$ microns while the first zero in the MTF occurs at $dz = 1162$ microns. The MTF associated with this position would be similar to the modeled MTF in Figure 4-40. This MTF has multiple zeros and the restored image should exhibit worse distortions than those in Figure 4-47.

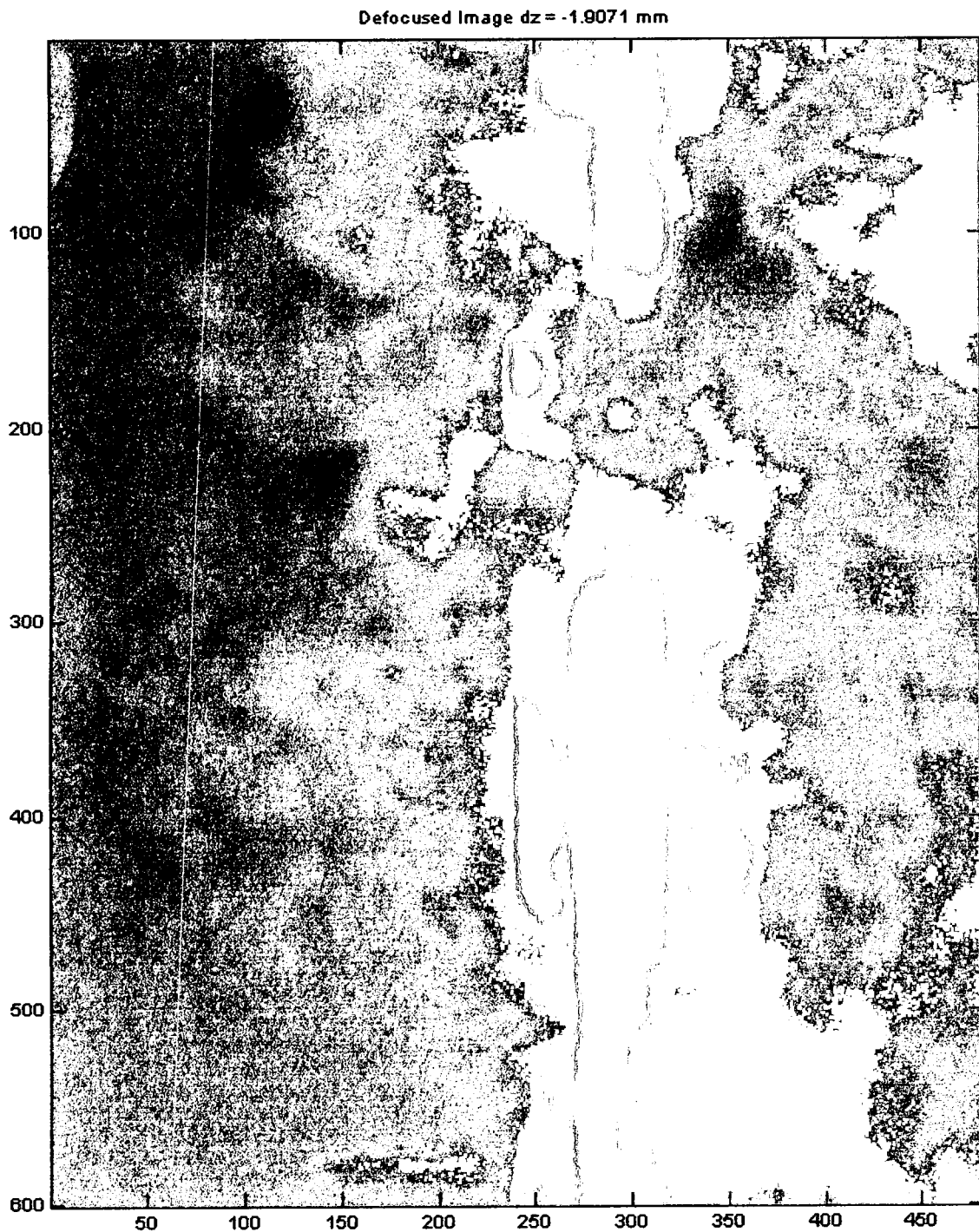


Figure 4-49: Sample Full-Size Defocused MWIR Imagery, $dz = -1907$ Microns (Zero in MTF)

Restored Image $dz = -1.9071 \text{ mm}$, $\Gamma = 0.01$



Figure 4-50: Sample Full-Size Restored MWIR Imagery, $dz = -1907 \text{ Microns}$ (Zero in MTF)

Defocused Image $dz = -0.3746$ mm

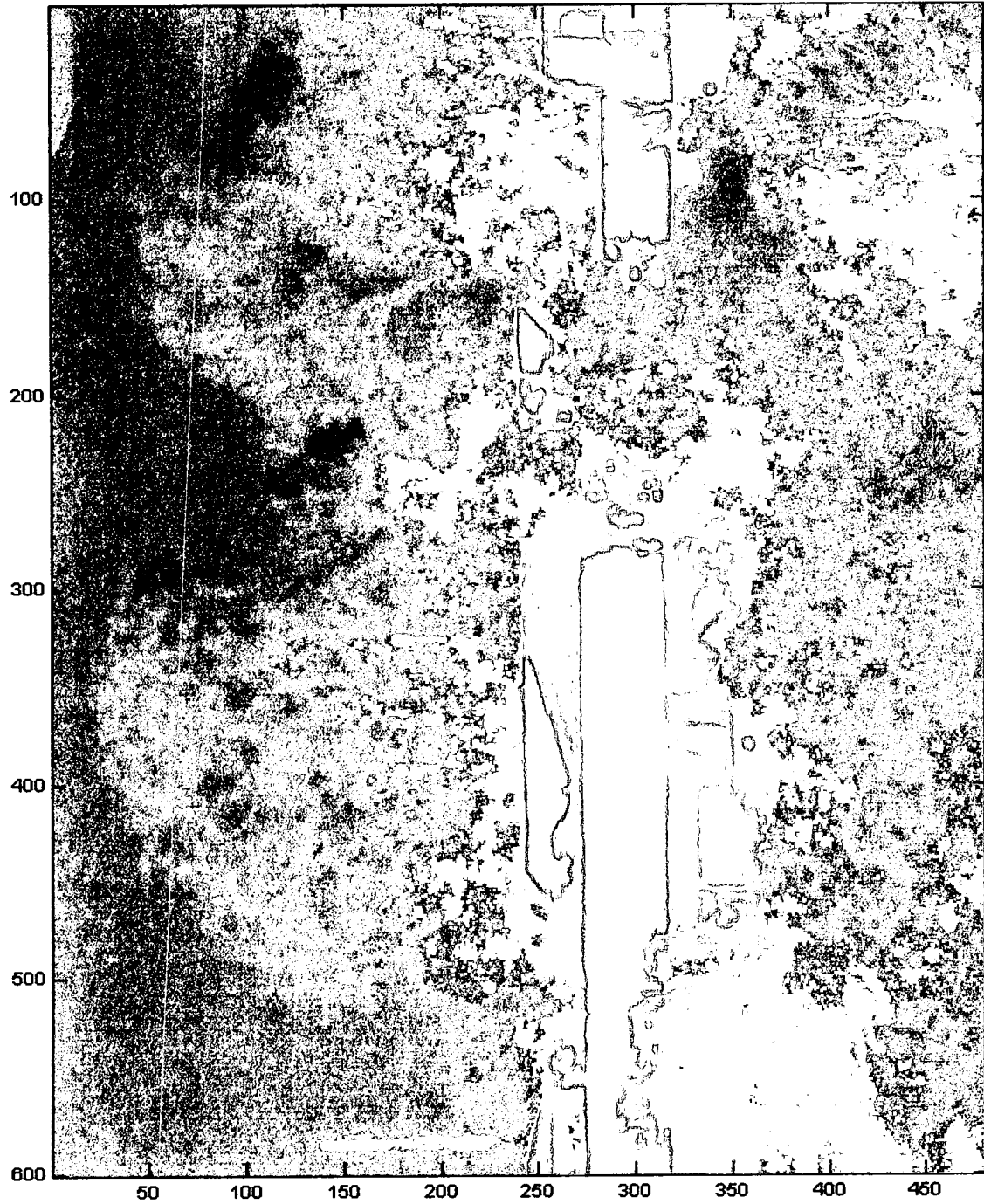


Figure 4-51: Sample Full-Size Defocused MWIR Imagery, $dz = -375$ Microns (No Zero in MTF)

Restored Image $dz = -0.3746$ mm, $\Gamma = 0.01$

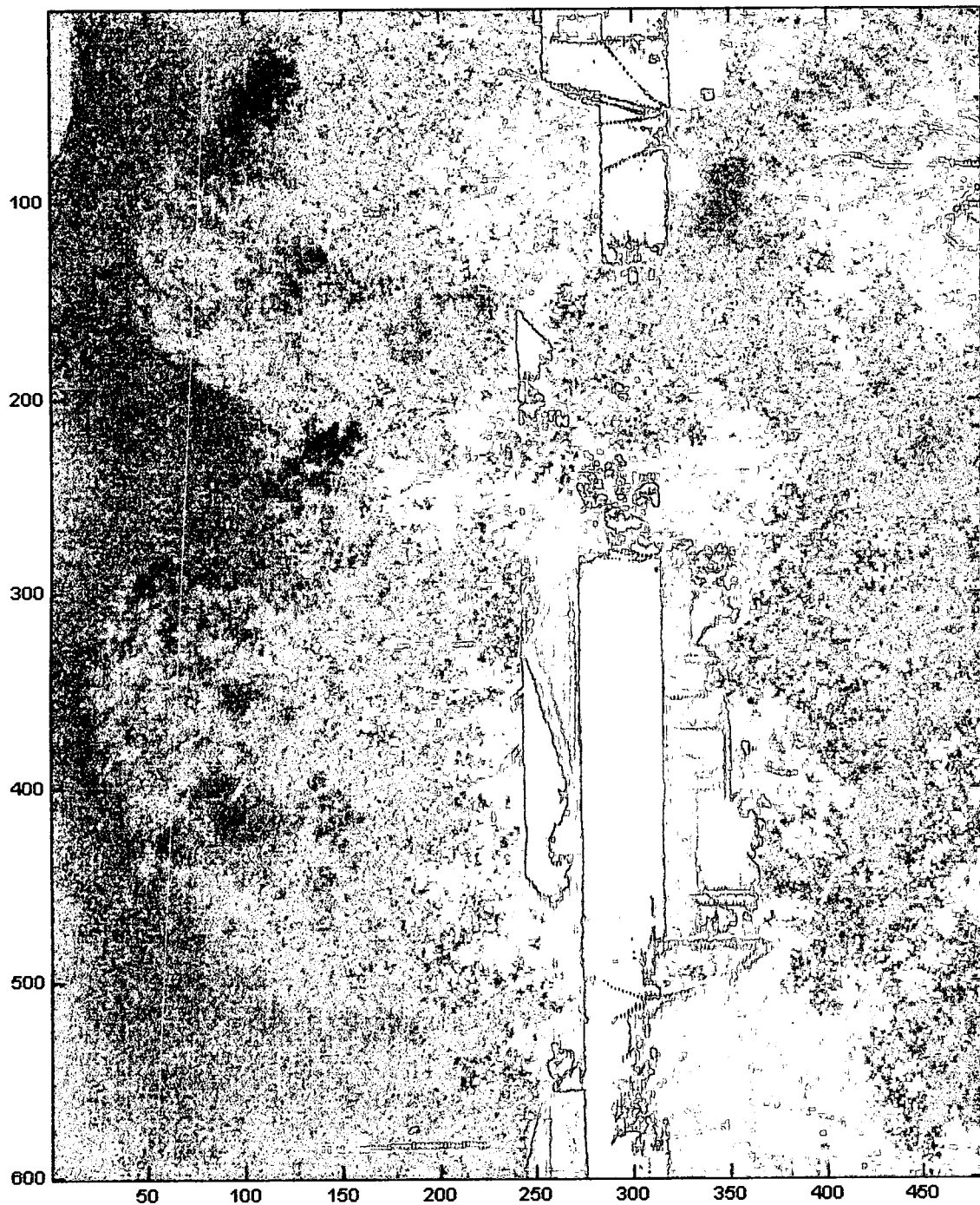


Figure 4-52: Sample Full-Size Restored MWIR Imagery, $dz = -375$ Microns (No Zero in MTF)

CHAPTER 5

Conclusions

The work of this thesis was divided into two parts: the development of a defocused imaging model and the application of that model to two imaging systems. The end result was restoring real defocused imagery from two different imaging systems - the results of which were satisfactory enough to both validate the model constructed and to provide impetus for further research.

The initial work determined an appropriate model for the monochromatic defocus PSF of an imaging system and was through using a defocus experiment using a HeNe laser for illumination. An algorithm for computing this PSF was constructed to facilitate the characterization of the two imaging systems because thousands of computations using numerical integration were prohibitive due to time considerations. It was discovered that the monochromatic defocus PSF was not accurate enough to satisfactorily restore actual defocused imagery, but an approximate polychromatic defocus PSF that incorporates the effects of longitudinal chromatic aberration was sufficiently accurate to provide decent results. This conclusion is based upon the fact that restoring images is highly dependant upon the accuracy of the PSF assumed and that the modeled PSFs in Figures 4-5 and 4-34 severely disagree with the monochromatic defocus PSFs predicted by Equation 2-3.

A combination achromatic doublet and board CCD imaging system was constructed for the initial investigation. Both monochromatic defocus experiments and

defocused imaging experiments were conducted using this setup to validate the defocus models constructed. The results of restoring defocused imagery from this basic imaging system were satisfactory enough that it was decided to experiment with a higher quality, pre-fabricated MWIR camera. Defocused imagery was taken by translation of the focus lens group seen in Figure 4-30. It was necessary to build a model of the optics using the optical design software Zemax in order to determine the defocus distances from the image plane to the sensor associated with each position of the lens group.

The process by which defocused imagery collected from either system was restored began with characterizing each system. To this end, modeled defocus PSFs were computed for incremental distances in relation to the focal shift curve. The image quality metric defined in Chapter 3 was computed at each position and the global minimum of this metric was defined to be the location of the image plane. This characterization provided the offset distance that allowed for the experimental defocus distances from the image plane recorded using a micrometer to be translated into defocus distances in relation to the focal shift curve of the optics. The defocused imagery from both systems was then restored using the modeled PSFs with a standard Wiener deconvolution filter. The results for the visible system appear slightly better than the results for the MWIR system. One possible reason is the higher noise level in the MWIR system. The Noise-to-Signal ratio (Γ) used for the visible system was .001 and for the MWIR system it was .01. If the noise had been less and a smaller Γ could have been used, spatial frequency content in the defocused images would have been boosted more by the Wiener deconvolution filter. The other possible reason is that more about the MWIR system was unknown and was therefore assumed. This included the Responsivity of the sensor and

the Transmittance of the optics. If these were incorrectly estimated it could be a large source of error.

There are several ways in which the results presented here could be improved upon. First, using a more accurate PSF for restoration would improve the quality of the restored images. The modeled PSF used assumes only diffraction and longitudinal chromatic aberration for aberrations of the optics. The inclusion of other aberrations in the model could increase its accuracy. One could also potentially account for these other aberrations by experimentally measuring the PSF in the defocus plane where it is desired to place the sensor. Another way to improve results is to use better optics – specifically optics designed to further flatten the focal shift curve. There are several types of optics with flattened curves: Achromats, Apochromats, and Superachromats representing two, three, and four wavelengths respectively sharing identical focal lengths [14]. The only issue in using optics with these higher order corrections is the increased cost. Finally, using a sensor for which the spectrum can be determined at each pixel would allow for the computation of the defocus image PSF (Equation 3-3) as it varied over the object instead of simply assuming a single spectrum and a single PSF for the entire image. One possibility is to use infrared sensors for which temperatures at each pixel can be obtained. Using the black body spectrum associated with a given temperature, a spectrum for each pixel could be obtained and a PSF at each pixel determined. However, the method of restoration using a Wiener filter presented in this thesis would not work if there were different PSFs at each pixel and therefore an alternate method (unknown to this author) would have to be employed.

The main limitation on the distance a sensor could be defocused and decent restorations still obtained is the occurrence of zeros in the MTF once defocus is severe enough. One possible direction for further research is to incorporate multiple sensors all of which are defocused different distances. The reason for this is that the zeros in the MTF occur at different spatial frequencies for different amounts of defocus. It may therefore be possible to combine several defocused images of the same scene and have the spatial frequency information lost from one zero in one image compensated for by another image without a zero at that spatial frequency. Fortunately, methods for the combination of multiple blurred images of the same scene to obtain one restored image already exist (For example, [17]).

The conclusion drawn from this work is that for intensity imaging with incoherent illumination of an opaque object it is possible to restore defocused images and obtain a reasonable facsimile of the in-focus image given that the sensor location remains within the bounds set by locating the positions of occurrence of new zeros in the MTF. Further constraints on the imaging systems for which this approach will work best are as follows: (1) the system should have a low Noise-to-Signal ratio, (2) the system should either have a narrow imaging band or be highly corrected for longitudinal chromatic aberration, (3) the imaging system should be shift-invariant (the PSF should not vary over the image) or else Wiener deconvolution won't work, and (4) if the system exhibits significant aberration beyond LCA and diffraction, then the modeled PSFs presented here won't work in their present form (Either the model would have to be updated to include higher aberrations or PSFs would have to be experimentally determined). Despite these

limitations, the results obtained were sufficiently positive that it is expected the extension of this work to the applications mentioned in Chapter 1 would be worthwhile.

Appendix A

Fresnel Defocus Diffraction Integral

```
function [out,r,M] =  
defocusmonopsfapprox(lam,w,fnum,diam,N,tolerance,epsilon);  
% function [out,r,M] =  
defocusmonopsfapprox(lam,w,fnum,diam,N,tolerance,epsilon);  
%  
% Mark Burky 2007  
%  
% Computes the Fresnel Defocus Diffraction Integral defined  
in Chapter 2 of  
% Mark Burky's Master's Thesis (Equation 2-3) using the  
algorithm developed  
% in Section 2.2.  
%  
% Specifically, this computes the intensity distribution in  
a plane defocused  
% from the focal plane given that a circular lens is  
illuminated by either  
% an on-axis spherical or plane monochromatic wave.  
%  
% Inputs:  
%  
% lam is the wavelength of the light  
%  
% w/lam is the max waves of defocus error. Given a defocus  
distance dz, w  
% is equal to  $(1/(8*(di/diam)^2)/(1/dz + 1/di))$  and this  
function assumes  
% it is provided in microns. di is the distance from the  
exit pupil to the  
% focal plane for lam.  
%  
% fnum is  $di^2/diam$  where di is the distance from the exit  
pupil to the  
% defocused plane.  
%  
% diam is the diameter of the exit pupil of the optics in  
mm.  
%
```



```

% N is the number of radial points to compute
%
% tolerance is the maximum fractional error at any output
point except possibly those
% from  $(1-\text{epsilon}) \cdot a < r < (1+\text{epsilon}) \cdot a$ 
%
% Typical input values ~ tolerance = .01, epsilon = .05
%
% Outputs:
%
% out is the 1-D intensity distribution as a function of
radial output, r. M
% is the # of iterations required to obtain the desired
tolerance. The
% output radial values in r are in Microns.

lam = double(lam)*10(-6);
fnum = double(fnum);
w = double(w)*10(-6);
diam = double(diam)*10(-3);

% Constants defined for convenience
a = 4*w*fnum;
b = pi/(lam*fnum);
binv = 1/b;
c = b*a;

R = double(diam)/2;% Radius of Exit Pupil
zpos = double(fnum*diam);% Distance from exit pupil to
defocus plane.

% First Zero of Airy Disk
r0 = 1.220*pi/b;

% Upper value for r. a approaches the geometric radius.
For small amounts
% of defocus a approaches zero and isn't a suitable upper
value for r. We
% use 10 times the first zero of the airy disk as a minimum
cutoff value.

rupper = max(5*r0,2*abs(a));

r = double(linspace(0,rupper,N));% radial points to
evaluate the integral at.

% We need to make certain  $r = a$  is contained in r
if sum(r==abs(a))~=1

```

```

    ind = min(find(r>abs(a))); % Keep number of points
    constant. Replace nearest point to a with a.
    r = [r(r<abs(a)) abs(a) r([ind+1:end])];

end

if w==0
    r(1)=eps^4; % Avoid divide by zero.
end

M = 1;
%Index of a in r
ind = min(find(r>abs(a)))-1;

x = b*r;

if w~=0

    t = i*a./[1 r([2:end])]; % Avoid divide by zero.
    % The first element in t is irrelevant because only
    values for r>a are
    % used.
    mti = i*r/a; % Minus of the inverse of t.
    st0 = exp(.5*(i*c + x.*mti)) - besselj(0,x); % Initial
    value of the "short" Bessel series
    st0 = st0([1:ind-1]); % Only need to evaluate this for
    values of r<a
    exact = (exp(i*c) - besselj(0,abs(c)))/2; % Exact value
    of the field at r = a
    suml = 0; % Initial long term
    sums = st0; % Initial short term

end

if w==0
    max_error=0; % If w==0 an analytic solution is available
else
    max_error=1; % Fractional error assumed to be 100% at
    start
end

while ((max_error>tolerance)) % Continue until
max_error<tolerance

    BessJ = besselj(M,x);

    suml = suml + t([ind:end]).^(M).*BessJ([ind:end]); % Add

```

```

another term onto the long Bessel series
    sums = sums - mti([1:ind-1]).^(M).*BessJ([1:ind-1]);%
Add another term onto the short Bessel series

    % Compute the upper bound on the fractional error for
the short series
    Es_frac = (0.6748/(M+1)^(1/3)*(r(r<(1-
epsilon)*abs(a))/abs(a)).^(M+1).*1./(1-r(r<(1-
epsilon)*abs(a))/abs(a)))./abs(sums([1:length(r(r<(1-
epsilon)*abs(a))))));

    % In computing El_frac below, it is possible suml
contains points
    % between r=a and r=(1+epsilon)*a and these must be
excluded.
    N_diff = length(suml)-length(r(r>(1+epsilon)*abs(a)));

    % Compute the upper bound on the fractional error for
the long series
    El_frac =
0.6748/(M+1)^(1/3)*(abs(a)./r(r>(1+epsilon)*abs(a))).^(M+1)
.*1./(1-
abs(a)./r(r>(1+epsilon)*abs(a)))./abs(suml([N_diff+1:end]))
;

    % Exact fractional error at r=a
    Ea_frac = abs(suml(1)-exact)./abs(suml(1));

    % Max_error is the maximum of the three errors
    max_error = max([Es_frac El_frac Ea_frac]);

    M = M + 1;% Increment M

end

if w == 0 % If w == 0 then output Airy disk
    defpsf = abs(besselj(1,x)./r).^2;
    norm = R^2;% Normalization
else
    defpsf = abs([sums suml]).^2; % If w ~= 0 then output
the concatenation of the short and long Bessel series.
    norm = R^4/(2*zpos*w)^2;% Normalization
end

out = norm*defpsf;
r = r*10^6;% Microns
r(1) = 0;% Reset first value to zero.

```

Appendix B

Polychromatic Defocus Imaging PSF

```
function [out,xhr,yhr,maxint,lROUT,xi,yi,LAM,NyqPer] =  
defocuspolyps(psfd,diam,lamb,dlamb,flamb,nlamb,focalshift,  
freqresp,spectrum,di,dz,rl,maxdz,N,tolerance);  
% function [out,xhr,yhr,maxint,lROUT,xi,yi,LAM, NyqPer] =  
defocuspolyps(psfd,diam,lamb,dlamb,flamb,nlamb,focalshift,  
freqresp,spectrum,di,dz,rl,maxdz,N,tolerance);  
%  
% Mark Burky 2007  
%  
% Computes the approximate incoherent intensity  
polychromatic defocus PSF  
% defined in Mark Burky's Master's Thesis (Equation 3-3) in  
Section 3.2.  
% Each wavelength is Fresnel propagated independantly to  
the plane of the  
% sensor a distance dictated by longitudinal chromatic  
aberration  
% (focal shift curve). The monochromatic PSFs are added in  
intensity  
% although weighted by the spectrum*frequency response,  
convolved with  
% the pixel PSF, then downsampled to the pixel frequency of  
the sensor.  
%  
% Inputs:  
%  
% psfd 1x2 array containing the pixel densities of the  
sensor  
% ([vertical horizontal ])in pixels/micron  
%  
% diam is the diameter of the (circular) exit pupil in mm.  
%  
% lamb is the center wavelength of the band of wavelengths  
imaged (Microns)  
%  
% dlamb is the width of the imaging band (Microns)  
%  
% flamb is one wavelength that is in focus at di. (Microns)  
This locates
```

```

% the focal shift curve in reference to the image plane.
%
% nlamb is the # of wavelengths to evaluate
%
% focalshift is a 2xX array (X is not specified) containing
the focalshift
% curve that defines the deviation in focus for each
wavelength relative to
% the focus for a reference wavelength. The first row is
an array of
% wavelengths (Microns) and the second an array of
distances (Microns).
%
% freqresp is a 2xY array (X is not specified) containing
the spectral
% sensitivity of the sensor. The first row is an array of
wavelengths
% (Microns) and the second an array of the normalized
response of the
% sensor for each wavelength.
%
% spectrum is a 2xY array (X is not specified) containing
the spectrum
% of the reflected light from the imaged object. The first
row is an
% array of wavelengths (Microns) and the second an array of
spectral
% component values
%
% di is the distance to the image plane (mm)
%
% dz is the distance from the image plane to the plane in
which the sensor
% is located (the defocus plane)
%
% rl is the number of radial points to compute the
polychromatic PSF at.
%
% maxdz is the maximum defocus distance for any of the
wavelengths.
% Ballpark guess is probably good enough. (mm)
%
% N is the # of radial points computed for each
monochromatic PSFs
%
% tolerance is a parameter passed to the monochromatic
defocus PSF function
% that sets the maximum fractional error in the mono PSFs.

```

```

%
%
% Outputs: [out,xhr,yhr,maxint,lROUT,xi,yi,LAM,NyqPer]
%
% out is the 2-D High-Resolution PSF
%
% xhr is the horizontal axis for the High-Resolution PSF.
%
% yhr is the vertical axis for the High-Resolution PSF.
%
% maxint is an array containing the maximum intensity of
each
% individual monochromatic PSF
%
% lROUT is the 2-D Lo-Res PSF sampled at the pixel
frequencies of the
% sensor
%
% xi is the horizontal axis for the Lo-Res PSF.
%
% yi is the vertical axis for the Lo-Res PSF.
%
% LAM is an array of the wavelengths for which
monochromatic PSFs
% were computed to produce the polychromatic PSF
%
% NyqPer is the ratio of the Lo-Res PSF sampling frequency
to the
% High-Res PSF sampling frequency. Useful for comparisons.

```

```

psfd = double(psfd);
diam = double(diam);
di = double(di);
dz = double(dz);
lamb = double(lamb);
dlamb = double(dlamb);
flamb = double(flamb);
focalshift=double(focalshift);
freqresp=double(freqresp);
spectrum = double(spectrum);

```

```

% Determine an appropriate band of wavelengths
minlamb1 = min(focalshift(1,:));
minlamb2 = min(freqresp(1,:));
minlamb3 = min(spectrum(1,:));
minlamb = max([minlamb1 minlamb2 minlamb3]);
maxlamb1 = max(focalshift(1,:));

```

```

maxlamb2 = max(freqresp(1,:));
maxlamb3 = max(spectrum(1,:));
maxlamb = min([maxlamb1 maxlamb2 maxlamb3]);

if nlamb == 1
    lm = lamb;
else
    lolamb = max([(lamb-dlamb/2) minlamb]);
    hilamb = min([(lamb+dlamb/2) maxlamb]);
    lm = linspace(lolamb,hilamb,nlamb);
end

LAM = lm;

% Evaluate the focalshift curve at wavelengths of interest.
fcst = interp1(focalshift(1,:),focalshift(2,:),lm,'cubic');

% Shift the focal shift curve so "zero" is at the focal
plane for flamb
shiftbase =
interp1(focalshift(1,:),focalshift(2,:),flamb,'cubic');

% Distance to focal plane for each wavelength
dim = di + (fcst - shiftbase)/1000;

% Distance to defocus plane from exit pupil
dic = di+dz;

% Defocus distance for each wavelength
dlz = dz - (dim - di);

% Relative frequency response for wavelengths of interest
fr = interp1(freqresp(1,:),freqresp(2,:),lm,'cubic');
fr = fr/max(fr(:));

% Spectrum for wavelengths of interest
sp = interp1(spectrum(1,:),spectrum(2,:),lm,'cubic');
sp = sp/max(sp(:));

% Define an appropriate upper radius to evaluate the PSF
at.
geomrad = abs(diam*maxdz/di*1000)/2;% Geometric defocus
Radius
r0 = 1.220*di/diam*max(lm); %First zero in Airy disk for
largest wavelength computed.
rup = max([geomrad*2 5*max(psf.^(-1)) r0*2]); %Make sure
we have an appropriate upper bound on radius.

```

```

% Make the higher resolution sampling frequency a factor of
the pixel
% frequency. This should make for a better downsampling
later.

factor = floor((rup/rl)^(-1)/psfd(2));
rup = (factor/rl)^(-1)/psfd(2);

% Array of Radius Values
r = double(linspace(0, rup, rl));

% Initialize PSF array with zeros
hrout = double(zeros([1 length(r)]));

% For loop to compute a mono PSF for each wavelength
for q = 1:length(lm)

    fnum1 = dic/diam;% fnum1 is the fnum using the distance
    from the exit pupil
    % to the defocus plane in which the sensor is located
    fnum2 = dim(q)/diam;% fnum2 is the fnum associated with
    each wavelength's focal plane

    if dlz(q)~=0
        %wdf/lam is the # of waves of defocus error for that
        wavelength (Microns)
        wdf = (1/(8*fnum2^2))/(1/dlz(q)+1/dim(q))*1000;
    else
        wdf=0;% Avoid dividing by zero in the equation for wdf.
    end

    % Use the monochromatic defocus PSF function for each
    wavelength
    [hrtempl,rd,M] =
    defocusmonopsfapprox(lm(q),wdf,fnum1,diam,N,tolerance,.05);

    % Because the defocusmonopsfapprox does auto-selecting of
    radius values to
    % evaluate, we interpolate onto the radius grid defined
    above.
    hrtemp = interp1(double(rd),double(hrtempl),r,'cubic',0);

    maxint(q) = max(hrtempl(:)); % Max Intensity for that PSF
    hrtemp = hrtemp*fr(q)*sp(q);% Weighting
    hrout = hrout + hrtemp;% Sum the weighted mono PSFs

end

```



```
[out,x,y] = gencircsym(hrout);% Rotate the computed PSF to  
obtain a 2-D PSF.
```

```
out = out/sum(out(:));% Normalize
```

```
xhr = [sort(-r([2:end]),'ascend') r];% Zero center the  
horizontal grid  
yhr = xhr;
```

```
psfw = 2*r(end)-1;% Physical width of the outputed PSF  
window
```

```
outwidth1 = ceil(psfd(1)*psfw);% Vertical width for the  
downsampled PSF in pixels  
outwidth2 = ceil(psfd(2)*psfw);% Horizontal width for the  
downsampled PSF in pixels
```

```
% For convenience, make the widths odd #s  
if mod(outwidth1,2)==0  
    outwidth1 = outwidth1 - 1;  
end
```

```
if mod(outwidth2,2)==0  
    outwidth2 = outwidth2 - 1;  
end
```

```
% High resolution sampling frequency. If this is too low,  
increase rl.  
fs = (r(2)-r(1))(-1);
```

```
% Ratio of Nyquist frequencies.  
NyqPer = psfd(2)/fs;
```

```
% Pixel PSF size  
blurx = round(fs/psfd(2));  
blury = round(fs/psfd(1));
```

```
% Convolve the poly PSF with the Pixel PSF  
if blurx*blury~=0
```

```
blur = double(ones(blury,blurx)/(blurx*blury));
```

```
OTF = fft2(out);  
CCDTF = fft2(blur,2*rl-1,2*rl-1);  
out1 = ifft2(OTF.*CCDTF);
```

```
else
```

```

    disp('You need to increase rl, the # of radial
points.')
    out1 = out;
end

out = out1;

% Downsample with imresize. It would be better to actually
downsample here, but
% there is no guarantee that the vertical and horizontal
pixel frequencies
% can both divide fs.
lrout = imresize(out1,[outwidth1 outwidth2],'bicubic');

lrout = lrout/sum(lrout(:));% Normalize

xi = linspace(-psfw/2,psfw/2,outwidth2);% x grid
yi = linspace(-psfw/2,psfw/2,outwidth1);% y grid

```

Appendix C

Wiener Deconvolution Filter

```
function [out,HW] = wiener2d(in,psf,nsr,border,padtype)
%
%   [out,HW] = wiener2d(in,psf,nsr,border)
%
%       Does 2D IIR Wiener Filtering
%
%       out      -   filtered signal
%       HW       -   Wiener filter DFT samples
%       in       -   input signal
%       psf      -   FIR impulse response of degradation
process
%       nsr      -   Noise to signal ratio (~ .01 - .1)
%       border   -   border padding size to minimize ringing
artifacts (~20)
%
% Author: Dr. Russell Hardie
% Modified 1/27/99

% Pad image and get new size
[psfy,psfx]=size(psf);

% Make certain we pad enough so that we are performing the
equivalent of
% convolution and not circular convolution.  (Actually,
this over pads.)

if border<max([psfy psfx])
    border=max([psfy psfx]);
end

% Pad Image
in=padarray(in,[border,border],padtype);% Padtype can be
'circular',
% 'replicate', or 'symmetric'
in=double(in);
psf=double(psf);

[L1,L2]=size(in);
```

```

% Create Wiener filter
H = fft2(psf,L1,L2);
absH2 = abs(H.^2);
HW = conj(H)./(absH2+nsr);

% Filter and Compute inverse DFT
X = fft2(in);
out = real(ifft2(HW.*X));

% circularly shift output to compensate for the
% PSF being defined in the 1st quadrant (circ shifted
% with respect to 0,0.
out=circshift(out,[round((psfy-1)/2),round((psfx-1)/2)]);

% cut out original image size
out=out(1+border:L1-(border),1+border:L2-(border),:);

```

REFERENCES

- [1] Castleman, K., *Digital Image Processing*, (Prentice Hall, 1996)
- [2] M. Gu, *Advanced Optical Imaging Theory*, (Springer, 2000, Pg. 46)
- [3] Stockseth, P, *Properties of a Defocused Optical System*, Journal of the Optical Society of America. 1969, Vol. 59, #10, 1314-1321.
- [4] Van Der Gracht, J., Euliss, G., and Pauca, V., *Experimental investigation of aliasing in the assessment of sampled images*, Proceedings of SPIE, the International Society of Optical 2002.
- [5] Wach, H., Dowski, E., and Cathey, W., *Control of Chromatic Focal Shift Through Wave-Front Coding*, Applied Optics, VOL. 37, 5359-5367, 1998
- [6] J. Goodman, *Introduction to Fourier Optics 3rd Edition*, (Roberts and Company Publishers, Colorado, 2005).
- [7] Mielenz, K., *Algorithms for Fresnel Diffraction at Rectangular and Circular Apertures*, Journal of Research of the National Institute of Standards and Technology, Vol. 103, #5, Pgs. 504-507.
- [8] G.O. Olaofo, *Diffraction by Gaussian Apertures*, Journal of the Optical Society of America. Vol. 60, Num. 12 (1970).
- [9] G. Watson, *A Treatise on the Theory of Bessel Functions*, (Cambridge Univ. Press, 1995).
- [10] L. Landau, *Bessel Functions: Monotonicity and Bounds*, Journal of the London Mathematical Society. 2000, 61, 197-215.
- [11] Gander, W. and Gautschi, W., *Adaptive Quadrature - Revisited*, BIT, Vol. 40, 2000, pp. 84-101.
- [12] Mitra, S., *Digital Signal Processing 3rd Edition*, (Mcgraw Hill, 2006)
- [13] Gonzalez, R. and Woods, R., *Digital Image Processing, 2nd Edition*, (Prentice Hall, 2001, pg. 201)

- [14] Smith, W., *Modern Optical Engineering 3rd Edition*, (Mcgraw Hill, 2000)
- [15] Saleh, B. and Teich, M., *Fundamentals of Photonics*, (John Wiley & Sons, Inc., 1991)
- [16] Jain, A., *Fundamentals of Digital Image Processing*, (Prentice Hall, 1989, pg. 279)
- [17] Harikumar, G. and Bresler, Y., *Exact Image Deconvolution from Multiple FIR Blurs*, IEEE Transactions on Image Processing, VOL. 8, NO. 6, June 1999

ROO2S94034